Modeling and Control of Undesirable Dynamics in Atomic Force Microscopes

by

Osamah M. El Rifai

B.S., King Saud University (1993)
M.S., The University of Michigan, Ann Arbor (1996)

Submitted to the Department of Mechanical Engineering
in partial fulfillment of the requirements for the degree of

Doctor of Philosophy in Mechanical Engineering

at the

MASSACHUSETTS INSTITUTE OF TECHNOLOGY

February 2002

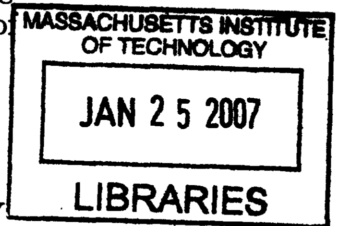

© Massachusetts Institute of Technology 2002. All rights reserved.

Author ....
Department of Mechanical Engineering
January 10, 2002

Certified by ....
Kamal Youcef-Toumi
Professor of Mechanical Engineering
Thesis Supervisor

Accepted by ....
Ain Sonin
Chairman, Department Committee on Graduate Students

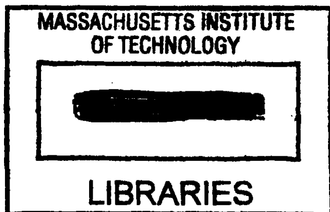

ARCHIVES

Modeling and Control of Undesirable Dynamics in Atomic Force Microscopes

by

Osamah M. El Rifai

Submitted to the Department of Mechanical Engineering
on January 10, 2002, in partial fulfillment of the
requirements for the degree of
Doctor of Philosophy in Mechanical Engineering

Abstract

The phenomenal resolution and versatility of the atomic force microscope (AFM), has made it a widely-used instrument in nanotechnology. In this thesis, a detailed model of AFM dynamics has been developed. It includes a new model for the piezoelectric scanner coupled longitudinal and lateral dynamics, creep, and hysteresis. Models for probe-sample interactions and cantilever dynamics were also included. The models were used to improve the dynamic response and hence image quality of contact-mode AFM. An extensive parametric study has been performed to experimentally analyze in-contact dynamics. Nonlinear variations in the frequency response were observed, in addition to changes in the pole-zero structure. The choice of scan parameters was found to have a major impact on image quality and feedback performance. Further, compensation for scanner creep was experimentally tested yielding a reduction in creep by a factor of 3 to 4 from the uncompensated system.

Moreover, fundamental performance limitations in the AFM feedback system were identified. These limitations resulted in a severe bound on the maximum achievable feedback bandwidth, as well as a fundamental trade-off between step response overshoot and response time. A careful analysis has revealed that a PID controller has no real advantage over an integral controller. Therefore, a procedure for automatically selecting key scan parameters and controller gain was developed and experimentally tested for I-control. This approach, in contrast to the commonly used trial and error method, can substantially improve image quality and fidelity. In addition, a robust adaptive output controller (RAOC), was designed to guarantee global boundedness and asymptotic regulation in the presence and absence of disturbances, respectively. Simulations have shown that a substantial reduction in contact force can be achieved with the RAOC, in comparison with a well-tuned I-controller, yet with no increase in the maximum scan speed. Furthermore, a new method was developed to allow calibrating the scanner's vertical displacement up to its full range, in addition to characterizing scanner hysteresis. This work has identified and addressed crucial problems and proposed practical solutions to factors limiting the dynamic performance of the AFM.

Thesis Supervisor: Kamal Youcef-Toumi
Title: Professor of Mechanical Engineering

Acknowledgments

I would like to thank my advisor, Professor Kamal Youcef-Toumi for his support, insightful advise, and continuous encouragement. I am also very thankful to my committee members, Professor George Verghese and Professor Samir Nayfeh, for their valuable insight and comments throughout the development of the thesis.

My great gratitude and appreciation goes to my parents. Their unconditional love and support have made all this possible. I would also like to extend my thanks to my brother Khalid and the rest of my family. Finally, I would like to thank all of my friends whom their friendship has made this journey pleasantly memorable.

Contents

1 Introduction **13**

1.1 Background 13

1.2 Technical Challenges and Research Objectives 15

1.3 Literature Survey 18

1.3.1 Modeling 18

1.3.2 Control 20

1.4 Thesis Overview 21

2 Modeling **23**

2.1 Atomic Force Microscope 23

2.2 Probe-sample Interactions 26

2.2.1 In-contact Interactions: Vertical Forces 26

2.2.2 In-contact Interactions: Lateral Forces 29

2.2.3 Out-of-contact Interactions: Vertical Forces 30

2.2.4 Point of Contact 30

2.3 Scanner Model 30

2.3.1 Piezoelectric Tube Lateral Dynamics 32

2.3.2 Extension Tube Lateral Dynamics 37

2.3.3 Piezoelectric Tube Longitudinal Dynamics 39

2.3.4 Extension Tube Longitudinal Dynamics 42

2.3.5 Hysteresis and Nonlinear Displacement Sensitivity 44

2.3.6 Creep 50

2.4 Cantilever Dynamics 54
2.4.1 Flexural Dynamics 54
2.4.2 Cantilever Twist 56
2.5 Noise and Disturbances 57
2.6 Overall AFM Model 57
2.7 Summary 58

3 Scanner Calibration **59**
3.1 Introduction 59
3.2 New Method for Scanner Height Calibration 60
3.3 Error Analysis 66
3.4 Summary 68

4 Model Validation **69**
4.1 Experimental Setup 69
4.2 Modifications to Experimental Setup 69
4.3 Cantilever Specifications 70
4.4 Force-separation Curve 70
4.5 Scanner Modes Identification 71
4.6 In-contact Dynamics 73
4.6.1 Frequency Responsc: Simulations 73
4.6.2 Frequency Responsc: Experiments 77
4.7 Scanning Simulation vs. Experiments 84
4.8 Scanner Hysteresis 84
4.9 Scanner Creep 86

5 Creep Compensation **93**
5.1 Introduction 93
5.2 Creep Compensation 94
5.2.1 530 nm Steps 94
5.2.2 1590 nm Steps 96

5.2.3 Notes on Parameter Identification for the Creep Model 98
5.2.4 Open Loop vs. Closed Loop 99
5.3 Summary 100

6 Automatic Selection of Scan and Controller Parameters 101

6.1 Introduction 101
6.2 On Factors Affecting Scan Parameter Selection 101
6.3 Trade-offs and Performance Limitations in AFM Feedback System 104
6.3.1 Scanner Bending Modes 107
6.3.2 Uncertainty 107
6.3.3 Poles and Zeros of a Transfer Function 110
6.4 Performance of PID and Higher Order LTI Controllers 115
6.5 Integral Controller 117
6.6 Feedforward Compensation 128
6.7 Variable Scan Speed Scanning 129
6.8 Robust Adaptive Output Control 133
6.9 Robust Adaptive Output Control Applied to AFM 142
6.9.1 Selection of Controller Parameters 143
6.9.2 Simulation Results 146
6.10 Summary 151

7 Conclusions and Recommendations 152

A Parameter Values Used in Simulations 166

List of Figures

1-1 AFM images: (a) $72\,\mu m/s, K_p = K_i = 2$, (b) $96\,\mu m/s, K_p = K_i = 20$. 16

1-2 AFM images: $180\,\mu m/s$, (a) nominal contact force, (b) smaller contact force. 17

1-3 AFM image of Silicon Steps: image artifacts due to scanner creep. 18

1-4 Schematic of an AFM model that has been commonly used in the literature. 20

2-1 Schematic of the main components of an AFM. 24

2-2 Sample-on-scanner design of AFM. 25

2-3 Cantilever-on scanner design of AFM, (a) two-scanner design, (b) single-scanner design. 25

2-4 Force law for Lennard-Jones potential and Dugdale approximation in arbitrary units. 27

2-5 Schematic of the contact showing stress distribution. 28

2-6 Cantilever-on-scanner design: single piezoelectric scanner with extension tube. 31

2-7 Cross-section of the piezoelectric tube. 31

2-8 Free body diagram of the piezoelectric tube for lateral dynamics. 32

2-9 Free body diagram of the extension tube for lateral dynamics. 37

2-10 Free body diagram of the piezoelectric tube for longitudinal dynamics. . . . 40

2-11 Free body diagram of the extension tube for longitudinal dynamics. 43

2-12 Experiments using a sinusoidal input voltage at 300 Hz with two different amplitudes, smaller amplitude in red. 45

2-13 Relay hysteresis of Preisach model. 45

2-14 Piezoelectric scanner response to a sinusoidal input voltage at $20\,Hz$ (a) electrical displacement (arbitrary units AU) vs. input voltage, (b) mechanical displacement vs. input voltage. 48
2-15 Piezoelectric scanner response to a sinusoidal input voltage at $20\,Hz$: electrical displacement (arbitrary units AU) vs. mechanical displacement. . . . 49
2-16 Schematic representation of piezoelectric scanner with hysteresis. 50
2-17 Two creep experiments: (a) initial fast response, (b) slow creep response. . 51
2-18 Experimental creep response plotted on logarithmic scale. 52
2-19 Experimental frequency response between input voltage and displacement of a PZT-5H actuator (a) Full frequency range, (b) zoom on 10 to $300\,Hz$ range. 53
2-20 Schematic representation of a model for both fast and creep dynamics. . . . 53
2-21 Coupling between cantilever twist and PSD signal due to cantilever bending. 56

3-1 Schematic representation of an accelerometer. 61
3-2 Schematic of the AFM scanner, cantilever, and optical sensor. 61
3-3 Schematic of the piezoelectric scanner with a piezoresistive cantilever. . . . 62
3-4 (a) Cross section of scanner with sample holder, (b) Geometric coupling between scanner bending and extension. 68

4-1 Simulation: Quasi-static normalized force-separation curve. 71
4-2 Experimental force-separation curve 72
4-3 (a) Experimental frequency response, (b) Cross-section of the piezoelectric tube. 73
4-4 Schematic of probe-sample contact. 75
4-5 Simulation: In-contact frequency response for different ratios of sample to cantilever stiffness $\frac{k_s}{k_c}$. 76
4-6 Pole-zero map as a function of $\frac{k_s}{k_c}$: (left) zoom on the $3.4\,kHz$ mode, (right) zoom on the $380\,Hz$ mode. 76
4-7 System identification block diagram. 77
4-8 Force displacement curve for cantilever-A with a Glass sample. 78

4-9 In-contact frequency response of cantilever-A with a Glass sample: same amplitude for different set-points. 79
4-10 In-contact frequency response of cantilever-A with a Glass sample: $14\,nN$, different amplitudes. 79
4-11 In-contact frequency response of cantilever-A with a Glass sample: $17.6\,nN$, different amplitudes. 80
4-12 Force-displacement curve for cantilever-A with a PDMS sample. 81
4-13 In-contact frequency response of cantilever-A with a PDMS sample: $17\,nm$ amplitude for different set-points. 81
4-14 In-contact frequency response of cantilever-A with a PDMS sample: $21\,nN$ for different amplitudes. 81
4-15 In-contact frequency response of cantilever-A with a PDMS sample: $35\,nN$ for different amplitudes. 82
4-16 Force displacement curve for cantilever-B with a PDMS sample. 82
4-17 In-contact frequency response of cantilever-B with a PDMS sample: $36\,nN$ for different amplitudes. 83
4-18 In-contact frequency response of cantilever-B with a PDMS sample: $17\,nm$ amplitude for different set-points. 83
4-19 In-contact frequency response of cantilever-B with a PDMS sample: $113\,nN$ for different amplitudes. 83
4-20 Images of calibration steps using a PI controller: (a) scanning simulation, (b) experiment. 84
4-21 Nonlinear voltage to displacement quasi-static curve of piezoelectric tube. . 86
4-22 Experimental hysteresis curves for scanner for a sinusoidal input at $10\,Hz$: $20\,V$, $50\,V$ and $100\,V$. 86
4-23 Hysteresis loops: experiments vs. simulations using the Bouc-Wen model. . 87
4-24 Hysteresis loops: experiments vs. simulations using the Coleman model. . . 87
4-25 Pre-data collection drift in PSD signal. 89
4-26 Experimental creep response: Linearity of response. 90
4-27 Creep response to inputs with different rates. 90

4-28 LTI creep model fitted to experimental responsc: insert shows a zoom on initial part of response. 91
4-29 Logarithmic creep model fitted to experimental response. 91
4-30 Creep response comparison between a single 340 nm step and two 170 nm steps. 91

5-1 Feedback block diagram with creep compensation filter. 93
5-2 Feedback block diagram with creep compensation filter. 94
5-3 AFM image of 530 nm Silicon steps, with and without creep compensation, 2.8 $\mu m/s$. 95
5-4 AFM image of 530 nm Silicon steps, with creep compensation, 17.5 nm/s. . 95
5-5 AFM image of 530 nm Silicon steps, without creep compensation, 17.5 nm/s. 96
5-6 AFM image of 1590 nm Silicon steps, with creep compensation, 10 $\mu m/s$. . 96
5-7 AFM image of 1590 nm Silicon steps, with creep compensation, 41.67 nm/s. 97
5-8 AFM image of 1590 nm Silicon steps, without creep compensation, 41.67 nm/s. 97
5-9 Locations for laser spot alignment for X and Y creep identification. . . . 100

6-1 Dependance of probe vertical speed on local slope at contact point. 103
6-2 Ratio of zero-deformation force to pull-off force vs. λ. 104
6-3 Contact radius vs. contact force for different values of λ. 104
6-4 Block diagram of the AFM feedback system. 106
6-5 Representative frequency response of G_p. 106
6-6 Loop transfer function frequency response of experimental data with integral control. 109
6-7 Control sensitivity function frequency response of experimental data with integral control. 109
6-8 Sensitivity function frequency response of experimental data with integral control. 109
6-9 Oscillations due to scanner bending mode in experimental AFM image of a 1046 nm Silicon step. 110
6-10 Step response of three transfer functions with a complex zero-pair 112

6-11 Step response of three transfer functions with a single real pole demonstrating trade-off. 112
6-12 Simulated frequency response between input voltage V_z, and the scanner's vertical displacement z_p. 114
6-13 Loop transfer function frequency response with integral control and proper PID controller. 116
6-14 Loop transfer function frequency response with integral control. 117
6-15 Frequency response with integral control: (a) sensitivity function (d_o to y_{PSD}), (b) control sensitivity function (d_o to u), (red) high bandwidth (blue) low bandwidth. 118
6-16 Unit step response in d_o with integral control: (a) sensitivity function (d_o to y_{PSD}), (b) control sensitivity function (d_o to u), (red) high bandwidth (blue) low bandwidth. 118
6-17 Frequency response with integral control: (a) sensitivity function (d_o to y_{PSD}), (b) control sensitivity function (d_o to u), (red) high bandwidth (blue) low bandwidth. 119
6-18 Unit step response in d_o with integral control: (left) sensitivity function (d_o to y_{PSD}), (right) control sensitivity function (d_o to u), (red) high bandwidth (blue) low bandwidth. 119
6-19 Root locus using an integral controller with (a) $G_p(s) = \frac{1}{(\frac{s}{2\pi 380})^2+\frac{0.2s}{2\pi 380}+1}$, (b) $G_p(s) = \frac{(\frac{s}{2\pi 500})^2+\frac{0.4s}{2\pi 500}+1}{(\frac{s}{2\pi 380})^2+\frac{0.2s}{2\pi 380}+1}$. 120
6-20 Schematic of probe sliding on sample. 124
6-21 Force vs. scanner displacement: identifying DC gain, pull-off point, and in-contact output signal noise. 126
6-22 Estimate of $|\hat{L}(j\omega)|$, $|\hat{S}(j\omega)|$, and $|\hat{S}_u(j\omega)|$ using Welch's averaged periodogram method. 127
6-23 AFM images of Silicon steps: (a) PID controller with default parameter values, (b) I-controller using proposed tuning method. 128
6-24 AFM feedback block digram with a feedforward term. 129
6-25 Conventional scan voltage signals and resulting probe trace. 131

6-26 New proposed scan voltage signals and resulting probe trace. 132
6-27 Imgae of a step scanned at $30\,\mu m/s$. 148
6-28 Set-point Error in $\AA$ for image of a step scanned at $30\,\mu m/s$. 148
6-29 Set-point Error in $\AA$ for image of a step scanned at $30\,\mu m/s$. 148
6-30 Image of a step scanned at $70\,\mu m/s$. 149
6-31 Zoom on top left of step image scanned at $70\,\mu m/s$. 149
6-32 Zoom on bottom right of step image scanned at $70\,\mu m/s$. 149
6-33 Set-point Error in $\AA$ for step image scanned at $70\,\mu m/s$. 150
6-34 AFM image convolution due to finite size of the probe. 150

Chapter 1

Introduction

1.1 Background

The field of nanotechnology has rapidly evolved over the years, as a result of a great interest in sub-micron research studies and applications. This interest has been supported by both academia and industry. For example, in fields like physics, biology, and chemistry, there is a need to perform experimental studies to understand phenomena at molecular and atomic levels. As for practical applications, there has been vast interest in miniaturization of macro-machines and devices. The goal is to allow for integration of sensors, actuators, and electronics to create the so-called micro and nano-machines. Accordingly, new challenges and technical problems are created both at the basic research and practical levels. The challenges span a wide range of fields of science and engineering. One of such challenges is the ability to characterize surfaces and material properties at the sub-micron level. Several tools are now available for this task, including scanning electron microscope (SEM) , transmission electron microscope (TEM), and scanning probe microscopes (SPM), including scanning tunneling microscope (STM), and atomic force microscope (AFM). Each of these tools has its strengths and weaknesses, and in cases they may complement each other. However, AFM offers very high resolution (10 nm lateral, 0.05 nm vertical are typical), compatibility with different types of samples and operating media, and generally requires no sample preparation. This has made the AFM a widely used instrument in many disciplines.

An AFM consists of a cantilever-mounted probe, a sensor measuring the deflection of the cantilever, and a scanner providing three dimensional relative motion between the probe and a sample. In contact-mode, the probe is brought into contact with the sample, at a user-specified contact force or cantilever deflection. The scanner is then moved in a raster fashion. During scanning, changes in the sample topography change the cantilever deflection. A controller is used to maintain the deflection constant by moving the scanner up and down. The sample image is composed of the correcting voltage sent to the scanner.

Since its invention [12], as a tool for measuring surface topography, AFM has been used in a wide range of fields and applications. In materials research, it has been used for studying indentation, friction, fracture, adhesion, and wear at the nano-scale [1]. Such studies have great practical importance. For example, there is a great interest in designing materials for bearings for micro-machines that have good tribological properties and can be fabricated using MEMS fabrication techniques. AFM is also used in studying mechanical and chemical properties of polymers to aid in their design for various applications. In medicine and biology, researchers have used AFM to investigate atenzymatic degradation of DNA, mechanics of single molecule domains [2], observation of infection of a cell by viruses, imaging living human platelets during their activation, and in cardiovascular research [87]. In the field of semiconductors, AFM is being used for surface roughness measurements of fabricated surfaces, in IC failure analysis, and for investigating nano-lithography (30 nm patterning resolution [88]). For data storage media, AFM is used for analyzing surface defects in compact disk drives, and investigating future technologies. Also, it has been used in applications such as manipulation of micro and nano-particles, fabrication of a single electron tunneling transistor, and quantum effect electronic devices.

1.2 Technical Challenges and Research Objectives

The wide use of AFM in various fields has imposed ever-increasing stringent requirements on its performance. At the Mechatronics Research Laboratory (MRL), at MIT, AFM has been used in a high-precision metrology application for samples with ultra-sharp features. In our experience and from experiences of other researchers from different disciplines, some limitations of current AFM technology were encountered. In applications like metrology, manipulation of nano-particles, nano-lithography, and read/write for high-density data storage media, it is required to achieve high image accuracy, repeatability, and precise positioning. Among the factors limiting AFM performance and repeatability are undesirable dynamics of the instrument. This can be attributed partly to user choice of operating environment, cantilever (its stiffness, resonant frequency, probe size, etc.), scan parameters (scan speed, force set-point, etc.), and feedback parameters [3]. Usually, AFM users start with some default values of the parameters. In a trial and error manner, parameters are adjusted until a reasonable image is collected. Alternatively, the image may be collected, for the same scan line, in both scan directions instead of only one. The resulting images are called trace and retrace images. If both look *similar*, then the scan parameters used are considered good. It is therefore of great practical value to be able to select key scan parameters in a systematic and automated fashion. This can improve repeatability, accuracy, and consistency. In addition, it aids in fully automating AFM technology for applications such as quality control in semiconductor industry.

Atomic force microscopes may generate erroneous data. To demonstrate this, a commercial AFM was used to scan a set of Silicon calibration steps. The AFM was run under a proportional-plus integral (PI), control. A Silicon Nitride cantilever was used with a resonant frequency of 13 kHz, and stiffness of 0.2 N/m. Scan results demonstrate the high sensitivity of collected images to scan and controller parameters (K_p and K_i). Comparing Figure 1-1 (a) (72 $\mu m/s, K_p = K_i = 2$) to Figure 1-1 (b) (96 $\mu m/s, K_p = K_i = 20$), some of the effects of scanning speed and controller gains on the image can be seen. Higher gains result in oscillations as the cantilever falls along the right edge of the step, with peaks indicating momentary loss of contact between the probe and the sample. The sharp peak on

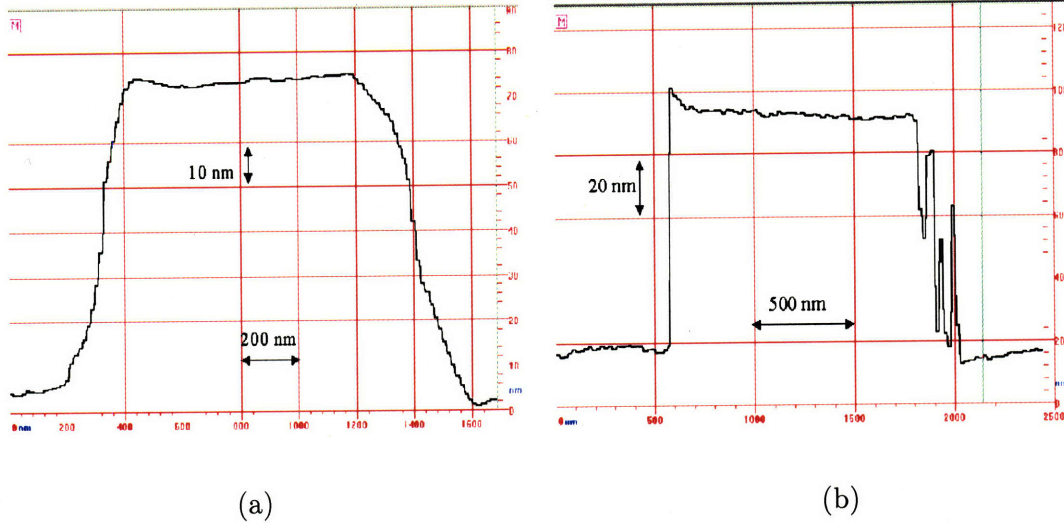

(a) (b)

Figure 1-1: AFM images: (a) $72\,\mu m/s, K_p = K_i = 2$, (b) $96\,\mu m/s, K_p = K_i = 20$.

the left edge of the step, Figure 1-1 (b), can be attributed to a high scan speed compared to closed loop bandwidth. The higher gains improve tracking, as the sharp left edge of the step is resolved more accurately. Figures 1-2 (a) and (b) were generated with a scan speed of 180 $\mu m/s$ using the same controller gains. The contact force set-point for Figure 1-2 (a) is set to the manufacturer's recommended value, while Figure 1-2 (b) a smaller force was used. Choosing a small contact force set-point reduces contact deformation and friction, however, it reduces stability of the contact. As seen from Figure 1-2 (b), the image generated with a small contact force has erroneous height information, due to loss of contact between the probe and the sample.

Furthermore, there are several factors that limit the AFM performance. The inherent piezoelectric scanner nonlinear sensitivity, hysteresis, creep, and cross-coupling between motion in different axes greatly affect imaging and positioning performance. Artifacts due to scanner creep are depicted in Figure 1-3 (a), where the scan direction is now along the steps. As the scanner creeps at the top of the step, the deflection of the cantilever changes. The controller compensates for it by applying a correcting voltage. This correcting voltage appears as part of the sample image. The change in step height in Figure 1-3, occurs over a time scale of 6 s. This is much slower than the response time of the feedback loop (about 50 ms for the gains used), hence, this decay is not due to transient response of the piezo-

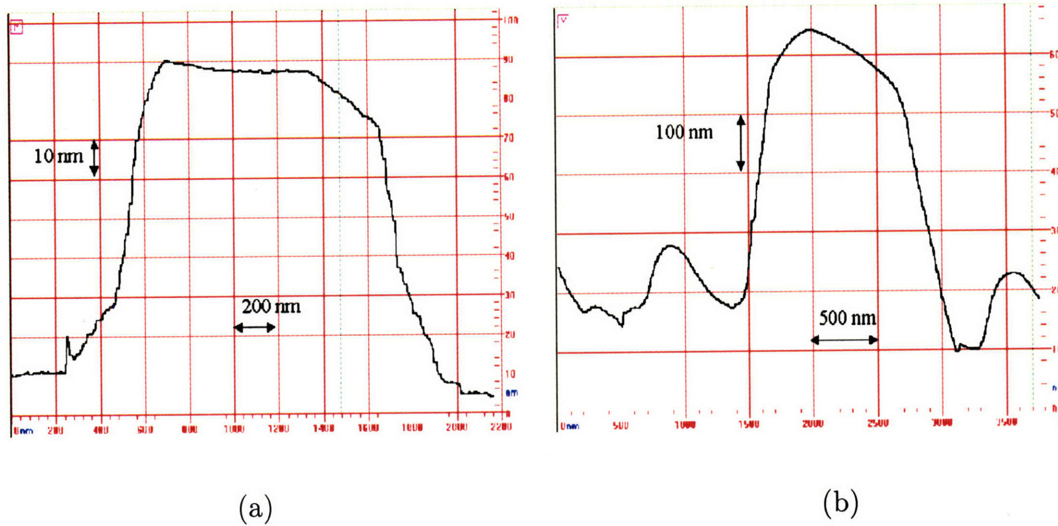

(a) (b)

Figure 1-2: AFM images: 180 $\mu m/s$, (a) nominal contact force, (b) smaller contact force.

electric scanner. Presence of creep can, therefore, introduce artificial shadows and ridges in the image near steep slopes. Moreover, scanner hysteresis can be as much as 25%, and could cause shifts in the image both vertically and laterally. Further, commercial AFMs are usually controlled by a PID controller. A fixed PID controller offers reasonable performance with only few parameters to tune. AFM is used with a wide range of samples having different effective stiffnesses, and with cantilevers that vary greatly in stiffness and resonant frequency. Typical stiffness and resonant frequency values for contact-mode cantilevers are 0.01 to 1.2 N/m, and 10 to 90 kHz, respectively. The operating environment can be air, vacuum, or fluid. Consequently, there is a large range of uncertanties in the system due to the changing nature of AFM operation. The wide range of uncertanties, in addition to non-linearities in the piezoelectric scanner, impose additional limitations on the performance of the feedback system and hence, the AFM. Cantilever thermal noise, laser back-action, and mechanical vibrations also affect performance by increasing the noise floor of the machine. Other sources limiting performance that have a less dynamic nature include convolution errors due to the finite probe size.

One possible approach for improving fidelity and repeatability of AFM images may be through improving its dynamic response by integrating and automating scan parameter selection and control to guarantee consistent performance. Therefore, factors affecting image

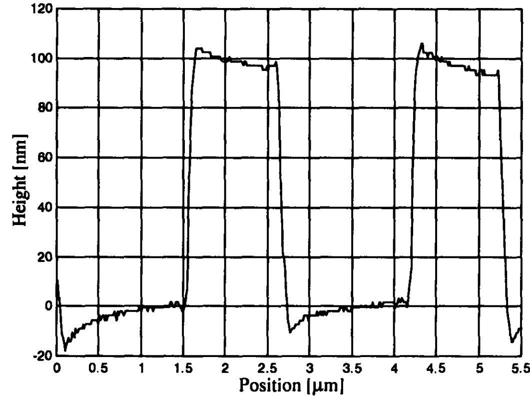

Figure 1-3: AFM image of Silicon Steps: image artifacts due to scanner creep.

formation and their impact on performance of the AFM, need to be identified and understood. This may be achieved through modeling of the main components of the AFM and the dynamic interactions between them.

1.3 Literature Survey

1.3.1 Modeling

In the last few years, researchers' efforts have focused on modeling AFM components independently. Three main components are of interest, namely the piezoelectric scanner, the cantilever, and probe-sample interactions. Linear dynamic models of an ideal uncoupled piezoelectric tube are available [5, 4, 80]. They are based on theory of thin-walled members and describe the longitudinal (extension), and the lateral dynamics independently, neglecting coupling between motion in different axes. Moreover, these models do not describe creep and hysteresis which have great impact on performance. Several models of hysteresis in ferroelectric and piezoelectric materials have been proposed in the literature [81, 19, 20, 21, 22, 23, 24, 25, 26, 27, 28, 10]. Some have received attention from researchers, such as Maxwell and Priesach's models. These models are generally less suitable for feedback control analysis and design. They are composed of many operators or elements connected in parallel . Hence, a large number of operators is needed to reproduce experimental hysteretic behavior. The resulting model will have too many parameters which makes pa-

rameter identification from experimental data complicated. Hence these models are rarely used in practice. Another class of hysteresis models is in the form of a first order nonlinear ordinary differential equation. These models have a small number of parameters and can provide more insight for control analysis and design. Little work has been done to study these models in the context of control. Similarly, modeling of creep for control applications has not had attention in the literature. In applications where feedback control is utilized, integral action in the controller will suffice in reducing the effect of creep on positioning accuracy. However, for open loop applications where calibration of the actuator is relied on (e.g. AFM), there is a great interest to model and control the creep phenomenon. In [90], a common model consisting of a logarithmic equation was used to predict creep in the step response of a piezoelectric actuator. The same model was used in [91], to compensate for creep in step response. As will be seen in Section 4.9, this model is not physically accurate and can not be used to predict creep for general excitation signals.

Tip-sample interaction forces could be due to different mechanisms. Dominant interactions depend on operating conditions and operating mode. Continuum mechanics has been used to model single asperity nano-contact. Experimental results support the adequacy of these models [89]. In general, surface forces of different origins may be present [50]. This may include van der Waals, capacitance, magnetic, or capillary forces. Simplified models have been proposed in the literature.

For modeling of the cantilever, elementary beam theory has been used to develop models for the flexural deflection. Most of the simulation studies available in the literature have used a single-mode model. Moreover, the majority of the models available describe the cantilever dynamics during intermittent or non-contact mode operation at a single point on the sample [17, 47, 48, 49]. This can be schematically represented as in Figure 1-4. Little work has been done to investigate dynamic response during scanning or in contact-mode. This is a more involved task that requires analyzing the closed loop dynamic response, and interactions between the cantilever and the piezoelectric scanner. It can be seen from this survey that models that were available in the literature are incapable of capturing the overall dynamics of the AFM. Therefore, there is a need for a competent model of the AFM.

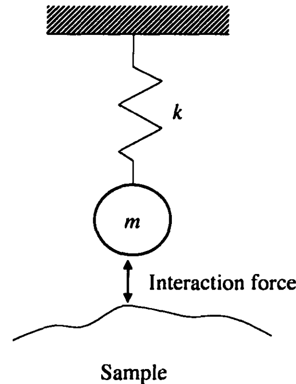

Figure 1-4: Schematic of an AFM model that has been commonly used in the literature.

1.3.2 Control

There has not been, to the best of the author's knowledge, published work directly aiming at automating the selection of scan parameters. A work that is of some relevance is [7], where authors examined the limits of scan speed in different operating media by considering only the cantilever and not including the piezoelectric scanner or the overall feedback system.

Published work on feedback control of AFM as a whole system was not available in the literature, to the best of the author's knowledge. However, there has been published work on control of a piezoelectric tube scanner as a stand-alone actuator [8, 9]. Both references relied on experimentally identified transfer functions to model the scanner lateral and longitudinal dynamics, respectively. In addition, a displacement sensor was used for feedback which is not commonly available in most AFMs. The models were 2nd and 4th order, respectively. In [8], both lead-lag and an H_∞ controller were designed and their performance tracking a triangular wave was tested. On the other hand, in [9], a PI controller was designed and small-amplitude step response was used to test the controller's performance. On control of piezoelectric actuators in general, there have been many contributions by different authors. Researchers have taken three main approaches. One approach involved driving the actuator with a charge amplifier instead of a voltage amplifier [83]. This results in reduction of the hysteretic behavior at the expense of reduced displacement sensitivity, increased charge leakage and hence actuator drift, and a more expensive implementation. As a result, charge drivers are rarely used in practice. Other researchers have used fixed feedforward control

as in [82, 43], and adaptive feedforward control as in [84]. In both cases the models used were composed of a number of hysteretic operators in parallel. Using a small number of operators can result in discontinuities in the hysteresis curve. A large number of operators was needed [84], making the number of adaptation parameters 30. This may reduce the maximum bandwidth of the closed loop system due to computational delays (20 Hz was reported). The results also did not include mechanical dynamics of the actuator. Alternatively, feedback control was used on linearized models of hysteresis to design an H_∞ linear fixed controller. Others developed adaptive inverse feedback control [86]. However, the model used assumes that the hysteresis loop is quadrilateral which is a very crude model of hysteresis. The aforementioned work on feedback control of piezoelectric actuators assumes that the actuator's displacement is measured, and that there are no other dynamics besides those of the actuator. Finally, the body of literature available on adaptive control is too large to list. References used in this work will be cited where relevant.

1.4 Thesis Overview

Despite the aforementioned results, a competent model describing the overall AFM dynamics is still lacking. In addition, there is a need for understanding dynamic interactions between different AFM components and mechanisms by which image artifacts are generated. Further, identification of possible performance limitations and their sources is essential for improving the dynamic response of the AFM. Ultimately, key scan parameters are to be automatically selected to ensure good dynamic response and a high level of data fidelity and repeatability.

In Chapter 2, a detailed dynamic model of the AFM will be presented. It includes models for probe-sample interaction forces, the cantilever, and the scanner. Models for the scanner will include linear coupled dynamics, creep, and hysteresis. Sources of noise and disturbances will also be discussed. A new method for calibrating the vertical displacement of the scanner will be presented in Chapter 3. Experimental validation of the models is provided in Chapter 4, and the results are discussed. In addition, simulation results will also

be presented and compared to experimental data. Compensation for creep and hysteresis will be presented and discussed in Chapter 5. In Chapter 6, fundamental performance limitations of the AFM feedback system will identified and supported by experiments and simulations. Based on the modeling results and the identified fundamental performance limitations, a procedure for parameter and controller gain selection is presented for integral control. The performance of PID and higher order LTI controllers is also discussed. Further, a robust adaptive output controller (RAOC), is designed and stability analysis is provided. Scan and controller parameter selection for the RAOC is also discussed. Finally, conclusions and recommendations are presented in Chapter 7.

Chapter 2

Modeling

2.1 Atomic Force Microscope

As seen in Figure 2-1, an AFM has three main components, namely, a scanner, a cantilever beam-mounted probe, and a cantilever deflection sensor. The scanner, typically a piezoelectric tube, provides three-dimensional relative motion between the probe and the sample. Information on sample topography or local material properties is obtained based on probe-sample interactions. Probe displacement is commonly determined by measuring the slope at the cantilever's free-end using an optical-lever sensor. The optical sensor consists of a laser source and a position sensative diode (PSD). There are two common AFM designs. In the sample-on-scanner design shown in Figure 2-2, the sample is placed on the scanner, while the cantilever is fixed in space. The size and weight of the sample is limited to avoid loading the piezoelectric actuator. The second design, cantilever-on-scanner, involves attaching the cantilever to the scanner while the sample is placed on a coarse motion stage that does not move during scanning. Two variants of this design are popular, namely, a single-scanner and a two-scanner design. In the two-scanner design of Figure 2-3 (a), two separate piezoelectric tubes are attached to each other. The top tube is typically dedicated to lateral motion, whereas the bottom tube provides vertical motion. In this design, the effect of vertical motion on the lateral motion is reduced. In the single-scanner design depicted in Figure 2-3 (b), a piezoelectric tube is used to provide both lateral and vertical motions. In addition, an extension tube attached to the scanner is used to provide means for attaching lenses for

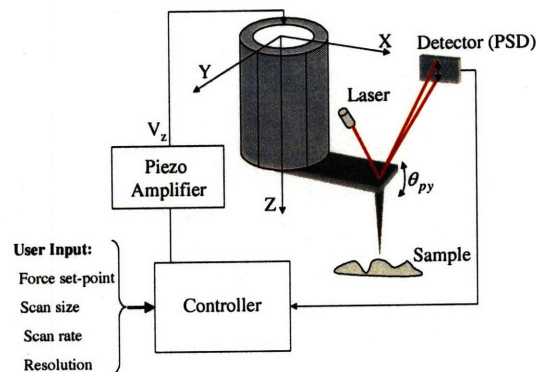

Figure 2-1: Schematic of the main components of an AFM.

the optical-lever sensor. Moreover, it provides additional mechanical amplification of the lateral motion; extending the lateral range of the scanner. Models presented later in this chapter will be for the more popular design; model of Figure 2-3 (b).

Atomic force microscopes have three main imaging modes, namely, contact [12], non-contact [13], and intermittent [14]. In contact-mode, the probe presses against a sample exerting a vertical force proportional to the cantilever's deflection. The probe is then dragged against the sample along each scan line in a raster fashion. The slope at the cantilever's free-end is measured and fed back. During scanning, a controller maintains a constant cantilever slope by adjusting the vertical extension of the piezoelectric scanner. Changes in the extension of the scanner are therefore, related to changes in the sample topography. This is known as the constant-force contact mode which will be the focus of this thesis. The cantilever and its holder are mounted on a piezoelectric crystal. This crystal is used in non-contact mode to vibrate the cantilever near its resonance frequency, while hovering above the sample surface. Surface forces between the sample and the probe change the amplitude of oscillation. The change is detected and fed back to maintain a constant vibration amplitude during scanning. Alternatively, a phase-lock circuit may be used as a feedback signal. Intermittent mode is very similar to the non-contact mode, except that the probe is brought closer to the sample until intermittent contact occurs, i.e. tapping.

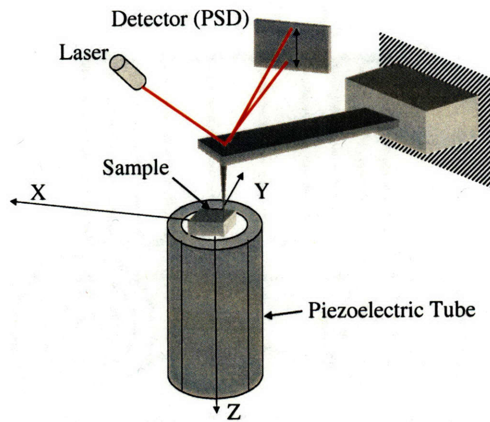

Figure 2-2: Sample-on-scanner design of AFM.

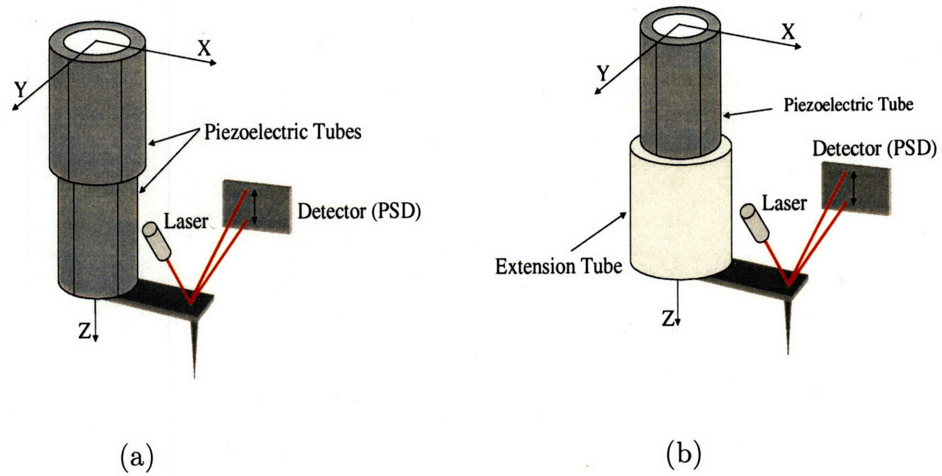

(a) (b)

Figure 2-3: Cantilever-on scanner design of AFM, (a) two-scanner design, (b) single-scanner design.

2.2 Probe-sample Interactions

Depending on the operating environment of the AFM, different probe-sample forces may be present. These forces can be classified as long-range and short-range forces. Long-range forces can be due to different origins; electrostatic, electrodynamic, and liquid forces. Short-range forces could be due to chemical or metallic bonding. Atomic force microscopes are generally operated in Air, vacuum, dry Nitrogen, or in a suitable liquid. Operation in vacuum or dry Nitrogen reduces capillary effects. Liquids are typically used to reduce surface forces such as van der Waals forces. The choice of operation medium strongly depends on the sample under consideration. In this section, in-contact, out-of-contact, and lateral forces will be discussed.

2.2.1 In-contact Interactions: Vertical Forces

The starting point for modeling probe-sample contact is deciding on the dominant surface forces. In this thesis, the focus will be on AFM operation in Air, which is the most common and versatile medium. Capillary and adhesion forces are commonly present due to contaminants in Air. As a result, a meniscus forms around the probe and sample when in close proximity holding them together even in the absence of an externally applied load.

The model presented here was first introduced by Maugis [15]. It describes the adhesion contact of two elastic spheres each with a radius R_i and elastic modulus of elasticity E_i, and Poisson's ratio ν. The Dupré work of adhesion is w. Maugis was able to obtain a closed-from solution by modeling surface forces using a Dugdale approximation. As shown in Figure 2-4, the Dugdale attractive force σ_o, is assumed constant for atomic planes separation h, such that $z_o \leq z_o + h \leq z_o + h_o$, where, z_o is the equilibrium separation of the atoms. For $h > h_o$, $\sigma_o = 0$. Maugis selected the value of σ_o to match the Lennard-Jones potential, Figure 2-4 (a), obtaining a value of $h_o = 0.97 z_o$. Figure 2-5 gives a schematic representation of the contact. For ease of visualization, one surface is represented as flat while the other surface has a radius of curvature equal to the reduced radius of the spheres $R = (\frac{1}{R_1} + \frac{1}{R_2})^{-1}$. Both surfaces mate over the central region $r \leq a$, with a separation h existing over $a \leq r \leq c$,

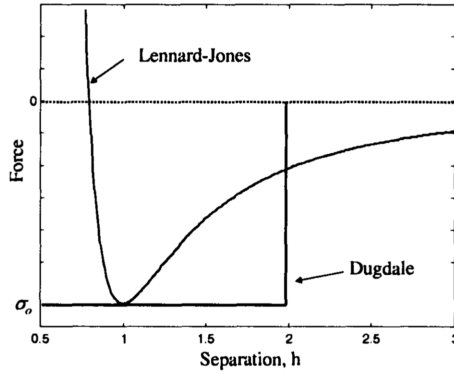

Figure 2-4: Force law for Lennard-Jones potential and Dugdale approximation in arbitrary units.

and increasing from zero to h_o. Over the central region, the total pressure distribution $p(r)$, as shown in Figure 2-5, is composed of Hertzian pressure $p_h(r)$, plus adhesion stress $p_a(r)$, and is given by

$$p(r) = p_h(r) + p_a(r), \quad p_h(r) = \frac{2E^*a}{\pi R}[1 - (\frac{r}{a})^2]^{\frac{1}{2}} \tag{2.1}$$

$$p_a(r) = -\frac{\sigma_o}{\pi} cos^{-1}(\frac{2a^2 - c^2 - r^2}{c^2 - r^2}) \tag{2.2}$$

where the combined elastic modulus for the spheres is $E^* = [\frac{1-\nu_1^2}{E_1} + \frac{1-\nu_2^2}{E_2}]^{-1}$. For $a \leq r \leq c$, the stress distribution is only due to adhesion and is constant $p(r) = -\sigma_o$. The total contact force $F_{con} = F_h + F_a$ is positive when compressive and is expressed as

$$F_{con} = \frac{4E^*a^3}{3R} - 2\sigma_o c^2[cos^{-1}(\frac{a}{c}) + a\sqrt{c^2 - a^2}] \tag{2.3}$$

The model predicts the relative displacement δ, of two points on the spheres located far away from the contact area as

$$\delta = \delta_h + \delta_a = \frac{a^2}{R} - \frac{2\sigma_o}{E^*}\sqrt{c^2 - a^2} \tag{2.4}$$

Moreover, the total separation between both surfaces at $r = c$, is h_o, hence

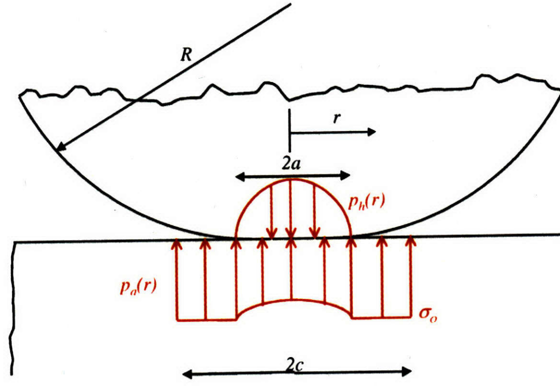

Figure 2-5: Schematic of the contact showing stress distribution.

$$\begin{aligned} h_h(c) &= \frac{c^2}{2R} - \frac{a^2}{R} + \frac{[(2a^2 - c^2)sin^{-1}(\frac{a}{c}) + a\sqrt{c^2 - a^2}]}{\pi R} \\ h_a(c) &= \frac{4\sigma_o}{\pi E^*}[\sqrt{c^2 - a^2}cos^{-1}(\frac{a}{c}) + a - c] \\ h_o &= h_h(c) + h_a(c) = \frac{w}{\sigma_o} \end{aligned} \tag{2.5}$$

Maugis introduced a non-dimensional transition parameter λ; defined as $\lambda = \sigma_o(\frac{9R}{2\pi w E^{*2}})^{\frac{1}{3}}$. This transition parameter can be viewed as the ratio of elastic deformation to the effective range over which surface forces act. From its definition, it follows that large values of λ correspond to compliant (small E^*), large spheres (R), and small adhesion (w) contacts, whereas small values are for stiff small spheres with high adhesion. Equations (2.3,2.4,2.5) form the Maugis model which can be solved numerically. The model equations were non-dimensionalized by introducing the following non-dimensional variables

$$\begin{aligned} \overline{a} &= a(\frac{4E^*}{3\pi w R^2})^{\frac{1}{3}}, \quad \overline{c} = c(\frac{4E^*}{3\pi w R^2})^{\frac{1}{3}}, \quad m = \frac{c}{a} \\ \overline{F}_{con} &= \frac{F_{con}}{\pi w R}, \quad \overline{\delta} = \delta(\frac{16E^{*^2}}{9\pi^2 w^2 R})^{\frac{1}{3}} \end{aligned} \tag{2.6}$$

Using (2.6) and the definition of λ, the model can be expressed in non-dimensional form as

$$\begin{aligned}
\overline{\delta} &= \overline{a}^2 - \frac{4\lambda\overline{a}}{3}\sqrt{m^2-1} \\
\overline{F}_{con} &= \overline{a}^3 - \lambda\overline{a}^2[\sqrt{m^2-1} + m^2 sec^{-1}(m)] \\
1 &= \frac{\lambda\overline{a}^2}{2}[(m^2-2)sec^{-1}(m) + \sqrt{m^2-1}] + \\
&\quad \frac{4\lambda^2\overline{a}}{3}[\sqrt{m^2-1}sec^{-1}(m) - m + 1]
\end{aligned} \tag{2.7}$$

The use of continuum models to describe nano-contacts has been supported by experiments as in [89], and in Section 4.4 of this thesis. The level at which continuum models break-down is not all clear.

2.2.2 In-contact Interactions: Lateral Forces

As the probe is dragged against the sample while in contact, a frictional shear force develops. Based on contact load and possibly scan speed, this frictional interaction may involve sliding and atomic stick-slip behavior. The nature of this atomic friction is not well understood and is currently an active area of research. In [74], experiments on mica have shown that in the absence of wear, the average friction force is directly proportional to contact area a_c, $F_f = \tau a_c$, where τ is the shear strength. For this work, the interest is in simulating the effect of sliding friction force on the cantilever dynamics during scanning. As a first order approximation, it will be assumed that the instantaneous friction force is directly proportional to the instantaneous contact area ($\sim a^2$), as shown below

$$F_f(t) = G\,a^2(t) \tag{2.8}$$

where G is a proportionality constant ($\sim$ shear strength of the contact junction). This model does not consider any explicit dependence of friction on scanning speed. Although contact models were originally developed for static loading, it has been shown in [74], that it holds under sliding conditions with not very high sliding speeds. When the probe and sample are out of contact the friction force is set to zero.

2.2.3 Out-of-contact Interactions: Vertical Forces

When the probe and sample are not in contact, surface forces acting on the probe may be due to different sources. This may include magnetic, capacitance, patch-charge, and van der Waals forces, to name a few. The presence of multiple forces could modify the shape of the force-separation curve. In general, these surface forces may depend on the geometry of probe and sample, their permittivity and that of the operating medium and probe-sample separation. The main characteristics of the attractive interactions could be captured by a simple van der Waals forces model. It is therefore, assumed that van der Waals forces between two spheres are the dominant interaction. The attractive surface force is then given as

$$F_{oc}(\delta) = -\frac{HR}{6(\delta - \epsilon_o)^2} \tag{2.9}$$

where H is Hamaker constant, and ϵ_o is an offset constant.

2.2.4 Point of Contact

In [15], it was shown that in the limit when $\overline{a} \rightarrow 0$, $\overline{F}_{con}$ and $\overline{\delta}$ reduce to,

$$\overline{\delta} \simeq \frac{-8}{9\pi}[\sqrt{4\lambda^4(\pi-2)^2 + 9\pi\lambda} - 2\lambda^2(\pi-2)] \tag{2.10}$$

$$\overline{F}_{con} \simeq -2 + \frac{8\lambda(\pi-2)}{9\pi}[\sqrt{4\lambda^4(\pi-2)^2 + 9\pi\lambda} - 2\lambda^2(\pi-2)] \tag{2.11}$$

Equations (2.9,2.11,2.10) can be used to impose continuity on the force-separation curve at the point of atomic contact by adjusting the value of ϵ_o.

2.3 Scanner Model

The piezoelectric scanner is a thin-walled tube. The tube has four electrodes of equal segments on its outer surface, and either a single or four electrodes on its inner surface. Applying a voltage to its inner electrode(s) results in extension motion along the Z axis. Motion in the X or Y direction is generated by subjecting two opposite electrodes to two voltage signals that have the same magnitude but opposite phase. The scanner design of Figure 2-3 (b) is considered in this section. The design is shown schematically in Figure 2-6,

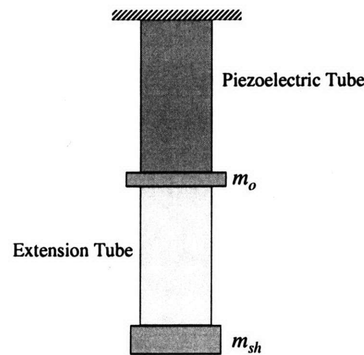

Figure 2-6: Cantilever-on-scanner design: single piezoelectric scanner with extension tube.

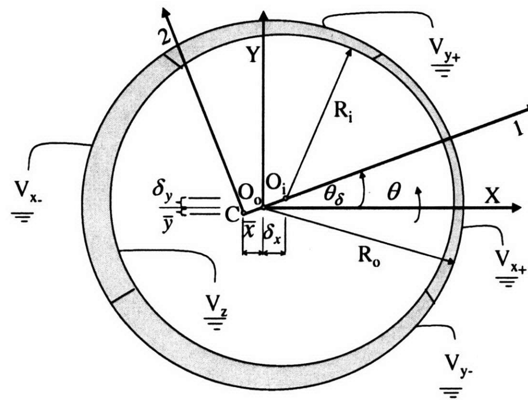

Figure 2-7: Cross-section of the piezoelectric tube.

where m_o represents the mass of an optical lense part of the laser sensor and a fixture joining the piezoelectric and extension tubes together. On the other hand, m_{sh} represents the mass of the sample holder, the piezoelectric crystal, and an additional lense typically placed at the end of the extension tube. The forces that the scanner experiences due to probe-sample interactions are on the order 10^{-12} to $10^{-6}\,N$ and are several orders of magnitude smaller than its force capacity which is typically about $\sim 1\,N$. Consequently, the effect of these minute forces on the scanner will be neglected.

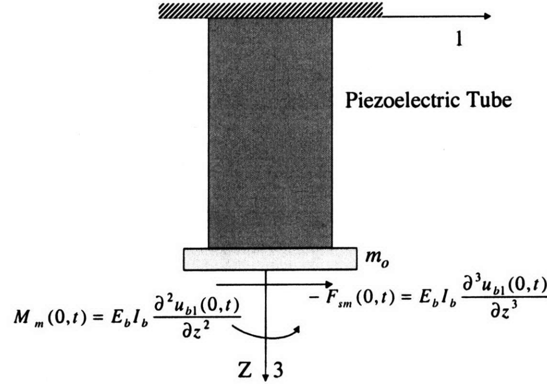

Figure 2-8: Free body diagram of the piezoelectric tube for lateral dynamics.

2.3.1 Piezoelectric Tube Lateral Dynamics

In [5, 4], a model for an ideal uncoupled tube scanner was presented. Due to inevitable machining tolerances, some eccentricity is always present in the tube, typically a maximum of $50\,\mu m$ for a $12.7\,mm$ diameter tube [18]. This seemingly small eccentricity is in fact significant since the probe-deflection sensor has typically a sub-Angstrom RMS resolution. The newly developed model presented within is based on two eccentric cylinders, as shown in Figure 2-7, with eccentricity δ_x and δ_y from the geometric center of the outer cylinder O_o. The outer and inner radii are R_o and R_i, respectively. The angle θ is measured from the X-axis. The tube is fixed at one end, while a mass m_o is rigidly attached to the other end. In addition, a concentrated moment and a shear force act on m_o as reactions from the extension tube, as shown in Figure 2-8.

The model is based on elementary bending theory for thin-walled members. The main assumptions are small deformations and angles, that plane sections of the tube remain plane after deformation, material is linear elastic, and negligible effects of rotatory inertia and shear deformation. The rotatory inertia of the end mass m_o and extension tube are also neglected. The first step in deriving the model is finding the centroid C of the cross section. The coordinates of the centroid $\bar{x}$ and $\bar{y}$ relative to O_o are giving by

$$\bar{x} = \frac{\int x dA}{\int dA} = \frac{\int_0^{2\pi} \int_{R_i(\theta)}^{R_o} r^2 cos(\theta) dr d\theta}{\pi(R_o^2 - R_i^2)} \tag{2.12}$$

$$\bar{y} = \frac{\int y dA}{\int dA} = \frac{\int_0^{2\pi} \int_{R_i(\theta)}^{R_o} r^2 sin(\theta) dr d\theta}{\pi(R_o^2 - R_i^2)} \tag{2.13}$$

where

$$R_\delta = \sqrt{\delta_x^2 + \delta_y^2}\ , \quad \theta_\delta = tan^{-1}(\frac{\delta_y}{\delta_x})$$

$$R_i(\theta) = R_\delta cos(\theta - \theta_\delta) + \sqrt{R_i^2 - R_\delta^2 \, sin^2(\theta - \theta_\delta)}$$

For a positive δ_x and δ_y, the centroid will be located below and to the left of O_o. Because of the eccentricity, the X and Y axes are no longer the principal axes of inertia, i.e. axes along which lateral deflection occurs. The new principal axes of inertia 1 and 2 can be found from symmetry. Axis 1 is along the point of minimum thickness at θ_δ, while the 2-axis is perpendicular to it. The Z-axis (or 3-axis) passes through the centroid C. For thin-walled members, the only stress is assumed to be in the Z-direction. Therefore, the linear constitutive relation for piezoelectric material [34] reduces to

$$\begin{pmatrix} \epsilon_z \\ D_r \end{pmatrix} = \begin{pmatrix} s_{11}^E & d_{31} \\ d_{31} & \epsilon_3^\sigma \end{pmatrix} \begin{pmatrix} \sigma_z \\ E_r \end{pmatrix} \tag{2.14}$$

where σ_z is the stress, ϵ_z is the strain, D_r is the electric displacement, E_r is the applied electric field, and subscript r denotes the radial direction. The electric field E_r will be assumed constant over the tube thickness.

Assuming constant inertia $\rho_p A_p$ per unit length, where ρ_p is the density and A_p is the cross sectional area, the equation of motion in the 1-direction is

$$\rho_p A_p \frac{\partial^2 u_{1p}}{\partial t^2} + b_{p1} \frac{\partial u_{1p}}{\partial t} = \frac{\partial F_{1sp}}{\partial z} \tag{2.15}$$

where b_{p1} is the viscous damping coefficient, and F_{1sp} is the shear force in the 1-direction. The shear force is related to the bending moment by $F_{1sp} = -\partial M_{2p}/\partial z$, where the bending moment is given by

$$M_{2p} = -\int\int r cos(\theta + \theta_\delta)\, \sigma_z \, d\theta \, dr \tag{2.16}$$

In Equation (2.16), the limits of integration with respect to r are from R_{C_i} to R_{C_o}; the

distances from C to the inner and outer cylinders, respectively. The variation of the radii with respect to θ, is given by

$$R_{C_i}(\theta) = R_{CO_i}cos(\theta - \theta_\delta) + \sqrt{R_i^2 - R_{CO_i}^2 sin^2(\theta - \theta_\delta)} \quad (2.17)$$

$$R_{C_o}(\theta) = R_{CO_o}cos(\theta - \theta_\delta) + \sqrt{R_o^2 - R_{CO_o}^2 sin^2(\theta - \theta_\delta)} \quad (2.18)$$

and

$$R_{CO_i} = \sqrt{(\bar{x} - \delta_x)^2 + (\bar{y} - \delta_y)^2}$$

$$R_{CO_o} = \sqrt{(\bar{x}^2 + \bar{y}^2)}$$

where R_{CO_i} and R_{CO_o} are the distances from C to O_i and O_o, respectively, and R_i and R_o are the radii of the inner and outer cylinders measured from their own geometric center as seen in Figure 2-7. Substituting the first equation of (2.14) into (2.16) and integrating with respect to r, leads to

$$\begin{aligned} M_{2p} &= \int_0^{2\pi} (\frac{(R_{Co}^4(\theta) - R_{Ci}^4(\theta))\, cos^2(\theta + \theta_\delta)}{4\, R_{curv_{1p}}\, s_{11}^E} \\ &\quad - \frac{d_{31}(R_{Co}^3(\theta) - R_{Ci}^3(\theta))cos(\theta + \theta_\delta)E_r}{3s_{11}^E})d\theta \\ &= \frac{\alpha_{u_{1p}}}{s_{11}^E\, R_{curv_{1p}}} + M_{2_V}(V) \qquad (2.19) \\ M_{2_V} &= -\int_0^{2\pi} \frac{d_{31}(R_{Co}^3(\theta) - R_{Ci}^3(\theta))cos(\theta + \theta_\delta)V(\theta)}{3s_{11}^E(R_{Co}(\theta) - R_{Ci}(\theta))}d\theta \end{aligned}$$

$$V(\theta) = \begin{cases} V_{x_+} - V_z & -\frac{\pi}{4} < \theta < \frac{\pi}{4} \\ V_{y_+} - V_z & \frac{\pi}{4} < \theta < \frac{3\pi}{4} \\ V_{x_-} - V_z & \frac{3\pi}{4} < \theta < \frac{5\pi}{4} \\ V_{y_-} - V_z & \frac{5\pi}{4} < \theta < \frac{7\pi}{4} \end{cases} \quad (2.20)$$

$$M_{2_V} = -\frac{d_{31}}{s_{11}^E}[\gamma_{x_+}V_{x_+} + \gamma_{x_-}V_{x_-} + \gamma_{y_+}V_{y_+} + \gamma_{y_-}V_{y_-} + \gamma_z V_z] \quad (2.21)$$

and

$$M_{2_V} = -\frac{d_{31}}{s_{11}^E}\sum_j \gamma_j V_j$$

$$\gamma_{x_+} = \int_{-\pi/4}^{\pi/4} \frac{(R_{Co}^3(\theta) - R_{Ci}^3(\theta))cos(\theta + \theta_\delta)}{3(R_{Co} - R_{Ci})}\, d\theta$$

$$\gamma_z = \int_0^{2\pi} \frac{(R_{Co}^3(\theta) - R_{Ci}^3(\theta))cos(\theta + \theta_\delta)}{3(R_{Co} - R_{Ci})} d\theta$$

where M_{2p} is the bending moment about the 2-axis, M_{2_V} is the bending moment about the 2-axis due to the applied voltages, and $R_{curv_{1p}}$ is the radius of curvature of the deformed tube in the $1 - Z$ plane, which is related to u_{1p}, for small deformations, by

$$\frac{1}{R_{curv_{1p}}} = \frac{\partial^2 u_{1p}}{\partial z^2} \tag{2.22}$$

The integrals for the constants α_i and γ_i, do not lead to simple expressions, but can be easily evaluated numerically. Substituting Equations (2.19) and (2.22) into Equation (2.15), results in

$$\rho_p A_p \frac{\partial^2 u_{1p}}{\partial t^2} + b_{p1}\frac{\partial u_{1p}}{\partial t} + \frac{\alpha_{u_{1p}}}{s_{11}^E}\frac{\partial^4 u_{1p}}{\partial z^4} = 0 \tag{2.23}$$

The boundary conditions are zero deflection and slope at the fixed end $z = 0$, and a balance of forces in the 1-direction and zero moment about the 2-axis at the free end. Mathematically, the conditions are

$$\begin{aligned}
&\text{At } z = 0 \\
&u_{1p} = 0 \\
&\frac{\partial u_{1p}(0,t)}{\partial z} = 0 \\
&\text{At } z = L_p \\
&m_o \frac{\partial^2 u_{1p}(L_p,t)}{\partial t^2} + b_{p1}\int_0^{L_p} \frac{\partial u_{1p}(z,t)}{\partial t} dz + \frac{\alpha_{u_{1p}}}{s_{11}^E}\frac{\partial^3 u_{1p}}{\partial z^3} = E_b I_b \frac{\partial^3 u_{1b}(0,t)}{\partial z^3} \\
&\frac{\alpha_{u_{1p}}}{s_{11}^E}\frac{\partial^2 u_{1p}}{\partial z^2} = E_b I_b \frac{\partial^2 u_{1b}(0,t)}{\partial z^2} - M_{2_V}
\end{aligned} \tag{2.24}$$

The concentrated loads depicted in Figure 2-8 appear in the boundary conditions making the boundary conditions time-dependant. As a result the technique of separation of variables could not be used to solve for the deflection. Alternatively, it is possible to use techniques as outlined in [11]. However, the resulting transfer function model of the system would be proper (number of zero equals the number of the poles). Consequently, that model would

not capture the high-frequency magnitude roll-off observed in an experimental frequency response. A low-order model is seeked in this work and therefore, an approximate solution will be used. An nth mode model based on Rayligh-Ritz method will be formulated. The deflection u_{1p} is approximated by a finite sum

$$u_{1p}(z,t) \approx \sum_{i=1}^{n} \psi_{1pi}(z)\, T_{1pi}(t) \tag{2.25}$$

where ψ_{1pi} are trial functions that satisfy the geometric (displacement and rotation) boundary conditions but not necessarly the natural (force and moment) boundary conditions. The reuslting model is

$$M\,\ddot{T}_{1p} + C\,\dot{T}_{1p} + KT_{1p} = Q_{1p} \begin{bmatrix} E_b I_b \frac{\partial^3 u_{1b}(0,t)}{\partial z^3} \\ E_b I_b \frac{\partial^2 u_{1b}(0,t)}{\partial z^2} \\ \frac{d_{31}}{s_{11}^E} \sum_j \gamma_j V_j \end{bmatrix} \tag{2.26}$$

where $T_{1p} = [T_{1p1} \ldots T_{1pi}]^T$, M is the mass matrix, K is the stiffness matrix, C is the damping coefficent matrix, and Q_{1p} is the generalized loads input matrix. The elements of these matrices are given by

$$\begin{aligned} m_{ij} &= \rho_p A_p \int_0^{L_p} \psi_{1pi}(z)\psi_{1pj}(z)dz + m_o \psi_{1pi}(L_p)\psi_{1pj}(L_p) \\ c_{ij} &= b_{p1} \int_0^{L_p} \psi_{1pi}(z)\psi_{1pj}(z)dz \\ k_{ij} &= \frac{\alpha_{u_{1p}}}{s_{11}^E} \int_0^{L_p} \frac{\partial^2 \psi_{1pi}(z)}{\partial z^2} \frac{\partial^2 \psi_{1pj}(z)}{\partial z^2} dz \\ q_{1pi} &= [\psi_{1pi}(L_p) \quad \frac{\partial \psi_{1pi}(L_p)}{\partial z} \quad \frac{\partial \psi_{1pi}(L_p)}{\partial z}] \end{aligned} \tag{2.27}$$

For a two-mode model with $\psi_{1p1}(z) = z^2$ and $\psi_{1p2}(z) = z^3$, the resulting model is given by

$$M = \begin{bmatrix} \rho_p A_p \frac{L_p^5}{5} + m_o L_p^4 & \rho_p A_p \frac{L_p^6}{6} + m_o L_p^5 \\ \rho_p A_p \frac{L_p^6}{6} + m_o L_p^5 & \rho_p A_p \frac{L_p^7}{7} + m_o L_p^6 \end{bmatrix}, \quad Q_{1p} = \begin{bmatrix} L_p^2 & 2L_p & 2L_p \\ L_p^3 & 3L_p^2 & 3L_p^2 \end{bmatrix} \tag{2.28}$$

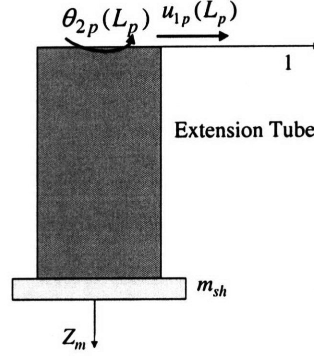

Figure 2-9: Free body diagram of the extension tube for lateral dynamics.

$$C = b_{p1} \begin{bmatrix} \frac{L_p^5}{5} & \frac{L_p^6}{6} \\ \frac{L_p^6}{6} & \frac{L_p^7}{7} \end{bmatrix}, \quad K = \frac{\alpha_{u_{1p}}}{s_{11}^E} \begin{bmatrix} 4L_p & 6L_p^2 \\ 6L_p^2 & 12L_p^3 \end{bmatrix} \tag{2.29}$$

It is worth noting that as a result of machining, actual tubes are not perfectly round. In addition, the wall thickness may vary along the tube's length. This can be handled in the model by using the desired thickness distribution as a function of θ, and depth z, in Equation (2.16). However, this will only change the coefficients γ_i, and α_i slightly, but the structure of the model will remain unchanged. As will be seen later in the thesis, the model indeed retains the correct structure and reproduces experimental results well. Therefore, accounting for the aforementioned thickness variations proved to be unnecessary. Finally, the equation of motion for u_{2p} can be derived similarly.

2.3.2 Extension Tube Lateral Dynamics

As shown in Figure 2-9, the extension tube's lateral deflection in the 1-direction u_{1m}, is measured with respect to the displacement of the piezoelectric tube u_{1p}. Assuming a concentric tube, the equation of motion is given by

$$\rho_m A_m \frac{\partial^2 [u_{1m} + u_{1p}(L_p,t) + z\,\theta_{2p}(L_p,t)]}{\partial t^2} + b_{m1}\frac{\partial u_{1m}}{\partial t} + E_m I_m \frac{\partial^4 u_{1m}}{\partial z_{z_m}^4} = 0 \tag{2.30}$$

where b_{m1} is the viscous damping coefficient, ρ_m is the mass density, and A_m is the cross sectional area. The boundary conditions relative to the piezoelectric tube displacement are

$$\begin{aligned}
&\text{At } z_m = 0 \\
u_{1m} &= 0 \\
\frac{\partial u_{1m}(0,t)}{\partial z_m} &= 0 \\
&\text{At } z_m = L_m \\
m_{sh}\frac{\partial^2 u_{1m}(L_m,t)}{\partial t^2} + b_{m1}\frac{\partial u_{1m}(L_m,t)}{\partial t} &= E_m I_m \frac{\partial^3 u_{1m}}{\partial z_m^3} \\
E_m I_m \frac{\partial^2 u_{1m}}{\partial z_m^2} &= 0 \qquad (2.31)
\end{aligned}$$

The mode shape functions ψ_{1mi} is given by

$$\begin{aligned}
\psi_{1mi} &= B_1(cos(\lambda_{1mi}z) + cosh(\lambda_{1mi}z)) + B_2(cos(\lambda_{1mi}z) - cosh(\lambda_{1mi}z)) \\
&+ B_3(sin(\lambda_{1mi}z) + sinh(\lambda_{1mi}z)) + B_4(sin(\lambda_{1mi}z) - sinh(\lambda_{1mi}z)) \qquad (2.32) \\
& \qquad (2.33)
\end{aligned}$$

Using Equation (2.31), ψ_{1mi} reduces to

$$\begin{aligned}
\psi_{1mi} &= B_{1mi}(cos(\lambda_{1i}z_m) - cosh(\lambda_{1mi}z_m)) + \\
&\frac{cos(\lambda_{1mi}L_m) + cosh(\lambda_{1mi}L_m)}{sin(\lambda_{1mi}L_m) + sinh(\lambda_{1mi}L_m)}(sinh(\lambda_{1mi}z_m) - sin(\lambda_{1mi}z_m)) \qquad (2.34) \\
0 &= \frac{1}{\lambda_{1mi}L_m}(cos(\lambda_{1mi}L_m)cosh(\lambda_{1mi}L_m) + 1) + \\
&\frac{m_{sh}}{\rho_m A_m L_m}(cos(\lambda_{1mi}L_m)sinh(\lambda_{1mi}L_m) - cosh(\lambda_{1mi}L_m)sin(\lambda_{1mi}L_m)) \qquad (2.35) \\
\lambda_{1mi}^4 &= \frac{\rho_m A_m \omega_{1mi}^2}{E_m I_m} \qquad (2.36)
\end{aligned}$$

Equation (2.35), can be solved to obtain the natural frequencies ω_{1mi}. B_{1mi} is an arbitrary constant which can be used to scale the modal mass m_{1mi}. The model mass, modal damping

b_{1mi}, and modal stiffness k_{1mi}, are given by

$$\begin{aligned} m_{1mi} &= \rho_m A_m \int_0^{L_m} \psi_{1mi}^2(z_m)dz_m + m_{sh}\psi_{1mi}^2(L_m) \\ b_{1mi} &= b_{m1}\int_0^{L_m} \psi_{1mi}^2(z_m)dz_m \ , \quad k_{1mi} = \omega_{1mi}^2 m_{1mi} \end{aligned} \tag{2.37}$$

The effect of concentrated displacements are directly included in the temporal modal response which is given by

$$\begin{aligned} Q_{1mi} &= -[\rho_m A_m \int_0^{L_m} \psi_{1mi}(z_m)dz_m + m_{sh}\psi_{1mi}(L_m)]\ \ddot{u}_{1p}\ (L_p,t) \\ &\quad -[\rho_m A_m \int_0^{L_m} z_m\psi_{1mi}(z_m)dz_m + m_{sh}L_m\psi_{1mi}(L_m)]\ \ddot{\theta}_{2p} \end{aligned} \tag{2.38}$$

$$m_{1mi}\ \ddot{T}_{1mi} + b_{1mi}\ \dot{T}_{1mi} + k_{1mi\ 1mi} = Q_{1mi} \tag{2.39}$$

2.3.3 Piezoelectric Tube Longitudinal Dynamics

Under similar assumptions of those in Section 2.3.1, the equation of motion for the tube's extension u_{3p}, Figure 2-10, is given by

$$\rho_p A_p \frac{\partial^2 u_{3p}}{\partial t^2} + b_{p3}\frac{\partial u_{3p}}{\partial t} = \frac{\partial F_{3p}}{\partial z} \tag{2.40}$$

where

$$F_{3p} = \int \sigma_z dA_p \tag{2.41}$$

$$\begin{aligned} &= \frac{1}{s_{11}^E}\int [\epsilon_z - d_{31}E_r]dA_p \\ &= \frac{1}{s_{11}^E}\int \epsilon_z dA_p - \frac{d_{31}}{s_{11}^E}\sum_j \gamma_{3j}V_j \end{aligned} \tag{2.42}$$

and

$$j = x+, x-, y+, y-, z$$

$$\gamma_{3j} = \int [R_o(\theta) + R_i(\theta)]V_j(\theta)d\theta \tag{2.43}$$

Substituting Equation (2.42) into (2.40), results in

$$\rho_p A_p \frac{\partial^2 u_{3p}}{\partial t^2} + b_{p3}\frac{\partial u_{3p}}{\partial t} - \frac{A_p}{s_{11}^E}\frac{\partial^2 u_{3p}}{\partial z^2} = 0 \tag{2.44}$$

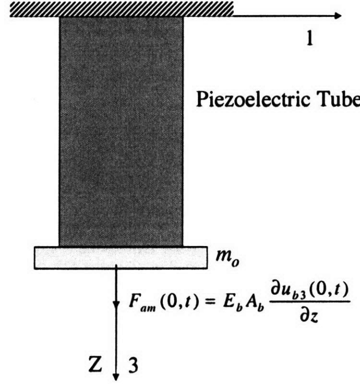

Figure 2-10: Free body diagram of the piezoelectric tube for longitudinal dynamics.

where b_{p3} is the coefficient of viscous damping. The boundary conditions are zero displacement at the fixed end $z = 0$, and a balance of forces at the other end $z = L_p$, which can be expressed as

$$\text{At } z = 0$$

$$u_{3p} = 0 \tag{2.45}$$

$$\text{At } z = L_p$$

$$m_o \frac{\partial^2 u_{3p}(L_p,t)}{\partial t^2} + b_{p3} int_0^{L_p} \frac{\partial u_{3p}(z,t)}{\partial t} dz = -\frac{A_p}{s_{11}^E} \frac{\partial^2 u_{3p}}{\partial z^2} + \frac{d_{31}}{s_{11}^E} \sum_j \gamma_{3j} V_j + \frac{E_b A_b s_{11}^E}{A_p} \frac{\partial u_{3b}(0,t)}{\partial z} \tag{2.46}$$

The solution to Equation (2.44) can be obtained by means of a finite sine Fourier transform which is given by

$$U_{3p}(p,t) = \int_0^{L_p} u_{3p}(z,t) sin(pz) dz \tag{2.47}$$

Taking the Fourier transform of Equation (2.44) results in

$$\rho_p A_p \frac{\partial^2 U_{3p}}{\partial t^2} + b_{p3}\frac{\partial U_{3p}}{\partial t} - \frac{A_p}{s_{11}^E}\frac{\partial^2 U_{3p}}{\partial z^2} = 0 \quad (2.48)$$

where it is assumed that

$$\int_0^{L_p} \frac{\partial^2 u_{3p}}{\partial t^2} sin(pz)dz = \frac{\partial^2}{\partial t^2}\int_0^{L_p} u_{3p}(z,t)sin(pz)dz = \frac{\partial^2 U_{3p}(p,t)}{\partial t^2} \quad (2.49)$$

The Fourier transform of $\frac{\partial^2 u_{3p}}{\partial z^2}$ is given by

$$\begin{aligned}\frac{\partial^2 U_{3p}(p,t)}{\partial z^2} &= \int_0^{L_p} \frac{\partial^2 u_{3p}(z,t)}{\partial z^2} sin(pz)dz \\ &= [\frac{\partial u_{3p}(z,t)}{\partial z} sin(pz) - -pu_{3p}(z,t)cos(pz)]_0^{L_P} - p^2 U_{3p}(p,t) \quad (2.50)\end{aligned}$$

By using the boundary conditions of Equations (2.45) and (2.46), Equation (2.50) reduces to

$$\begin{aligned}\frac{\partial^2 U_{3p}(p,t)}{\partial z^2} &= sin(pL_p)[F_a(t) - \frac{s_{11}^E m_o}{A_p}\frac{\partial^2 u_{3p}(L_p,t)}{\partial t^2} - \frac{s_{11}^E b_{p3}}{A_p}\int_0^{L_p}\frac{\partial u_{3p}(z,t)}{\partial t}dz] \\ &\quad -pu_{3p}(L_p,t)cos(pL_p) - p^2 U_{3p}(p,t) \quad (2.51) \\ F_a(t) &= \frac{d_{31}}{s_{11}^E}\sum_j \gamma_{3j}V_j + \frac{E_b A_b s_{11}^E}{A_p}\frac{\partial u_{3b}(0,t)}{\partial z} \quad (2.52)\end{aligned}$$

Since $\frac{\partial^2 u_{3p}(L_p,t)}{\partial t^2}$, $\frac{\partial u_{3p}(L_p,t)}{\partial t}$, and $u_{3p}(L_p,t)$ are not known, they can be eliminated from Equation (2.51) by setting the sum of their terms to zero which gives

$$p_n L_p tan(p_n L_p) = \frac{\rho_p A_p L_p}{m_o} \quad (2.53)$$

which can be solved for p_n. The natural frequencies ω_{3pn} are given by $\omega_{3pn} = \frac{p_n}{\sqrt{\rho_p s_{11}^E}}$. As a result, Equation (2.51) reduces to

$$\frac{\partial^2 U_{3p}(p_n,t)}{\partial z^2} = F_a(t)sin(p_nL_p) - p_n^2 U_{3p}(p_n,t) \tag{2.54}$$

Hence, Equation (2.48) becomes

$$\rho_p A_p \frac{d^2 U_{3p}(p_n,t)}{dt^2} + b_{p3}\frac{dU_{3p}(p_n,t)}{dt} + \frac{A_p}{s_{11}^E} p_n^2 U_{3p}(p_n,t) = \frac{A_p}{s_{11}^E} sin(p_nL_p)F_a(t) \tag{2.55}$$

with initial conditions

$$U_{3p}(p_n,0) = \int_0^{L_p} u_{3p}(z,0)sin(p_nz)dz$$

$$U_{3p}(p_n,0) = \int_0^{L_p} \frac{\partial u_{3p}(z,0)}{\partial t} sin(p_nz)dz \tag{2.56}$$

$$\tag{2.57}$$

The displacement $u_{3p}(z,t)$ can be found by inverse Fourier transform given by

$$u_{3p}(z,t) = \frac{2}{L_p}\sum_{n=1}^{\infty} U_{3p}(p_n,t)\, sin(p_nz) \tag{2.58}$$

2.3.4 Extension Tube Longitudinal Dynamics

The extension tube is assumed to be rigidly attached to the mass m_o, and its extension u_{3m}, is measured relative to the piezoelectric tube's extension $u_{3p}(L_p)$. Under similar assumptions of those in Section 2.3.1, the equation of motion for u_{3m}, is given by

$$\rho_m A_m \frac{\partial^2 (u_{3m} + u_{3p}(L_p,t))}{\partial t^2} + b_{m3}\frac{\partial u_{3m}}{\partial t} - E_m A_m \frac{\partial^2 u_{3m}}{\partial z_m^2} = 0 \tag{2.59}$$

where b_{m3} is the coefficient of viscous damping. As before, the concentrated load will be accounted for in the modal equations of motion. The boundary conditions then become zero displacement at $z_m = 0$, and a balance of forces at the other end $z_m = L_m$, which can

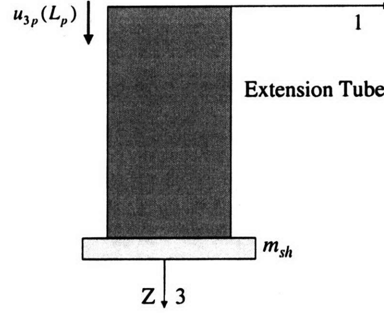

Figure 2-11: Free body diagram of the extension tube for longitudinal dynamics.

be expressed as

At $z_m = 0$

$$u_{3m} = 0$$

At $z_m = L_m$

$$m_{sh}\frac{\partial^2 u_{3m}(L_m,t)}{\partial t^2} + b_{m3}\frac{\partial u_{3m}(L_m,t)}{\partial t} = -A_m E_m \frac{\partial^2 u_{3m}}{\partial z_m^2} \tag{2.60}$$

The solution can be expressed with respect to the mode shape functions ψ_{3mi}, as

$$u_{3m}(z_m,t) = \sum_{i=1}^{\infty} \psi_{3mi}(z_m) T_{3mi}(t) \tag{2.61}$$

$$\psi_{3mi}(z_m) = B_{3mi}\, sin(\frac{\rho_p}{E_m}\omega_{3mi} z_m) \tag{2.62}$$

where B_{3mi} is an arbitrary constant, and the natural frequencies ω_{3mi} can be computed from the solution of

$$\frac{\rho_m}{E_m}\omega_{3mi} L_m tan(\frac{\rho_m}{E_m}\omega_{3mi} L_m) = \frac{\rho_m A_m L_m}{m_{sh}} \tag{2.63}$$

The modal response $T_{3mi}(t)$, is governed by

$$m_{3mi}\ \ddot{T}_{3mi} + b_{3mi}\ \dot{T}_{3mi} + k_{3mi} T_{3mi} = -[\rho_m A_m \int_0^{L_m} \psi_{3mi}(z_m) dz_m + m_{sh}\psi_{3mi}(L_m)]\ \ddot{u}_{3p}\ (L_p,t) \tag{2.64}$$

where

$$
\begin{aligned}
m_{3pi} &= \rho_m A_m \int_0^{L_p} \psi_{3mi}^2(z_m)\, dz_m + m_{sh}\, \psi_{3mi}^2(L_m) \\
b_{3mi} &= b_{m3} \int_0^{L_m} \psi_{3mi}^2(z)\, dz_m \ , \quad k_{3mi} = \omega_{3mi}^2\, m_{3mi}
\end{aligned}
$$

2.3.5 Hysteresis and Nonlinear Displacement Sensitivity

Piezoelectric materials are ferroelectric, hence, they exhibit hysteretic relationship between some of the electric variables (electric field and electric displacement) and the mechanical variables (mechanical strain and force). Hysteresis in piezoelectric materials [31, 32, 33], is generally attributed to molecular friction at sites of material imperfections as a result of domain walls motion. In the absence of an applied electric field, domain walls form at pinning sites to minimize associated potential energy. When a small electric field is applied, domain walls motion is limited and reversible, hence hysteresis in not observed. At higher magnitudes of electric field, the local energy barriers associated with the pinning sites are overcome and domain walls move an extended distance. The motion of domain walls across pinning sites provide an irreversible mechanism that contributes to the observed hysteresis. The experimental observations of absence and existance of hysteresis at low and high electric fields, respectively, is demonstrated in Figure 2-12. The figure shows experimental voltage to mechanical displacement response of a PZT-5H piezoelectric tube actuator for a sinusoidal input at 300Hz and two voltage amplitudes. It is worth mentioning that the first mechanical resonance of this particular actuator is at $9.7\,kHz$. Hence, the experiment is considered quasistatic.

In practice, the electric field applied to a piezoelectric actuator is limited to avoid saturation and degradation in the actuator performance. Therefore, typical hysteresis loops can be characterized by their average slope, loop center point, and the loop width. These characteristics strongly depend on the piezoelectric compound. In a quasistatic hysteresis experiment, the frequency of the periodic input voltage signal should be much lower than the first mechanical resonance. In addition, it should be chosen to be fast enough such

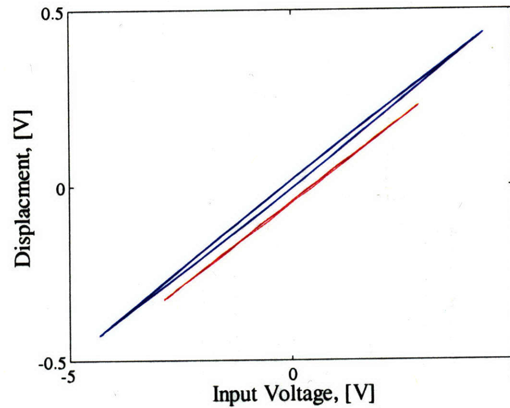

Figure 2-12: Experiments using a sinusoidal input voltage at 300 Hz with two different amplitudes, smaller amplitude in red.

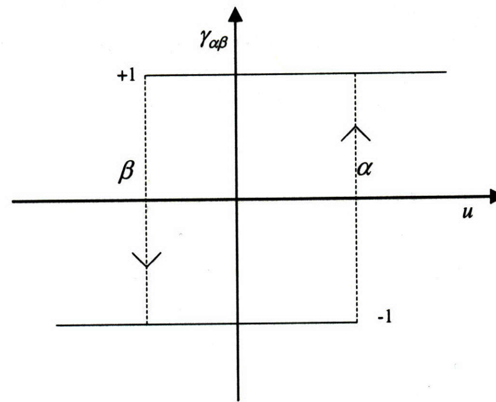

Figure 2-13: Relay hysteresis of Preisach model.

that creep response is not observed. Under these conditions, the width of the measured hysteresis loop will be independent of the input frequency, i.e. rate-independent. The rate independance nature of piezoelectric hysteresis has been expeiemntally verified by several authors [10, 29, 30].

Hysteresis has been extensively studied in the literature. As a result, there are various models of varying complexity that may be used to model hysteresis. In what follows, several rate-independent models suitable for piezoelectric material hysteresis will be briefly discussed. These models can be generally classified as of two types; superposition of a basic hysteresis operator, or integral hysteresis operator. The latter can be written as

an ordinary differential equation (ODE). The former type of models are based on a basic hysteresis element (e.g. relay). A hysteresis loop can be reproduced by using as many elements as needed to achieve a good fit to experimental data. Examples include Preisach [19, 20], Krasnosel'skii and Pokrovskii [21], and the Generalized Maxwell Slip model [22]. Preisach model is the most common model in this category and will be discussed further. The model consists of a weighted combination of elementary relay elements, Figure 2-13, describing the hysteretic relation between an input x and an output F. Mathematically the model is given by

$$F = f(t) = \int\int_{(\alpha,\beta)\in S} \mu(\alpha\,,\,\beta)\,\gamma_{\alpha,\beta}(x(t))\,d\beta\,d\alpha \tag{2.65}$$

where $\mu(\alpha, \beta) > 0$ is a weighing function comprised of two parts capturing both non-hysteretic and hysteretic behavior, and $S = \{(\alpha, \beta) : x_{min} \leq \beta \leq \alpha, x_{min} \leq \alpha \leq x_{max}\}$. In order to use the model for reproducing hysteresis data, $\mu(\alpha, \beta)$ needs to be identified. There are several identification procedures available in the literature, such as that in [29]. However, real-time implementation of the Preisach model is complicated by the need to fit a two-dimensional surface to the experimental data in order to evaluate $\mu(\alpha, \beta)$. As a result, a large number of model parameters is needed to achieve a good fit. In addition, the model output depends on the extrema of the input. Accordingly, the extrema for each relay need to be updated in real-time during each sampling period. This requires that for each relay a search for both extrema values (minimum and maximum) be performed based on the input history. Hence, real-time implementation of Preisach model is cumbersome and slow, and is rarely used in practice. Other models in this category share similar implementation difficulties.

On the other hand, ODE-based models typically consist of a single nonlinear ODE. Examples include Bouc-Wen [23, 24], Dahl [25], Chua-Stromsmoe [26, 27], and Coleman-Hodgdon [28]. These equations describe the hysteretic relation between an input x and an output F. Most ODE models have the following form,

$$\dot{F} \;=\; \frac{dF}{dx}\frac{dx}{dt} = f(x, F, sgn(\dot{x}))\,\dot{x} \tag{2.66}$$

Note that $f(x, F, sgn(\dot{x}))$ does not depend explicitly on time or $\dot{x}$ but rather on the sign of $\dot{x}$. This captures the rate-independence nature of energy loss in the hysteresis loop. The dependence on x allows for capturing energy storage in the model. As an example, consider Dahl's model which has the following from

$$\frac{dF}{dx} = \sigma|1 - \frac{F}{F_c}sgn(\dot{x})|^i\, sgn(1 - \frac{F}{F_c}sgn(\dot{x})) \tag{2.67}$$

where sgn is the sign function, and F_c and σ are constants. For $\frac{|F|}{F_c} \ll 1$, $F \approx \sigma x$. In a mechanical system this expression represents a constitutive law of a spring, with F being a force and x a displacement. More generally, an element that stores potential energy. As $|x| \to \infty$, $\frac{dF}{dx} \to 0$ and $|F| \to F_c$. Hence, at large values of x, the model behave like a Coulomb friction, providing a mechanism for energy dissipation that is rate-independent.

An advantage for ODE-based models is that they could be more tractable for control design compared to operator-based models. In addition, the functions used in the ODE can be chosen to shape the hysteresis loop as desired provided that some conditions are satisfied. However, there could be a trade-off between complexity of the functions and implementation. Complex nonlinear functions may give a good match with experimental data. However, model parameter identification may become more difficult. Moreover, simple functions with few parameters may not be capable of reproducing experimental data particularly well. In addition, sensitivity due to parameter variation is expected to be larger than operator-based models with a large number of parameters.

In piezoelectric materials energy transduction occurs between the electrical and mechanical domains. As discussed earlier, impediment of domain wall motion contributes to hysteresis. However, it is not clear whether there are other mechanisms in the mechanical domain that contribute to the observed hysteresis. Answering this question allows including

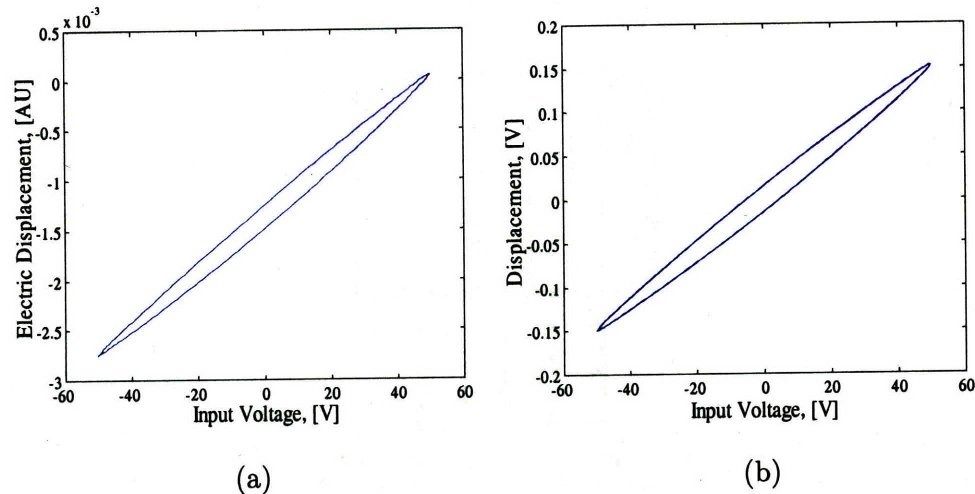

Figure 2-14: Piezoelectric scanner response to a sinusoidal input voltage at $20\,Hz$ (a) electrical displacement (arbitrary units AU) vs. input voltage, (b) mechanical displacement vs. input voltage.

a physically consistent hysteresis model in the overall model of a piezoelectric actuator. As before, it has been suggested that hysteresis occurs in the electrical domain between the applied electric field and electric displacement or charge. This is supported by experimental observations as in Figure 2-14 (a). Hysteresis is also observed, Figure 2-14 (b), between electric field and mechanical strain or displacement. In addition, hysteresis is noticed between force and mechanical strain [30], when actuator electrodes are shorted and charge is allowed to flow. However, no hysteresis is observed when electrodes are open and no charge flows within the material. More so, charge vs. mechanical strain as in Figure 2-15, shows no hysteresis. Accordingly, hysteresis is believed to lie mainly in the electrical domain.

To include hysteresis in the piezoelectric tube model, its effect will be lumped into a single element as seen in Figure 2-16. Due to hysteresis, the applied electric field E, is balanced by a potential drop E_h, due to the combined capacitance and resistance of the hysteretic element, in addition to a drop E_p, across the hysteresis-free capacitance of the piezoelectric material. Hence, $E = E_h + E_p$. The models of sections 2.3.1 and 2.3.3, were derived assuming that $E_p = E$ in the piezoelectric constitutive relation Equation (2.14).

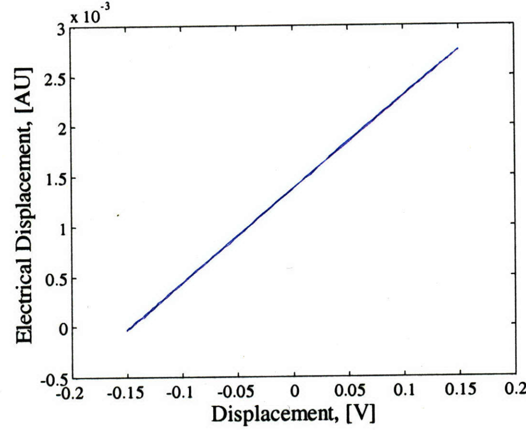

Figure 2-15: Piezoelectric scanner response to a sinusoidal input voltage at 20 Hz: electrical displacement (arbitrary units AU) vs. mechanical displacement.

The new constitutive relation is given as

$$\begin{pmatrix} \epsilon_z \\ D_r \end{pmatrix} = \begin{pmatrix} s_{11}^E & d_{31} \\ d_{31} & \epsilon_3^\sigma \end{pmatrix} \begin{pmatrix} \sigma_z \\ E_{pr} \end{pmatrix} . \tag{2.68}$$

In addition, the electric charge in the scanner q_p, is given by

$$q_p = \int D_r \, dA_p \tag{2.69}$$

$$E_r = E_{hr} + E_{pr} \tag{2.70}$$

As a result, Equations 2.26 and 2.52, know become

$$M \ddot{T}_{1p} + C \dot{T}_{1p} + K T_{1p} = Q_{1p} \begin{bmatrix} E_b I_b \frac{\partial^3 u_{1b}(0,t)}{\partial z^3} \\ E_b I_b \frac{\partial^2 u_{1b}(0,t)}{\partial z^2} \\ \frac{d_{31}}{s_{11}^E} \sum_j \gamma_j (V_j - k_{1jh} V_h) \end{bmatrix}$$

$$F_a(t) = \frac{d_{31}}{s_{11}^E} \sum_j \gamma_{3j} (V_j - k_{3jh} V_h) + \frac{E_b A_b s_{11}^E}{A_p} \frac{\partial u_{3b}(0,t)}{\partial z} \tag{2.71}$$

where k_{1jh} and k_{3jh} are constants introduced to account for the fact that not the whole piezoelectric material necessarily contributes to hysteretic behavior. A hysteresis model is then expressed between the charge and the potential across the hysteresis capacitance V_h. Both types of hysteresis models could be used by replacing x with charge q_p, and F with

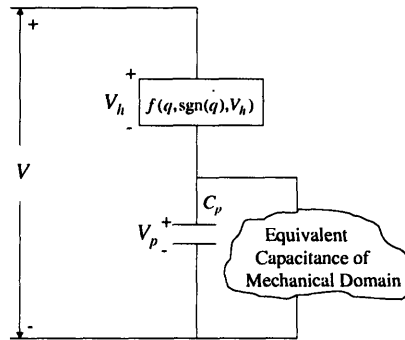

Figure 2-16: Schematic representation of piezoelectric scanner with hysteresis.

V_h. For the ODE models, this results in

$$\dot{V_h} = f(q_p, V_h, sgn(\dot{q}_p))\, \dot{q}_p \tag{2.72}$$

The anhysteretic voltage to displacement curve may be used to model the nonlinear voltage to displacement sensitivity of the piezoelectric scanner.

2.3.6 Creep

The response of a piezoelectric actuator to a rapid change in input voltage, Figure 2-17, consists of two main parts. The initial part of the response occurs over a time scale dictated by the mechanical resonance of the actuator, typically few millisecond. This is followed by a slow creeping response occuring over tens to hundreds of seconds and could amount to more than 20 % of the total response. The rate and amount of creep, strongly depend on the piezoelectric compound. As discussed in Section 2.3.5, pinning sites impede on the motion of domain walls. When an electric field is applied to the material, the domain walls will eventually align in a way to conform with the applied electric field. The initial fast response would be due to domain walls experiencing little resistance and their response would be limited by the maximum mechanical strain rate of the material. Other domain walls, on the other hand, would experience much more resistance to their motion. The effective capacitance and path resistance of these domain walls, will dictate the amount of motion

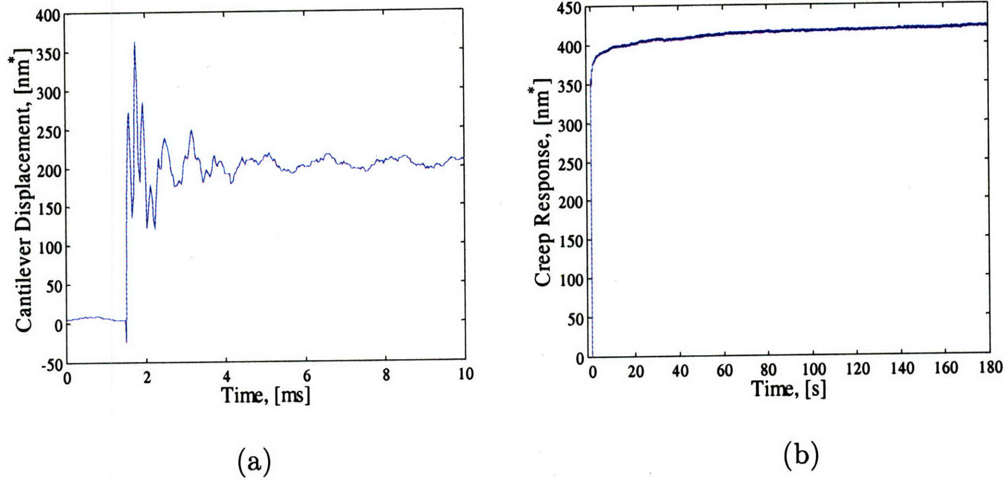

Figure 2-17: Two creep experiments: (a) initial fast response, (b) slow creep response.

and time scale over which this motion occurs. This could amount to the creep response. Two models for creep will be presented, namely, a logarithmic model and a finite-dimension linear time-invariant (LTI), model.

When creep response is plotted verses time on a logarithmic scale as in Figure 2-18, the response appears to be linear. Therefore, a common equation [90, 94], to model creep is

$$z(t) = z_o[1 + \gamma\, log_{10}(\frac{t}{t_o})] \tag{2.73}$$

where $z(t)$ is the actuator displacement, z_o is the nominal fast displacement to the applied voltage, γ is a constant controlling the rate of creep, and t_o is the time after which creep response is considered to start, i.e. after the fast dynamics response has occured.

The aforementioned discussion on the origin of creep, may suggest that a model composed of capacitive and resistive elements may be appropriate. Furthermore, experimental frequency response of piezoelectric actuators shown in Figure 2-19 (a), displays very little variation in phase at low frequency between input voltage and displacement, Figure 2-19 (b). Moreover, as seen in Figure 2-19 (b), a slight decrease in gain is observed with increased frequency; 4.5% from $10\,Hz$ to $300\,Hz$. Therefore, a transfer function model between the input voltage and actuator displacement would have a relative degree zero at frequencies

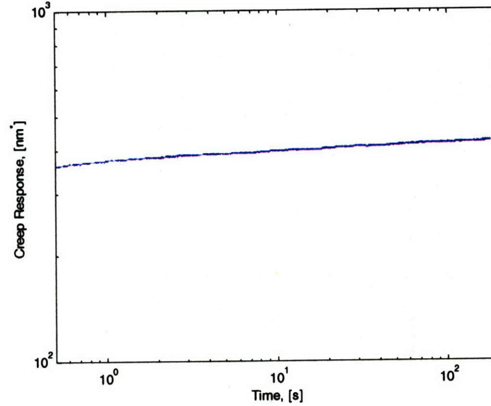

Figure 2-18: Experimental creep response plotted on logarithmic scale.

much lower than the actuator's first resonance frequency. The relative degree is defined as the number of poles minus the number of zeros. It is possible therefore, to simulate creep behavior using a suitable LTI model composed of capacitive and resistive elements. A schematic representation of one choice of such model is shown in Figure 2-20, and its mathematical representation is given as

$$\frac{z_p}{V_z} = \frac{b_{m+n-2}s^{m+n-2} + b_{m+n-3}s^{m+n-3} + \ldots + b_0}{s^{m+n} + a_{m+n-1}s^{m+n-1} + \ldots + a_0} \tag{2.74}$$

$$= G_f(s)\, G_{creep}(s) \tag{2.75}$$

where G_f is the transfer function containing the fast dynamics and retains n poles and $n-2$ zeros as suggested by the models presented in Sections 2.3.1 to 2.3.4. G_{creep} is the transfer function modeling the creep which has a zero relative degree and contains m poles.

Both creep models, however, assume that the ratio between the amount of creep and the fast scanner displacement is independent of input amplitude and rate. Both assumption were experimentally tested and results are given in Chapter 4.

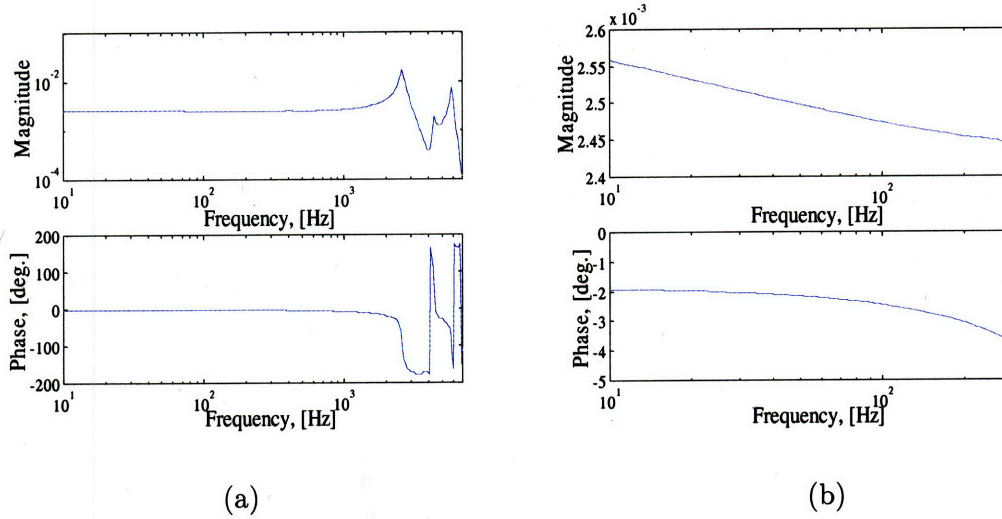

Figure 2-19: Experimental frequency response between input voltage and displacement of a PZT-5H actuator (a) Full frequency range, (b) zoom on 10 to 300 Hz range.

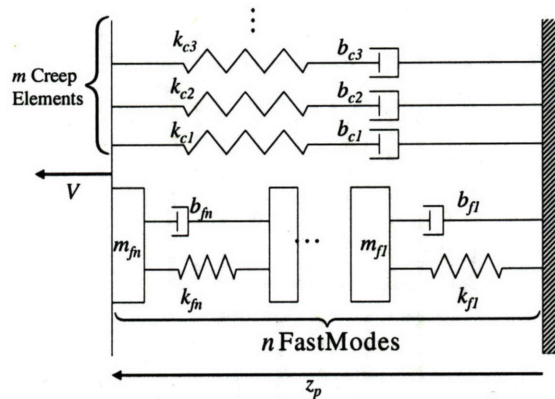

Figure 2-20: Schematic representation of a model for both fast and creep dynamics.

2.4 Cantilever Dynamics

2.4.1 Flexural Dynamics

This dynamic model for cantilever deflection is based on elementary bending theory, hence neglects effects of shear deformation and rotatory inertia. The cantilever is assumed to have a constant rectangular cross sectional area A_c, moment of inertia I_c, mass density ρ_c, Young's modulus of elasticity E_c, Poisson's ratio ν_c, and a probe of length l_t. The cantilever deflection $u_{3c}(x,t)$, is measured relative to its base motion $u_{3sh}(t) = u_{3p}(L_p,t) + u_{3m}(L_m,t)$. Forces acting on the cantilever include a distributed force $p(x,t)$, and concentrated force and moment $F(t)$ and $M(t)$, respectively. The concentrated loads act on the probe at a distance x_s measured from the cantilever's base. $F(t)$ is due to the vertical probe-sample interactions, while $M(t)$ is a moment resulting potentially from probe-sample lateral friction force. Linear damping originating from three possible sources is considered, namely, damping from air $F_a(x,t)$, from contact of probe with the sample surface $F_c(t)$, or internal material damping $F_m(x,t)$. Material damping is assumed to be proportional to strain rate. Both F_a and F_c depend on the absolute velocity of the cantilever, while F_m depends on the relative deflection of the cantilever with respect to its base. Hence, the form for damping forces is as follows

$$\begin{aligned} F_a(x,t) &= b_a \frac{\partial u_{3c}(x,t)}{\partial t}, \quad F_c(t) = b_c \frac{\partial u_{3c}(x_s,t)}{\partial t} \\ F_m(x,t) &= b_m \frac{\partial^2}{\partial x^2}\left(I_c \frac{\partial^3 u_{3c}(x,t)}{\partial x^2 \partial t}\right) \end{aligned} \tag{2.76}$$

While in contact, Air damping is negligible. However, it has been included to account for Air damping during loss of contact and for non-contact and intermittent contact modes. The ratio between the probe to the cantilever mass is typically about 0.1%, and therefore, the probe mass will be neglected. The boundary conditions are therefore, taken as zero deflection and slope relative to the base at the fixed end, and zero moment and shear force at the free-end. The boundary conditions are represented as

$$\text{At } x = 0$$

$$\begin{aligned} u_{3c} &= 0 \\ \frac{\partial u_{3c}(0,t)}{\partial x} &= 0 \end{aligned}$$

$$\text{At } x = L_c$$

$$\begin{aligned} E_c I_c \frac{\partial^3 u_{3c}}{\partial x^3} &= 0 \\ E_c I_c \frac{\partial^2 u_{3c}}{\partial x^2} &= 0 \end{aligned} \tag{2.77}$$

The mode shape functions are given by

$$\begin{aligned} \phi_{3ci}(x) &= (cos\lambda_{3ci}x + cosh\lambda_{3ci}x) + \\ &\quad \frac{(cos\lambda_{3ci}L_c + cosh\lambda_{3ci}L_c)}{(sin\lambda_{3ci}L_c + sinh\lambda_{3ci}L_c)}(sinh\lambda_{3ci}x - sin\lambda_{3ci}x) \qquad (2.78) \\ 0 &= cos\lambda_{3ci}L_c cosh\lambda_{3ci}L_c + 1 \qquad (2.79) \end{aligned}$$

The natural frequencies are given by

$$\omega_{3ci} = (\lambda_{3ci}L_c)^2 \sqrt{\frac{E_c I_c}{(1-\nu_c^2)\rho_c A_c L_c^4}} \tag{2.80}$$

where $\lambda_{3ci}L_c$ are roots of Equation (2.79). The equation of motion in modal coordinates q_{3ci}, is given as

$$\begin{aligned} m_{3ci}\ddot{q}_{3ci} + b_{3ci}\dot{q}_{3ci} + k_{3ci}q_{3ci} &= \int_0^{L_c} \phi_{3ci}(x)p(x,t)dx + \phi_{3ci}(x_s)F(t) \\ &+ \phi'_{3ci}(x_s)M(t) - \rho_c A_c \int_0^{L_c} \phi_{3ci}(x)dx \; \ddot{u}_{3sh}(t) \\ &- [b_a \int_0^{L_c} \phi_{3ci}(x)dx + b_c\phi_{3ci}(x_s)] \; \dot{u}_{3sh}(t) \\ &- \rho_c A_c \int_0^{L_c} \phi_{3ci}(x)x dx \; \ddot{\theta}_{ysh} \\ &- [b_a \int_0^{L_c} \phi_{3ci}(x)x dx + b_c\phi_{3ci}(x_s)x_s] \; \dot{\theta}_{ysh} \end{aligned} \tag{2.81}$$

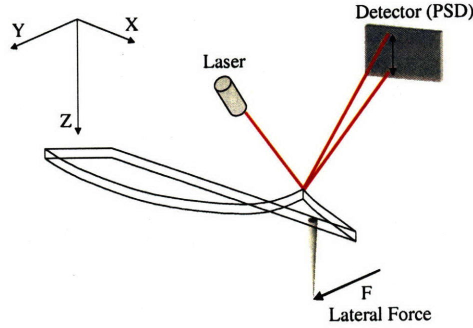

Figure 2-21: Coupling between cantilever twist and PSD signal due to cantilever bending.

Moreover, the modal mass m_{3ci}, modal damping b_{3ci}, and modal stiffness k_{3ci}, are given by

$$\begin{aligned} m_{3ci} &= \rho_c A_c \int_0^{L_c} \phi_{3ci}^2(x)dx, \;\; k_{3ci} = \omega_{3ci}^2 m_{3ci} \\ b_{3ci} &= b_a \int_0^{L_c} \phi_{3ci}^2(x)dx + b_c \phi_{3ci}^2(x_s) + b_s I_c \int_0^{L_c} \phi_{3ci}^{(iv)} \phi_{3ci}(x)dx \end{aligned}$$

2.4.2 Cantilever Twist

When the laser spot is aligned onto the back of the cantilever, inevitably there will be an offset form the axis of the cantilever (X-axis in Figure 2-21). In addition, the laser spot size is finite. As a result, twist in the cantilever θ_{xc}, results in a vertical change in the position of the reflected laser beam falling on the detector. Cantilever twist can be due to probe-sample friction force, changes in the sample topography, or an impact between the probe wall and a high aspect ratio feature on the sample. The dynamics of twist will not be considered as it is typically much faster than the flexural dynamics. However, a quasi-static relation coupling twist angle θ_{xc} with sensor output y_{PSD} will be assumed as

$$y_{PSD} = k_{xc}\theta_{xc} \tag{2.82}$$

2.5 Noise and Disturbances

Thermal noise or Brownian motion contributes to a fundamental source of noise in AFM. At thermal equilibrium, the mean value of the cantilever potential energy has to equal $\frac{1}{2}k_BT$, where $k_B = 1.38 \times 10^{-23}\, J/K$ is Boltzmann's constant, and T is the absolute temperature in Kelvin. By considering the first mode of the cantilever, the slope at the cantilever's free-end will oscillate with a RMS value, $z_c'^{rms} = \frac{3}{2L_c} z_c^{rms} = \frac{3}{2L_c}\sqrt{\frac{k_BT}{k_c}}$, where k_c is the stiffness of the cantilever's first mode. This expression is valid for a free standing cantilever. If the cantilever is in contact with a sample, the expression has to be modified by including the sample effective stiffness in k_c. Another source of disturbance is the laser back-action. It is due to incidence of photon flux from the optical sensor on the cantilever. Both thermal and back-action noises will be effectively modeled as zero-mean white noise force disturbances with a combined constant intensity $\chi\,\delta(t-\tau)$, where $\delta(t-\tau)$ is the Dirac delta function. Further, mechanical vibrations transmitted through the mechanical structure of the AFM may result in cantilever oscillations, and relative motion between the probe and the sample. Consequently, the noise floor of the AFM would increase.

Feedback measurement noise arising from the optical sensor can be due to shot noise, a fundamental noise for these sensors, in addition to noise from sensor electronics. Shot noise can also be modeled as white noise.

2.6 Overall AFM Model

The models developed in Sections 2.2 to 2.4.2, constitute a detailed overall model for AFM dynamics. In addition, the complexity and order of the model can chosen based on the objectives of using the model. The model can be used to analyze and simulate the dynamic response between the five input voltages and any combination of desired outputs. Particularly important outputs include the displacements of the sample holder $u_{1sh}, u_{2sh}, u_{3sh}$ in the X, Y, and Z directions and the rotations (i.e. slopes), of the sample holder about X and Y axes, namely θ_{xsh} and θ_{ysh}. And most importantly, the PDS signal. The equations

for the aforementioned outputs are

$$
\begin{aligned}
x_{sh} &= cos(\theta_\delta)[u_{1p}(L_p,t) + u_{1m}(L_m,t)] - sin(\theta_\delta)[u_{2p}(L_p,t) + u_{2m}(L_m,t)] && (2.83) \\
y_{sh} &= sin(\theta_\delta)[u_{1p}(L_p,t) + u_{1m}(L_m,t)] + cos(\theta_\delta)[u_{2p}(L_p,t) + u_{2m}(L_m,t)] && (2.84) \\
z_{sh} &= u_{3p}(L_p,t) + u_{3m}(L_m,t) && (2.85) \\
\theta_{ysh} &= cos(\theta_\delta)[u'_{1p}(L_p,t) + u'_{1m}(L_m,t)] - sin(\theta_\delta)[u'_{2p}(L_p,t) + u'_{2m}(L_m,t)] && (2.86) \\
\theta_{xsh} &= sin(\theta_\delta)[u'_{1p}(L_p,t) + u'_{1m}(L_m,t)] + cos(\theta_\delta)[u'_{2p}(L_p,t) + u'_{2m}(L_m,t)] && (2.87) \\
y_{PSD} &= \theta_{ysh} + k_{xsh}\,\theta_{xsh} + k_{xc}\,\theta_{xc} - z'_{3c}(x_L,t) && (2.88)
\end{aligned}
$$

where k_{xsh} is a coupling parameter between the PSD signal and the bending of the scanner about the X-axis, and x_s is the distance from the cantilever's base to the laser spot on the back of the cantilever.

2.7 Summary

In this chapter, a detailed dynamic model for the AFM was presented. It includes a new model for the piezoelectric scanner coupled longitudinal and lateral dynamics, creep, and hysteresis. Models for probe-sample interactions and cantilever dynamics were also presented.

Chapter 3

Scanner Calibration

3.1 Introduction

The accuracy of AFM data ultimately depends on the calibration of the scanner. Piezoelectric materials exhibit nonlinear quasistatic voltage to displacement response. Typically, a trade-off between nonlinearity and displacement range exist based on the piezoelectric compound. A scanner made of PZT-5H will have a displacement sensitivity twice of that of a similar scanner made from PZT-4. However, nonlinearity of 3 to 5 % is expected for the PZT-4 scanner compared to 20 to 25 % if PZT-5H is utilized. Scanners used in AFM have typical displacement ranges of 10 to 100 μm laterally, and 4 to 10 μm vertically. Calibration of the scanner is usually performed by imaging a standard sample with a known characteristic dimension. The voltage to displacement sensitivity is then computed from the applied voltage and the known dimension(s) of the standard. A linear sensitivity is assumed for vertical calibration, while a quadratic or a cubic polynomial is used for lateral calibration. Structures with pitch of 200 nm to 10 μm are commercially available for lateral calibration. For a large scan size, an adequate number of data points can be collected from the image and used for lateral calibration. On the other hand, standards for vertical calibration are available with height between 9 nm and 1.6 μm. However, utilizing images for calibration could be problematic, especially for vertical calibration. As have been shown, image quality depends strongly on scan and controller parameters. Due to scanner nonlinear displacement, calibration may be affected by the bias voltage applied to the scanner to maintain

probe-sample contact at the desired set-point during scanning. In addition, computed sensitivity will depend on scan speed due to creep. Images obtained at a slow scan speed would yield larger sensitivity compared to images performed at faster speeds. Moreover, standards with a small height compared to the scanner range, are commonly used for calibration to reduce the effect of hysteresis. Consequently, calibration would only be accurate for a small fraction of the total scanner range (typically $\sim 3\%$). Imaging samples with features taller than the standard used for calibration will be corrupted with both hysteresis and nonlinearity due to the scanner's displacement. Consequently, there is a strong need to develop a method to allow calibration of the scanner's full range vertical displacement, in addition to hysteresis identification.

3.2 New Method for Scanner Height Calibration

Typically, accelerometers, consist of a flexible structure of some effective mass and stiffness. When the structure is subjected to an acceleration, its measured response is related to the acceleration signal. A schematic representation of an accelerometer is shown in Figure 3-1. In this simple representation and under sinusoidal acceleration $\ddot{z}_p$, the measured response z_c of the proof mass m_c is governed by

$$\ddot{z}_c + \omega_c^2 \, z_c = - \, \ddot{z}_p \,, \quad \omega_c = \sqrt{\frac{k_c}{m_c}} \tag{3.1}$$

$$\text{For } z_p = A \, sin(\omega \, t) \,, \ \text{ and } \ \omega < \omega_c$$

$$|z_c| = A \left(\frac{\omega}{\omega_c} \right)^2 \tag{3.2}$$

Therefore, by measuring the response of z_c, the displacement amplitude of z_p can be determined. Figure 3-2, shows a schematic of the AFM scan unit, including the scanner, the cantilever, and the optical sensor. The similarity between the scan unit and an accelerometer can be seen from the figure. The source of acceleration is z_p, and the cantilever is the flexible structure. Accordingly, it may be possible to apply a sinusoidal input voltage V_z and relate the measured cantilever response to z_p. By doing so, a calibration map could be obtained for the entire displacement range. However, the PSD signal y_{PSD}, measures the

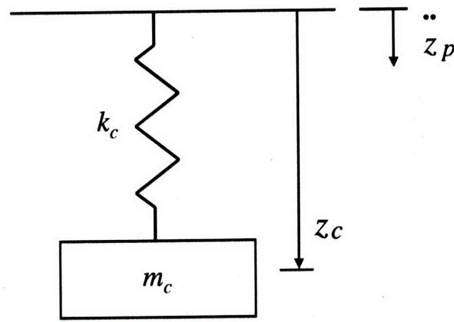

Figure 3-1: Schematic representation of an accelerometer.

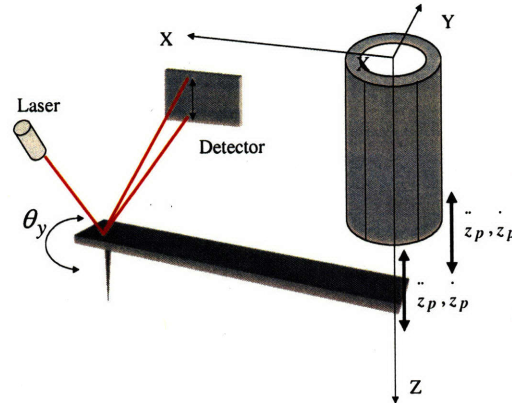

Figure 3-2: Schematic of the AFM scanner, cantilever, and optical sensor.

absolute angle of the cantilever in space, which is given by

$$y_{PSD} = \theta_{ysh} - z_c'(x_L, t) \tag{3.3}$$

Due to the coupling between V_z and θ_{ysh}, as shown in Chapter 2, z_p can not be practically inferred from y_{PSD}.

As a remedy for this problem, the cantilever deflection relative to its base could be measured and used for calibration. In the past, cantilevers with piezoresistive elements [36], were utilized in AFM for imaging as an alternative to using the optical sensor. However, their noise performance in Air was found far inferior to that of the optical sensor. In addi-

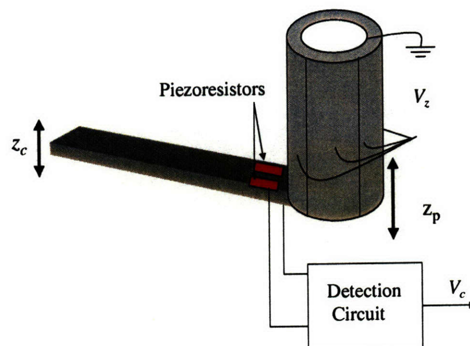

Figure 3-3: Schematic of the piezoelectric scanner with a piezoresistive cantilever.

tion, piezoresistive cantilevers suffered from drift and poor long-term stability. Therefore, their use did not gain wide spread and is mainly limited to AFM operation in ultra-high vacuum.

The new proposed calibration method is based on using a piezoresistive cantilever as an accelerometer, Figure 3-3. While in Air and far away from any sample surface, a sinusoidal voltage V_z is applied to the scanner, and the response of the piezoresistive cantilever is detected. The measured response can easily be related to the displacement of the scanner. These cantilevers can be fabricated to fit standard AFM cantilever holders. Therefore, eliminating the need for specialized fixtures and allowing them to be used for almost all commercial AFMs with a cantilever-on-scanner design. In addition, biasing the piezoresistors can be accomplished easily. Cantilever holders are attached to a piezoelectric crystal that is used to oscillate the cantilever for non-contact and intermittent modes. The wiring used for driving the crystal may be used for biasing the piezoresistors. A simple Whetstone bridge circuit can be used for detecting the resistance change in the piezoresistors. Further, for each data point to be used for calibration, only few oscillation cycles at $10s$ to $100s\,Hz$ need to be collected. Hence, drift and long term stability will not be a concern. What remains to be shown, though, is that the cantilever's noise performance in Air is adequate for the calibration experiment.

Design equations for piezoresistive cantilevers are available in [38]. A new fabrication technique in [37], permitted fabrication of ultra-thin piezoresistive AFM cantilever with thickness of 87 to 90 nm. The objective of this work was to improve force detection limit of piezoresistive AFMs; detailed analysis and design equations were therefore given. Noise performance predictions based on these design equations were found to be in good agreement with the measured performance of the fabricated cantilevers. Therefore, these design equations will be used below to demonstrate the feasibility of the proposed calibration technique. Sources of noise in piezoresistive cantilevers are mainly Johnson noise, $1/f$ noise, and thermomechanical noise. Johnson noise is due to thermal energy of carriers in a resistor R. It is a white noise with a spectral density function S_J given by

$$S_J = 4k_BTR \tag{3.4}$$

where k_B is Boltzmann's constant, and T is temperature in Kelvin of the resistor. In a bandwidth of f_{max} to f_{min}, the mean-square noise is

$$V_J^2 = \frac{16k_B\,T\,L_{leg}}{w\,t_d\,\mu\,q\,p}(f_{max} - fmin) \tag{3.5}$$

where L_{leg} is the length of piezoresistive cantilever leg, w is the total cantilever width, t_d is doped thickness, μ mobility, q electron charge, and p doping density. On the other hand, $1/f$ noise has a spectral density S_f, given by

$$S_f = \frac{\alpha V_B^2}{N f} \tag{3.6}$$

where V_B is the voltage bias across the resistor, N number of carriers, and α a nondimensional parameter that depends on annealing for an implanted resistor. In a bandwidth of f_{max} to f_{min}, the mean-square noise is

$$V_f^2 = \frac{\alpha V_B^2}{N} ln(\frac{f_{max}}{f_{min}}) \tag{3.7}$$

N is proportional to the cantilever volume for a constant doping concentration. It is assumed that $N = pL_{leg}t_d w$. Thermomechanical noise is the mechanical equivalent of Johnson noise. Its spectral density S_{tm}, for a single mode approximation is given by

$$S_{tm} = \frac{4k_B T}{k_c \omega_c Q_c} \tag{3.8}$$

where k_c is the cantilever stiffness, and Q_c is the quality factor. The corresponding RMS displacement noise z_{ctm}, is

$$z_{ctm} = \sqrt{\frac{4k_B T}{k_c \omega_c Q}}, \ \omega \ll \omega_c \tag{3.9}$$

$$z_{ctm} = \sqrt{\frac{4k_B T Q}{k_c \omega_c}}, \ \omega = \omega_c \tag{3.10}$$

If the piezoresistor makes up one corner of a Wheatstone bridge, the output voltage V_o can be found from

$$V_o = \frac{V_B \Delta R}{4R} \tag{3.11}$$

$$\frac{\Delta R}{R} = \frac{3\pi_L E t(L_c - L_{leg}/2)}{2L_c^3} z_c \tag{3.12}$$

where π_L is the piezoresistive coefficient, E is modulus of elasticity, t is total thickness, w is cantilever width, and L_c is cantilever length. In practice, thermomechanical noise is seldom the dominant noise source. Exception to this are cantilevers with high Q_c that are operated at their resonance. Under this condition, the total root-mean-squared (RMS), displacement noise $z_{c_{min}}$ is found as

$$z_{c_{min}} = \frac{\sqrt{\frac{\alpha V_B^2}{L_{leg} t_d w p} ln(\frac{f_{max}}{f_{min}}) + \frac{16 k_B T L_{leg}}{w t_{d,} \mu q p}(f_{max} - f_{min})}}{\frac{3 V_B \pi_L E t (L_c - L_{leg})}{16 L_c^3}} \tag{3.13}$$

Commercial piezoresistive cantilevers are generally optimized either for imaging or force detection. As a result, they are generally not suitable for use in this calibration procedure. In order to demonstrate the feasibility of using a piezoresistive cantilever for the proposed calibration method, a cantilever has been designed to have adequate signal-to-noise ratio (SNR), at $200\,Hz$. It is assumed that the first mechanical resonance of the AFM scan unit will be a at least a factor of 2 to 3 higher than the driving frequency to ensure a quasistatic response of the scanner. The resulting cantilever has a length $Lc = 600\,\mu m$, width $w_c = 50\,\mu m$, thickness $t_c = 0.2\,\mu m$, and resonance frequency $\omega_c = 785\,Hz$. Using the model of Section 2.4, the sensitivity of the cantilever displacement to scanner displacement is found to be $\frac{z_c}{z_p} = 0.1$ at $200\,Hz$. For a 100 to $400\,Hz$ bandwidth, Equation (3.13), gives $z_{c_{min}} = 2.9\,nm\ RMS$. The SNR is then SNR $= \frac{0.1\,z_p(nm)}{2.9}$. For example, if $zp = 150\,nm$ (3 % of typical scanner range), the expected SNR is 5.2. Consequently, the proposed calibration method could be used to calibrate the scanner's vertical displacement from a few percent of its range up to its full range. In addition, the maximum strain in this cantilever would remain small; less than 2×10^{-3} for scanner range of $z_p = 10\mu m$ corresponding to a maximum acceleration of $1.6g$, where g is the acceleration of gravity. Linearity better than 0.1% for piezoresistive-based accelerometers has been commercially demonstrated. Moreover, the SNR can be further improved. As seen from Equation (3.2), z_c and hence SNR depend quadratically on the ratio of the frequency ω, of the acceleration source z_p, to the cantilever's resonance frequency ω_c. Hence, increasing this ratio would increase the SNR. Increasing ω is limited by the first resonance frequency of the scanner to ensure a quasistatic measurement. Lowering ω_c can be easily done by adding a so-called proof mass at the end of the cantilever as evident from Equation (3.1). In addition, by setting $\omega = \omega_c$, hence operating the cantilever at resonance, the SNR can be further improved by a factor of Q_c; experimental data show that typically $Q_c \geq 5$. Consequently, operating at resonance can permit using the proposed method to calibrate the scanner's displacement from few nanometers up to the full range of the scanner.

In order to use the cantilever for calibration, its output sensitivity to acceleration k_{V_oa}, needs to be determined. Once, mounted on the scanner, the piezoresistive cantilever will

experience the acceleration of gravity g. Hence, by merely measuring the cantilever's output with no scanner displacement, its acceleration sensitivity can be obtained. If designed to permit so, the cantilever can be flipped and its output recorded. This allows using two data points for determining the acceleration sensitivity. Since the cantilever displacement or voltage output V_o is linear in z_p, Equation (3.2), the scanner calibration can be obtained from

$$z_p(V_z) = \frac{V_o}{k_{V_o a}\omega^2} \tag{3.14}$$

The resulting curve between the input voltage V_z and the scanner vertical displacement z_p can be used to compensate for scanner displacement nonlinearity. The method may also be used to characterize scanner hysteresis over the full scanner range. Another advantage of this method, is that the calibration will not be affected by scanner creep or drift since the dynamic measurements are done at frequencies in the $10s$ to $100s$ of Hz. Furthermore, commercially available piezoresistive cantilevers cost less than \$100 to purchase. In contrast, calibration standards cost about \$200 for a set of three and their height is only a fraction of the total scanner's displacement.

3.3 Error Analysis

As seen in Section 2.3.1, when the scanner is commanded to move vertically by applying a voltage V_z, a slight bending motion also occurs. A first order analysis of errors due to this coupling was performed. As seen in Figure 3-4 (a), offsets of δ_x and δ_y, are assumed between the cantilever base and the centroid of the scanner's cross-section. The actual displacement at the cantilever base is not only due to z_p. As a result of scanner bending, displacements of the order of $\delta_x\theta_y$ and $\delta_y\theta_x$, are introduced. Geometric coupling between bending and extension, as seen in Figure 3-4 (b), is also considered. The resulting change in vertical displacement Δz_b, is given by

$$\Delta z_b = L_p - \sqrt{4R_{curv}^2 \, sin^2(\frac{\theta_y}{2}) - y^2} \quad (3.15)$$

where $$R_{curv}\,\theta_y = L_p\,, \;\; \theta_y = \frac{2y}{L_p} \quad (3.16)$$

$$\Delta z_b = L_p - \sqrt{\frac{4L_p^2}{\theta_y^2}\, sin^2(\frac{\theta_y}{2}) - (\frac{L_p\theta_y}{2})^2} \quad (3.17)$$

A typical scanner with vertical and lateral ranges of 5 and 40 μm, respectively, will be used in this analysis. The maximum angle due to bending $\theta_y \approx 2 \times 10^{-5}\, rad$ was estimated using two methods. First, the angle was estimated from experimental data using an AFM. The displacement sensitivity of the cantilever was estimated by bringing the probe into contact with a hard sample and moving the scanner up and down. Then, the probe was moved far away from the sample and a triangular voltage signal V_z, was applied to the scanner. The output of the detector y_{PSD} was then recorded. The output was converted to an angle based on the cantilever length. In the second method, the scanner model was used to predict scanner bending due to V_z. The result using the model was off by a factor of 30% from the experimental result. The maximum value of both estimates was used. The errors are summarized below assuming a 1 mm offsets in X and Y

$$\delta_x\theta_{ysh} \approx 1mm \times 2 \times 10^{-5} rad \qquad (0.4\,\%\text{ of } 5\,\mu m \text{ range})$$

$$\delta_y\theta_{xsh} \approx 1mm \times 2 \times 10^{-5} rad \qquad (0.4\,\%\text{ of } 5\,\mu m \text{ range})$$

$$L_c\theta_x \approx 500\mu m \times 2 \times 10^{-5} rad \qquad (0.2\,\%\text{ of } 5\,\mu m \text{ range}).$$

$$\Delta z_b \approx 1.5 \times 10^{-5} \qquad (0.3\%\text{ of } 5\,\mu m \text{ range}).$$

Therefore, errors $\approx 1\,\%$ is expected at full range. This is a substantial improvement over possible errors of 20 to 25% due to scanner nonlinearity.

The calibration method can also be used for an AFM with the sample-on-scanner design, Figure 2-2. However, it would require that a cantilever holder be mounted and centered

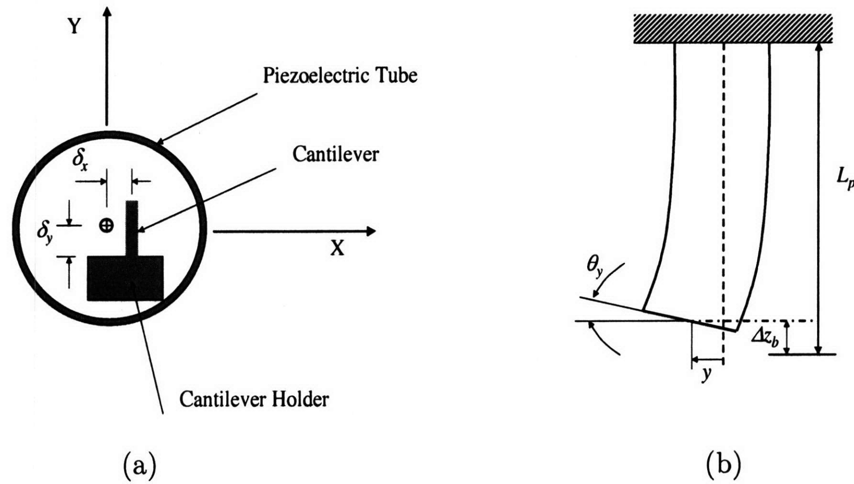

Figure 3-4: (a) Cross section of scanner with sample holder, (b) Geometric coupling between scanner bending and extension.

on the scanner. The piezoresistive cantilever can then be mounted on the holder and the scanner calibration can be obtained. Finally, some means for biasing the piezoresistors is needed. This may or may not be a challenge, depending on the AFM design.

3.4 Summary

In this chapter, a new method was developed and presented to allow calibrating the scanner's vertical displacement up to its full range, in addition to characterizing scanner hysteresis. Analysis demonstrating the practical feasibility of the method using piezoresistive cantilevers was performed in addition to a first order error analysis.

Chapter 4

Model Validation

4.1 Experimental Setup

The setup used is based on a Quesant AFM [39]. The scanner used has a scan range of $40\,\mu m$ and vertical range of about $4.25\,\mu m$. To reduce the effect of noise, and environmental effects due to temperature changes the AFM is placed inside an acoustic isolation chamber [41]. Further, the AFM and the chamber are placed on top of a bench-top pneumatic vibration isolation table [40], to reduce the effect of mechanical vibrations.

4.2 Modifications to Experimental Setup

The setup will be used for model validation, implementing custom controllers and scan algorithm. Therefore, several modifications were required to enable performing the desired experiments. A dSPACE controller board [42], was used to implement custom algorithms. The board has 16-bit analog-to-digital converters (ADC), and 14-bit digital-to-analog converters (DAC), and a 400 MHz IBM PowerPC 604e processor. Interface software accompanying the board allows using MATLAB and SIMULINK codes. The software can automatically generate executable code ready for real-time implementation. Code was developed in MATLAB environment to allow probe-sample engagement, probe retraction, feedback control, and scanning and image collection. The codes were implemented using a sampling frequency of $60\,kHz$, while the expected feedback bandwidth is less than $1\,kHz$. Therefore,

delay effects due to sampling will have practically no effect of feedback performance. In addition, the drive electronics of the AFM had to be bypassed. Accordingly, a high-voltage piezoelectric amplifier was built based on commercial cards [39]. To further reduce noise from the amplifier, filters were built and added to the amplifier. The amplifier has 3 input channel with a range of $\pm 10\,V$ and 5 output channels at $\pm 200\,V$. One out channel is dedicated to the scanner electrode for Z motion, while X and Y-motions use two channels each. The X/Y channels have a $-3\,dB$ bandwidth of $300\,Hz$, and a peak-to-peak output noise of $50\,mV$ while connected to the scanner. The capacitance of the scanner is $8\,pF$. On the other hand, the Z-channel has $-3\,dB$ bandwidth of $2.4\,kHz$ with a phase of -45° at that frequency, and a peak-to-peak output noise of $50\,mV$. In addition, a K-type thermocouple was mounted inside the acoustic chamber to monitor Air temperature.

4.3 Cantilever Specifications

Experimental results will be shown for two different Silicon cantilevers with rectangular cross-sections. Cantilevers are labeled A [44], and B [45]. Cantilever-A has a length of $350\,\mu m\,\pm 5\,\mu m$, a width of $35\,\mu m\,\pm 3\,\mu m$, a thickness of $1\,\mu m\,\pm 0.3\,\mu m$, a resonance frequency between 7 to $14\,kHz$, and a stiffness between 0.01 to $0.08\,N/m$. Cantilever-B, on the other hand, has a length of $450\,\mu m\,\pm 5\,\mu m$, a width of $50\,\mu m\,\pm 5\,\mu m$, a thickness of $2\,\mu m\,\pm 0.5\,\mu m$, a resonance frequency between 10 to $17\,kHz$, and a stiffness between 0.07 to $0.4\,N/m$. Both cantilevers have a probe length between 15 to 20 μm, and radius of curvature of less than $15\,nm$. In the figures presented, * will be used as a superscript to denote the use of a nominal value of a parameter for converting the units of a measured signal.

4.4 Force-separation Curve

Equations (2.7,2.9,2.10,2.11), were used to generate the nondimensional composite force-separation curve of Figure 4-1. Parameters used to generate the curve are, $w = 0.1\,J/m^2$, $R_1 = 20\,nm$, $R_2 = \infty$, $\nu_1 = 0.3$, $\nu_2 = 0.27$, $E_1 = 169\,GPa$, $E_2 = 6\,GPa$, $H = 1 \times 10^{-19}\,J$, and $\sigma_o = 5 \times 10^8\,N/m$, where subscripts 1 and 2 correspond to the probe and sample,

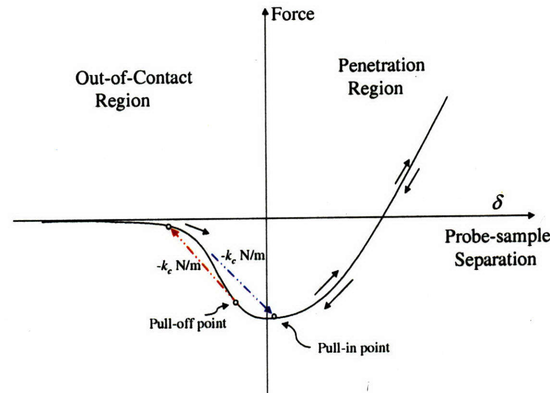

Figure 4-1: Simulation: Quasi-static normalized force-separation curve.

respectively. It is worth noting that the model of Equation (2.7) can predict an instability that has been observed in quasi-static experiments. This quasi-static instability, as seen in Figure 4-2, occurs when an approaching/receding probe jumps in/out of contact (pull-in/pull-out points), with the sample surface corresponding to a sudden jump in the contact area. The actual point of instability on the force-separation curve will depend on the stiffness of the cantilever k_c, as shown in Figure 4-1. The cantilever stiffness is estimated from Figure 4-2 as the slope of the line just after the pull-off point. The stiffness is estimated to be $0.06\,N/m$, which is in good agreement with the values given in Section 4.3. It can be seen from both figures that the model captures the main characteristics of the experimental curve. However, the difference in the approach and retract lines (i.e. hysteresis), is not captured. This behavior may be attributed to viscoelastic behavior of the sample in addition to scanner hysteresis.

4.5 Scanner Modes Identification

In order to identify the main resonance frequencies of the scanner, several experiments were performed. In one experiment, the piezoelectric tube, Figure 4-3 (b), was excited by applying a voltage to the two outer electrodes $x+$ and $x-$ and the charge q_p, on both the $y+$ and $y-$ electrodes was measured. The measured charge is proportional to the strain or mechanical displacement, at least for small input amplitudes, since the applied voltage on

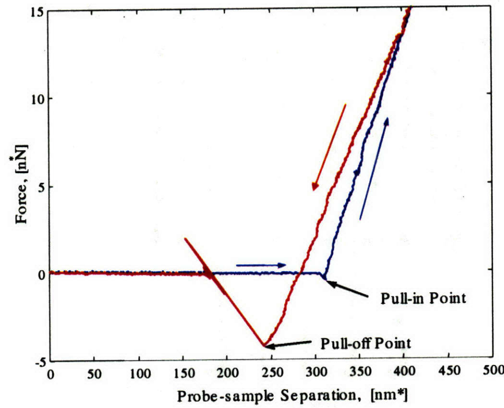

Figure 4-2: Experimental force-separation curve

the $y+$ and $y-$ electrodes is zero. This can be seen from Equation (2.14). The induced stain is mainly due to the Z-axis displacement, in addition to a small contribution from the bending modes as a result of coupling. However, the coupling induced strain will have an opposite effect on the $y+$ and $y-$ electrodes; one being negative while the other positive. By adding $q_p(y+)$ and $q_p(y-)$, the effect of bending almost cancels out. Since each of the electrodes will experience bending about both the X and Y-axis, a small contribution from bending modes will be seen in the measured charge. Figure 4-3 (a), shows the frequency response for this case labeled $V_{x+x-} \rightarrow q_p(y+) + q_p(y-)$. The scanner's main longitudinal modes are at 4.6, 8, and 21 kHz. To identify the main bending modes in the X-direction, a voltage signal was applied to the $x+$ electrode, and the charge on the $x-$ electrode was measured. The result is labeled $V_{x+} \rightarrow q_p(x-)$, in Figure 4-3 (a). A similar experiment was performed for the Y-axis, and the result was found fairly identical to that for the X-axis. The main bending modes are at 380 Hz, 3.4 and 11.8 kHz. However, there is a small resonance at 540 Hz which the tests failed to identify its source. Because of its small peak compared to other system resonances, further investigations for its source was not performed. Further, the data labeled $V_z \rightarrow y_{PSD}$ in Figure 4-3 (a), are from V_z to the detector's output y_{PSD}, while the cantilever is not in contact with a sample. As seen from the plot, the bending modes are observable from the feedback signal, as predicted by the model, Equation (2.88).

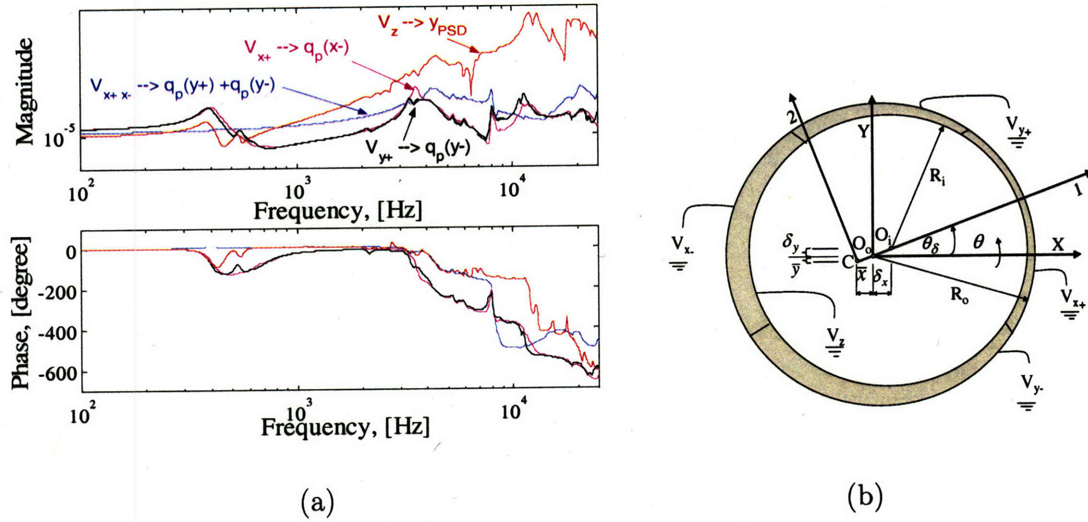

Figure 4-3: (a) Experimental frequency response, (b) Cross-section of the piezoelectric tube.

4.6 In-contact Dynamics

As described earlier, during scanning, y_{PSD} is used as a feedback signal, while V_z is used as a control input. Due to feedback bandwidth limitations, scan speed is typically more than an order of magnitude lower than the frequency of the first bending mode. As a result, the effect of this low scan speed lateral motion on the feedback loop is not dramatic. Consequently, it is essential to identify and understand the dynamics between the feedback input-output pair (V_z, y_{PSD}). In this section, the focus will be on hysteresis and creep-free dynamics. Hysteresis and creep will be addressed in Sections 4.8 and 4.9, respectively. Simulations will first be introduced followed by experimental results.

4.6.1 Frequency Responsc: Simulations

The models presented in Sections 2.3.1 to 2.4, and 2.6, are presented below in transfer function form

$$\begin{aligned} z_c'(s) &= \sum_{i=1}^{i^*} \frac{(a_{2zi}s^2 + a_{1zi}s)}{s^2 + 2\zeta_{ci}\omega_{ci}s + \omega_{ci}^2} z_p(s) + \frac{(a_{2\theta i}s^2 + a_{1\theta i}s)}{s^2 + 2\zeta_{ci}\omega_{ci}s + \omega_{ci}^2} \theta_{py}(s) \\ &+ \frac{a_{fi}}{s^2 + 2\zeta_{ci}\omega_{ci}s + \omega_{ci}^2} f(z_c, z_p, \theta_{py}, z_s) \end{aligned} \tag{4.1}$$

$$\theta_{py}(s) = \sum_{j=1}^{j^*} \frac{k_{j\theta} V_z}{s^2 + 2\zeta_{\theta_j}\omega_{\theta_j} s + \omega_{\theta_j}^2} \tag{4.2}$$

$$z_{sh}(s) = \sum_{m=1}^{m^*} \frac{k_{z_pm} V_z}{s^2 + 2\zeta_{z_pm}\omega_{z_pm} s + \omega_{z_pm}^2} \tag{4.3}$$

$$y_{PSD} = \theta_{ysh} - z_c' \tag{4.4}$$

where i^*, j^*, and m^* are the number of modes retained for the cantilever, scanner bending and longitudinal dynamics, respectively. The probe-sample interaction force $f(z_c, z_p, \theta_{py}, z_s)$, is a nonlinear function of probe-sample separation, and depends on geometry, environment, and probe and sample material properties. To obtain a linear model to be used for analysis, the force was expanded as a Taylor series and linear terms were retained, giving

$$\begin{aligned} f(z_c, z_p, \theta_{py}, z_s) &= g_c z_c' + g_z z_p + g_{\theta_{py}} \theta_{py} \\ &\quad + k_s z_s + H.O.T. \end{aligned} \tag{4.5}$$

where k_s can be considered as a linear effective probe-sample contact stiffness. The probe-sample contact can be represented schematically as in Figure 4-4, where again z_c', is measured relative to z_p. The contact and cantilever stiffnesses, are represented as two springs in series. The contact stiffness does not change the order of the model, but has a great impact on the system's zeros. Substituting Equations (4.2), (4.3), and (4.5) into Equation (4.1), and the resulting equation into Equation (4.4) gives the overall transfer function between V_z and y_{PSD}, which describes the AFM Z-dynamics. The effect of probe-sample contact properties on system zeros can be explained by considering a reduced order model where bending dynamics θ_{yp} consists of the first bending mode and first zero-pair. In addition, the scanner extention dynamics and cantilever flexural modes are ignored as they are typically much faster than the bending dynamics of the scanner. The resulting model is given as

$$y_{PSD} \approx \theta_{yp} - g_{\theta_{yp}} \theta_{yp} - g_z' z_p \tag{4.6}$$

$$\begin{aligned} y_{PSD} &\approx \frac{b_2 s^2 + b_1 s + b_0}{s^2 + a_1 s + a_0} V_z - g_{\theta_{yp}} \frac{b_2 s^2 + b_1 s + b_0}{s^2 + a_1 s + a_0} V_z \\ &\quad - k_z g_z' V_z \end{aligned} \tag{4.7}$$

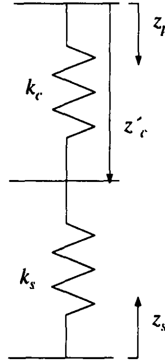

Figure 4-4: Schematic of probe-sample contact.

where k_Z and g'_z are proportionality constants. As seen from Equation 4.7, the first two terms are due to the scanner bending mode. The coefficient $g_{\theta_{yp}}$ multiplying the second term depends on the probe-sample contact properties and surface forces between the sample and probe. It is clear that changes in the contact properties (e.g. nominal contact force set-point) would affect the zeros of the transfer function. However, the frequency of the bending mode would not be affected as seen in Fig. 4-18. Physically, this is true since the probe sample forces are orders of magnitude smaller than the force the scanner can provide, ($\sim 10's\, nN$ vs. $\sim 1N$).

The model used in this study included four bending modes and two extension modes for the scanner, in addition to a single bending mode for the cantilever. The parameter values used are given in Appendix A. The ratio of sample to cantilever stiffness $\frac{k_s}{k_c}$, proved to be an important parameter. Changes in this ratio have two main effects on the model transfer function, namely, changes in the DC gain and changes in the frequency of the zeros associated with the bending modes at $380\,Hz$ and $3.4\,kHz$. Figure 4-5, shows the simulated frequency response of the model for different ratios of stiffnesses. For large ratios (e.g. $\frac{k_s}{k_c} = 7$), the zeros are at a higher frequency than those of the modes. For smaller ratios (e.g. $1 \leq \frac{k_s}{k_c} \leq 2$), their frequency decreases to be below that of the modes. This change in pole-zero pattern is referred to as pole-zero flipping. Moreover, for some value ($\frac{k_s}{k_c} \approx 4$), there is pole-zero cancelation and thus, the bending modes become unobservable. Figure

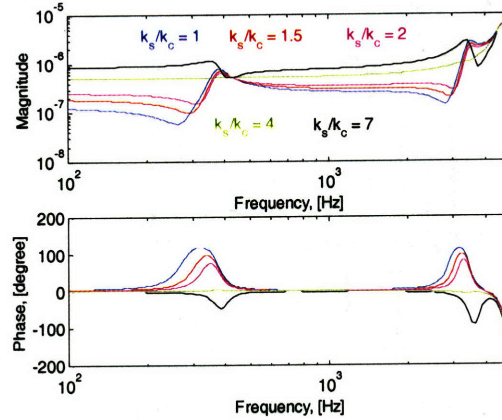

Figure 4-5: Simulation: In-contact frequency response for different ratios of sample to cantilever stiffness $\frac{k_s}{k_c}$.

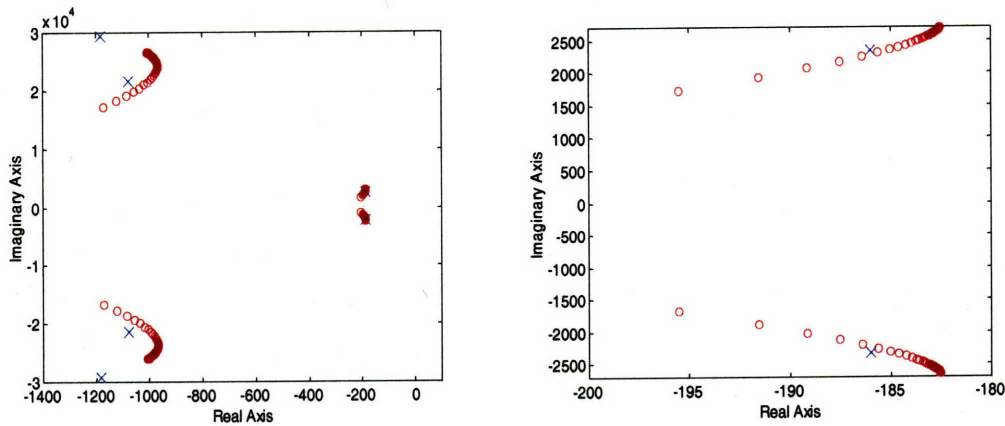

Figure 4-6: Pole-zero map as a function of $\frac{k_s}{k_c}$: (left) zoom on the $3.4\,kHz$ mode, (right) zoom on the $380\,Hz$ mode.

4-6, presents a pole-zero map of the first two modes for different values of $\frac{k_s}{k_c}$. As a result, as the zeros move away from the mode, the resonance peak appears more prominent in the response. Furthermore, when $\frac{k_s}{k_c}$ is either too large or too small, the DC gain reaches a limit controlled by k_c and k_s, respectively. For intermediate values, the DC gain will depend on both stiffnesses and changes in k_s due to different set-pints or input amplitudes will change the DC gain, and zeros location.

The model can be further improved on to include nonlinearities in the contact affecting the DC gain and dissipation. These nonlinearities depend in great part on properties of the sample. Hence, the form of this dependence is not known. It is possible to account for it

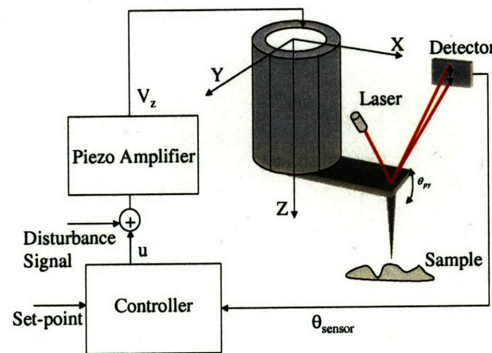

Figure 4-7: System identification block diagram.

in the model by generalizing the probe-sample force to include dissipative terms and retain higher order terms. Therefore, Equation (4.5), changes to $f(z_c, \dot{z}_c, z_p, \dot{z}_p, \theta_p, \dot{\theta}_p, z_s)$.

4.6.2 Frequency Responsc: Experiments

The samples chosen for these experiments were Glass and Polydimethylsiloxane (PDMS), having Young's moduli of elasticity of 60 MPa and 2.5 MPa, respectively. The experimental procedure is as follows, the probe was brought into contact with the sample until the desired set-point is attained. The system was run in feedback with a PI controller. A disturbance signal generated by a Dynamic Signal Analyzer HP35670A, was injected at the input to the piezoelectric amplifier, as seen in Figure 4-7. The signal going to the amplifier input is comprised of the disturbance signal plus the controller output. The amplifier input in addition to the laser output signal were sent to the analyzer to obtain the frequency response of the system. The results will be shown for different cantilevers. In addition, the effect of the force set-point and input voltage amplitude on the dynamics will be investigated. This will aid in choosing scan parameters to achieve a good dynamic response and improve image quality.

Cantilever-A: Glass Sample

Figure 4-8, shows the force displacement curve for the Glass sample. The points labeled on the plot are the force set-points used for the frequency response experiments. The effects

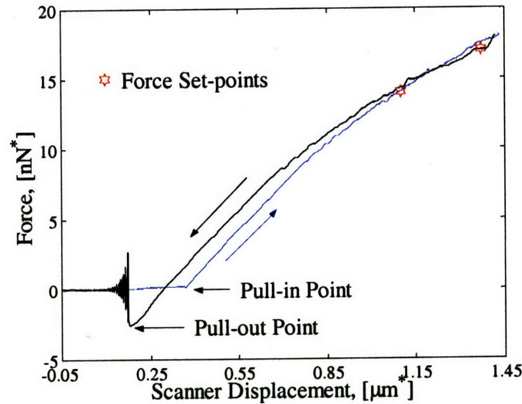

Figure 4-8: Force displacement curve for cantilever-A with a Glass sample.

of the force set-point on the dynamics can be seen from Figure 4-9. For the larger set-point of $17.6\,nN$, the DC gain is smaller and the $380\,Hz$ bending mode has a smaller resonance peak. The decrease in DC gain suggests that the effective contact stiffness has decreased, hence, the scanner displacement is transmitted more to the smaller stiffness; the contact's. The smaller resonance peak could be due to two reasons; the frequency of the zero-pair associated with the bending mode has slightly decreased for the larger set-point. Hence, the contribution of the bending mode appears less prominent in the response. In addition, it could be a result of changes in the dissipative properties of the contact with changes in the set-point. It is important to realize that the bending mode resonance frequency does not change. The contact forces are orders of magnitude smaller than the force the scanner can provide, $\sim 10's\,nN$ vs. $\sim 1N$.

The effect of excitation amplitude on the frequency response is shown in Figures 4-10 and 4-11 for set-points of $14\,nN$ and $17.6\,nN$, respectively. It is seen that the larger the amplitude of excitation, the smaller the DC gain. The amount by which the DC gain changes depends on the value of the set-point. Here, the larger the set-point, the less the change is. At a large contact force, more plastic deformation might occur in the contact, which in turn reduces the effective contact stiffness. Contacts with higher level of plastic deformation, would experience smaller change in the contact stiffness and hence the DC gain. The resonance peak also changes due to variation in the frequency of the bending

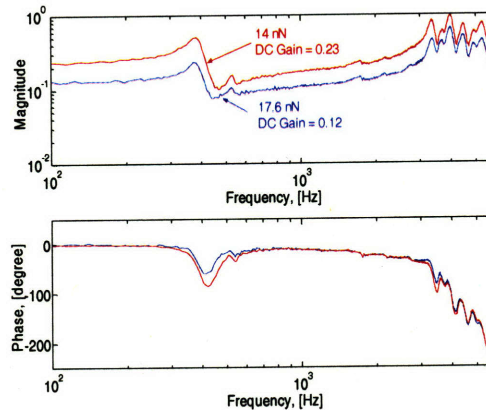

Figure 4-9: In-contact frequency response of cantilever-A with a Glass samplc: same amplitude for different set-points.

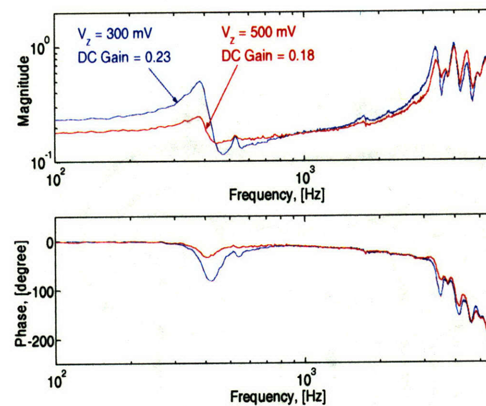

Figure 4-10: In-contact frequency response of cantilever-A with a Glass samplc: $14\,nN$, different amplitudes.

mode zeros. It is worth noting that the changes in the dynamic behavior greatly differs around the first and second bending modes, possibly due to variation in the viscoelastic response of the contact at different frequencies.

Cantilever-A: PDMS Sample

Figure 4-12, shows the force displacement curve for the PDMS sample. The penetration region seems quite linear. This implies that what is being measured by the PSD is mainly the deflection of the cantilever and not the deformation of the sample. This suggests that cantilever stiffness is much smaller than the effective stiffness of the sample at that location. Compared to results in Figure 4-8, the suggestion is surprising since the modulus of elasticity

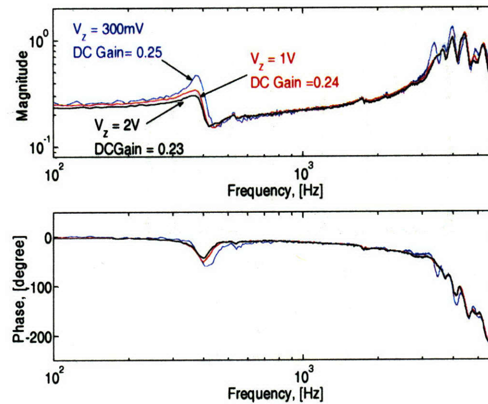

Figure 4-11: In-contact frequency response of cantilever-A with a Glass samplc: $17.6\,nN$, different amplitudes.

of PDMS is a factor of 24 smaller than that of Glass. However, the values of the moduli are bulk values and they may not represent the local properties of the nano-contact. In addition, the experiments with the Glass sample were performed before those of the PDMS sample. It may be possible that the probe has become blunt. As a result, the contact stress would be smaller for the same applied force. The results in Figures 4-13 to 4-15, are similar to those for the Glass sample, except for the changes in resonance peak. As seen in Figures 4-14 and 4-15, the frequency of the bending mode zeros does not change with excitation amplitude. This again implies that the contact stiffness is much greater than the cantilever stiffness. As predicted by the model, most of the response will be absorbed by the cantilever with little sample deformation. Therefore, the changes in resonance peak may be due to changes in the dissipative properties of the contact.

Cantilever-B: PDMS Sample

The results with the Glass sample are similar to those with cantilever A and therefore, will not be presented. However, the results with the PDMS sample are different and will be presented and discussed.

Figure 4-16, shows the force-displacement curve for the PDMS sample. The penetration region seems quite nonlinear. This implies that what is being measured by the PSD signal, at least in part, is the deformation of the sample. The observations in Figure 4-17 for a $36\,nN$ set-point, are that increasing the input amplitude reduces the DC gain, and the

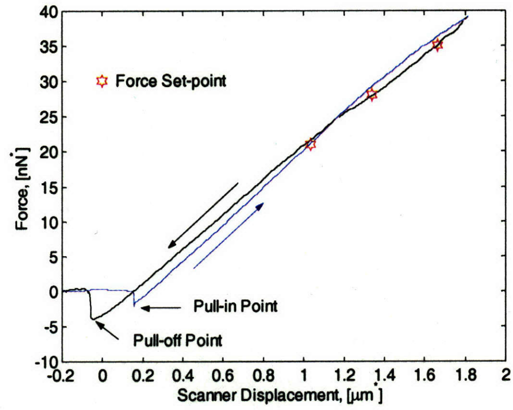

Figure 4-12: Force-displacement curve for cantilever-A with a PDMS sample.

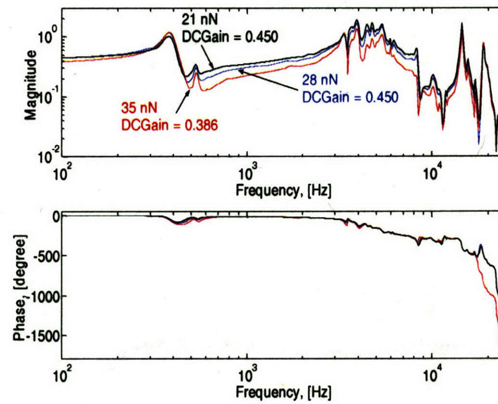

Figure 4-13: In-contact frequency response of cantilever-A with a PDMS samplc: $17\,nm$ amplitude for different set-points.

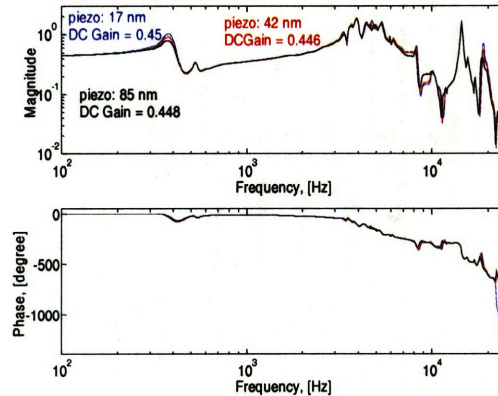

Figure 4-14: In-contact frequency response of cantilever-A with a PDMS samplc: $21\,nN$ for different amplitudes.

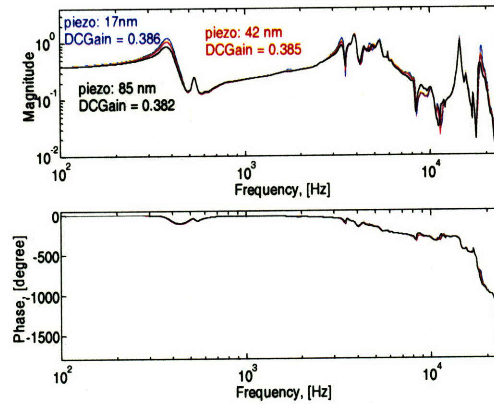

Figure 4-15: In-contact frequency response of cantilever-A with a PDMS samplc: $35\,nN$ for different amplitudes.

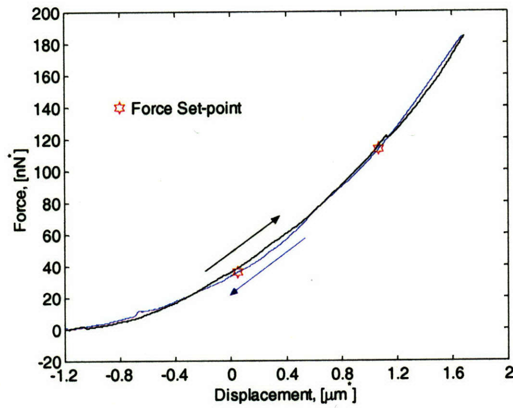

Figure 4-16: Force displacement curve for cantilever-B with a PDMS sample.

frequency of bending-mode zeros, thus, increasing the resonance peak. This suggests that the contact stiffness decreases with increased amplitude. In addition, increasing set-point, Figure 4-18, results in pole-zero flipping for the first two bending modes. In addition, there is no change in the location of the zeros with input amplitude for the $113\,nN$ step-point, as seen in Figure 4-19. This implies that increasing the higher set-point increased the effective contact stiffness, which agrees with Figure 4-16. These results are in agreement with model predications in section 4.6.1, (Figure 4-5); implying that the contact and cantilever stiffness values are relatively close at the $36\,nN$ contact point.

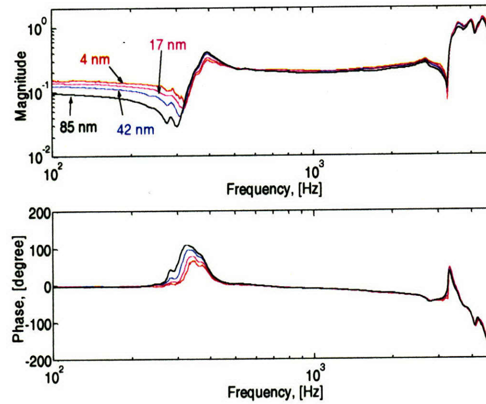

Figure 4-17: In-contact frequency response of cantilever-B with a PDMS samplc: $36\,nN$ for different amplitudes.

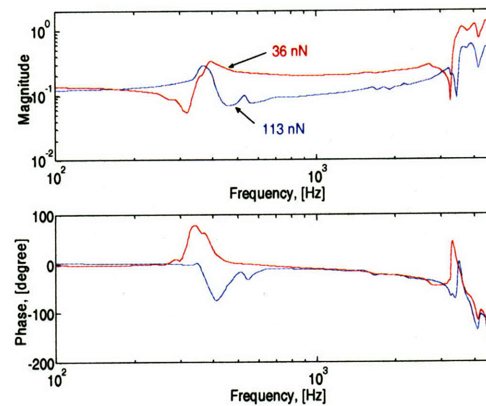

Figure 4-18: In-contact frequency response of cantilever-B with a PDMS samplc: $17\,nm$ amplitude for different set-points.

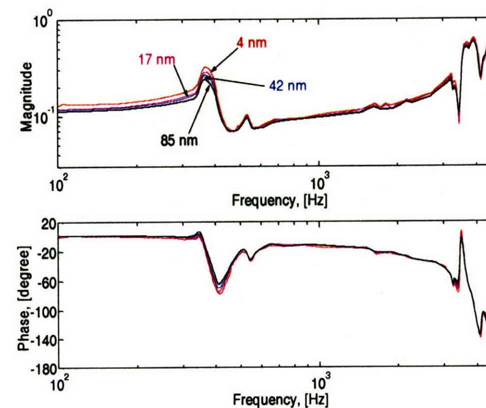

Figure 4-19: In-contact frequency response of cantilever-B with a PDMS samplc: $113\,nN$ for different amplitudes.

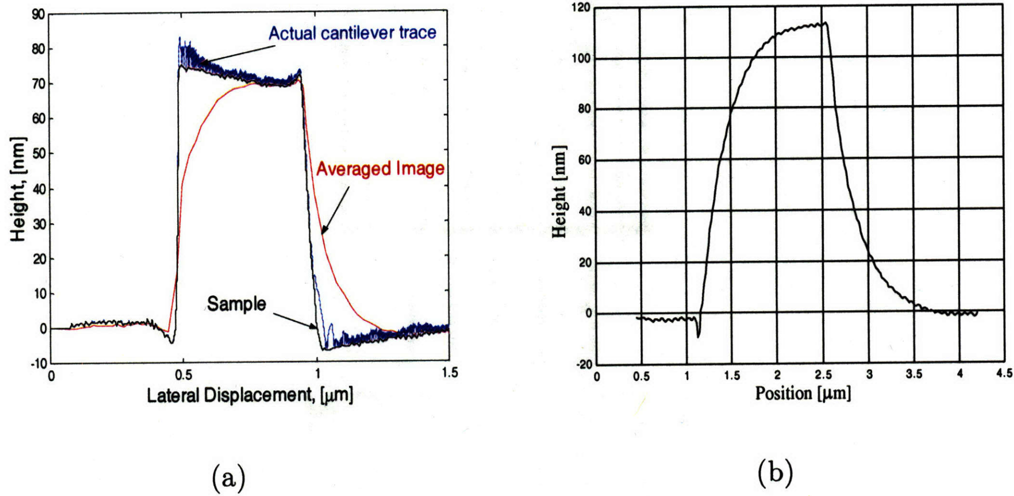

(a) (b)

Figure 4-20: Images of calibration steps using a PI controller: (a) scanning simulation, (b) experiment.

4.7 Scanning Simulation vs. Experiments

Scanning simulations were performed using the developed models. The sample shape used in simulation is an experimental AFM image of calibration steps. Figure 4-20 (a), shows the simulated image vs. the actual sample. It can be seen that the sampled and averaged image generated from the voltage V_z, does not correspond well to the actual image. The cantilever oscillations causes it to loose contact with the sample and the hammering action could in fact be damaging to the sample. The AFM image shown in Figure 4-20 (b) is of the steps used in the simulation. The simulations predict the actual response well. Also note that the oscillations observed in Figure 4-20 (b), which are due to the bending mode, introduce an artifact that could be interpreted incorrectly as surface roughness.

4.8 Scanner Hysteresis

The nonlinear voltage to displacement sensitivity of the scanner was measured by applying a $10\,Hz$ sinusoidal input and measuring the bending response of the scanner. The input amplitude was varied from $20\,V$ up to the maximum allowable voltage of $400\,V$. The results are shown in Figure 4-21 with the input voltage scaled down by a factor of 10. The data are typical of a PZT scanner where sensitivity initially increases with increased input

amplitude. Although not seen from the data, however, when the input amplitude exceeds a certain limit, the sensitivity starts decreasing with increased input amplitude approaching a saturation limit. This limit is avoided in practice as it brings the input electric field close to the depolarization field where piezoelectric effect would be lost. A 2nd order polynomial was fitted to the data. The maximum relative error of the fit is 7 % for the range 40 to 400 V. A linear fit was applied to the low-voltage data points and is also shown in Figure 4-21. The linear fit gives a 24% error at full range. Accordingly, for a 5 μm scanner there would be an error of 1.2 μm at full scale using this linear fit as is commonly done. The new calibration method presented in Chapter 3, can be used to generate data similar to Figure 4-21, which would allow for accurate calibration of the scanner. Therefore, eliminating the shortcomings of using an AFM for measuring tall structures as in optical and semiconductor devices.

Figure 4-22, presents experimental hysteresis loops for the piezoelectric scanner. The input signal is a 10 Hz sine wave with amplitudes of 20, 50, and 100 V. In the figure, the input values are scaled down by a factor of 10. The hysteresis loops can be characterized by their average slope, loop center point, and the loop width. These characteristics change with the input amplitude. As discussed in Section 2.3.5, hysteresis in piezoelectric actuators occur mainly in the electrical domain between the applied electric field and the electric displacement (or charge q_p). Therefore, in order to use the hysteresis model of Equation (2.72), the current $\dot{q}_p$, needs to be measured. Measuring the current given the high input voltage is practically difficult and therefore, not used in practice. Some authors have used the derivative of the input signal instead [95], and fitted the Bouc-Wen model to a single hysteresis loop. However, using the input derivative will fail to capture the changes in the characteristics of the hysteresis loop at various input amplitudes. The Bouc-Wen model was fitted to the 100 V hysteresis loop of Figure 4-22, and the model was later used to predict hysteresis loop for the 50 V input. The results are given in Figure 4-23, where it is seen that the model fails to accurately simulate the smaller loop. This is mainly due to the nonlinearity in the voltage to charge response which will is not captured when the derivative of the input is used instead of the current. A similar tested was done using the

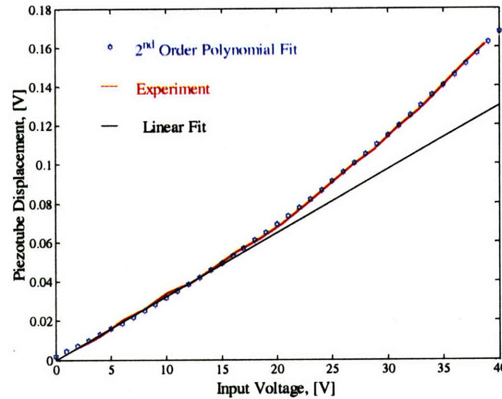

Figure 4-21: Nonlinear voltage to displacement quasi-static curve of piezoelectric tube.

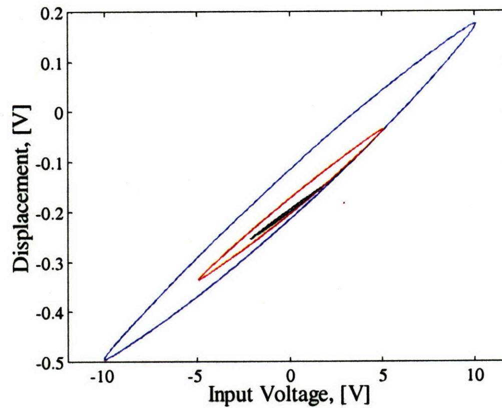

Figure 4-22: Experimental hysteresis curves for scanner for a sinusoidal input at $10\,Hz$: $20\,V$, $50\,V$ and $100\,V$.

Coleman model, and the results are shown in Figure 4-24. A solution for this problem is not presented in this thesis. However, the main thesis contributions in dealing with hysteresis in AFM are developing the method of Chapter 3, that allows characterizing hysteresis for the full range of scanner displacement. In addition, developing a realistic scanner model that can accommodate a hysteresis model in a physically-consistent manner. Finally, identifying limitations of some of the methods that has been proposed in the literature [95].

4.9 Scanner Creep

A commercial AFM was used to measure the creep response of its piezoelectric scanner. The AFM probe was brought into contact with a hard sample (Glass sample), while in open loop.

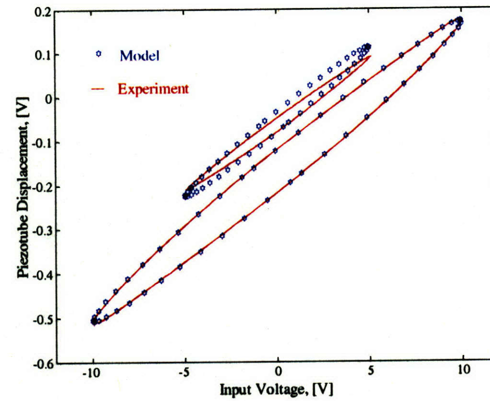

Figure 4-23: Hysteresis loops: experiments vs. simulations using the Bouc-Wen model.

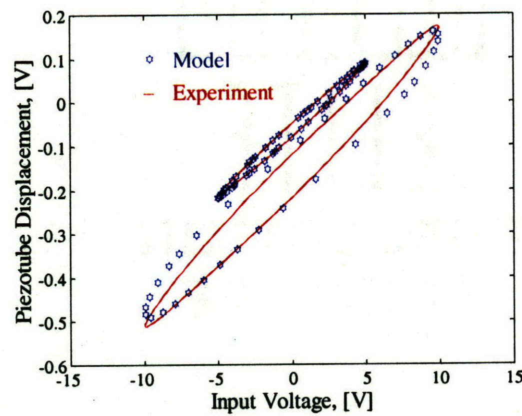

Figure 4-24: Hysteresis loops: experiments vs. simulations using the Coleman model.

Commanding the scanner to move up/down in the Z-direction, changes the PSD signal accordingly. This signal shows the scanner response including creep. However, the measured PSD signal could also change due to the response of the AFM structure or scanner to variations in the environment temperature, and/or mechanical vibrations. More so, variations in the laser source output, heating of the cantilever by the laser source, cantilever bending due to thermal gradient between the probe and sample, relaxation in probe-sample contact, and/or drift in the drive or sensing electronics can affect the PSD output. All these factors are considered sources of noise in the creep data. To minimize their effect on measurement and obtain a good signal-to-noise ratio, the AFM was placed inside an environmental and vibration isolation chamber. The system was given enough time to reach an equilibrium state, before data collection. A thermocouple measuring the Air temperature inside the chamber was used to record the extremum temperatures during the experiments. Typical temperature fluctuation was 0.4^oC over the duration of an experiment, $30 - 40$ minutes. The choice of cantilever was dictated by a trade-off between sensitivity and noise. A low stiffness gives a high displacement sensitivity and a small probe-sample force. This reduces the effect of possibly nonlinear material behavior of the sample on the measurements. On the other hand, the cantilever stiffness should not be too low causing reduced resolution by increasing the cantilever displacement response to thermal noise. Another concern is the choice of nominal cantilever deflection (PSD signal). The cantilever deflection vs. scanner displacement curve can exhibit nonlinear behavior hence degrading the linearity of the measurements. The selected nominal deflections and operating range during experiments were chosen to be within the mostly linear part of the curve. In addition, the input voltage V_z, was chosen to be small enough to ensure good linearity in scanner displacement. The excitation signals consisted of steps and ramp signals that are saturated in amplitude. The rate of ramp signal was varied to study the effect of input rate on creep response. The PSD signal was recorded before the scanner is excited to measure total instrument drift (noise). During the experiments, the scanner was commanded to move down a certain displacement. After several minutes it was commanded to move the same displacement up. Both data were combined and averaged to cancel the effect of drift in the PSD signal.

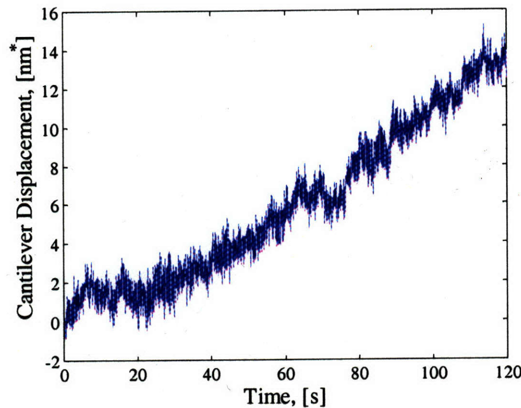

Figure 4-25: Pre-data collection drift in PSD signal.

Two Silicon cantilevers were used for these experiments. A cantilever with nominal stiffness of $0.03\,N/m$ that had an equivalent displacement noise of $14\,\AA\,rms$ and $7\,nm$ peak-to-peak at $100\,Hz$. The second cantilever had a nominal stiffness of $0.2\,N/m$ and an equivalent displacement noise of $5.1\,\AA\,rms$ and $3.5\,nm$ peak-to-peak at $100\,Hz$. A typical scan requires 2 to 5 minutes to complete, depending on scan rate and image resolution. Ideally, this is the necessary duration for characterizing scanner creep. Instrument drift of $1.4\,\AA/s$ was typical, Figure 4-25. Data collection was limited to a maximum of 3 minutes to ensure small contributions of instrument drift to the collected data.

To test the linearity of creep response, different voltage ramp signals with different saturated amplitudes were used. All signals had the same ramping rate of $1\,V/s$, hence, ramping time was different for each input. The amplitudes were chosen to be small enough such that the nonlinearity in the scanner fast response would not be a concern. The results are shown in Figure 4-26, where the cantilever response to a $260\,nm$ scanner displacement is compared with the response to a $104\,nm$ displacement which has been scaled by a factor of $\frac{260}{104} = 2.5$. The Figure shows the good linearity of the response. This tends to suggest that the creep part of the response tends to scale linearly with the fast response. Therefore, a linear model of creep may be justified. The nonlinearity in the fast scanner displacement could be accounted for separately. Figure 4-27, displays the creep response for two ramp inputs of the same saturated amplitude but ramped over $200\,\mu s$ and $10\,ms$. The response

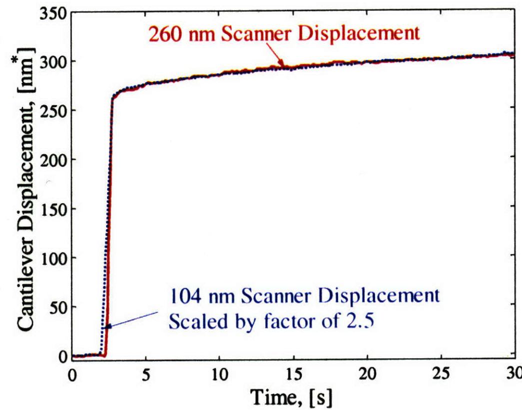

Figure 4-26: Experimental creep responsc: Linearity of response.

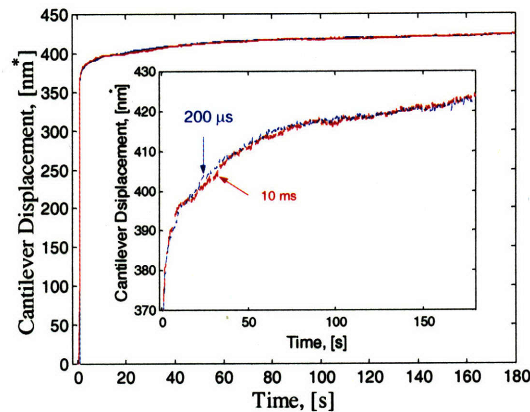

Figure 4-27: Creep response to inputs with different rates.

does not show any dependence of creep rate on input rate.

Figures 4-28 and 4-29 show the response of the LTI and logarithmic models, respectively. The parameter values for the logarithmic model are, $\gamma = 0.12$, and $t_o = 0.18\,s$. A $3rd$ order LTI model was used with poles at $3.98\,mHz$, $79.57\,mHz$, and $1.59\,Hz$ and zeros at $4.48\,mHz$, $84.79\,mHz$, and $1.71\,Hz$. Both models reproduced the creep response reasonably well. The fit for both models degraded at larger times. The fit can be improved by increasing the order for the LTI model or adding more terms of different rates in the logarithmic model.

A model used to predict and compensate for creep in AFM has to be able to reproduce creep behavior under excitations during typical operation. The input signals for lateral motion (scanning), are a triangular wave, not necessarily with a linear slope, and a ramp

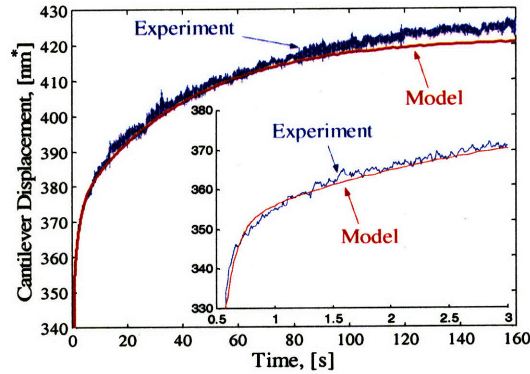

Figure 4-28: LTI creep model fitted to experimental responsc: insert shows a zoom on initial part of response.

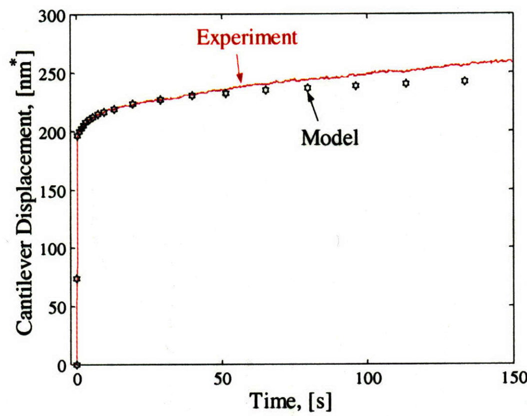

Figure 4-29: Logarithmic creep model fitted to experimental response.

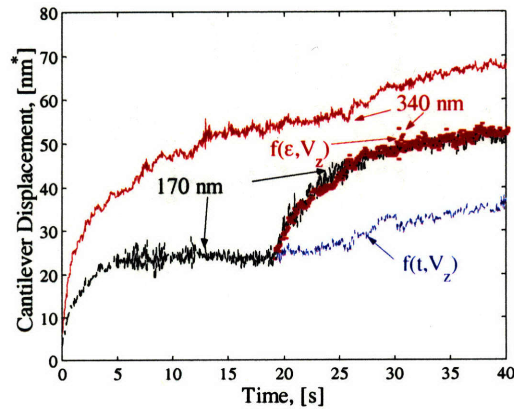

Figure 4-30: Creep response comparison between a single $340\,nm$ step and two $170\,nm$ steps.

for the fast and slow scan directions, respectively. The model fitting can be optimized specifically for these signals, yielding good agreement with actual response. The Z input voltage depends on sample topography and is not known a priori. Hence, a creep model for the Z-direction scanner displacement has to be capable of reproducing scanner creep not only for a prescribed input signal.

Both models presented displayed the ability to closely predict creep response for a step-like input. However, the structure of the models is quite different. In the logarithmic model, the strain rate of the scanner (or velocity) is assumed to be an explicit function of time $\frac{d\epsilon}{dt} = f(t, V_z)$, suggesting that the scanner is a non-autonomous system. In contrast to the LTI model, $\frac{d\epsilon}{dt} = f(\epsilon, V_z)$, which is time-invariant (autonomous). Physically the scanner response depends on the input voltage V_z history and the state of strain ϵ of the scanner. To portray this graphically, two experiments were performed. In the first experiment, the scanner was stepped by $340\,nm$, and the PSD signal was recorded. In the second experiment, the scanner was stepped by half the displacement of the first experiment $170\,nm$ at time zero. After $19\,s$, it was stepped by an additional $170\,nm$. The creep part of the response is shown in Figure 4-30, for both experiments. The logarithmic model would predict, for the second $170\,nm$ step, the curve labeled $f(t, V_z)$ which is the portion of the $340\,nm$ curve after $t = 19\,s$. This prediction does not match the actual response. Conversely, the LTI model prediction labeled as $f(\epsilon, V_z)$ matches the actual response well. It was obtained using the portion of the $340\,nm$ curve starting at $24\,nm$. Hence, demonstrating that the creep response depends on the input and state of strain of the scanner and not explicitly on time.

Note that creep is also a function of temperature as the sensitivity of the scanner is. It is assumed however, that AFM would be operated in an environment where temperature fluctuations are not large. Otherwise, obtaining reliable measurements will be difficult.

Chapter 5

Creep Compensation

5.1 Introduction

It has been shown that the LTI model is more suitable for predicting creep response. To compensate for creep, the model was inverted and a pole at $10\,kHz$ was augmented to the inverse filter to limit exciting high-frequency system modes. The filter, as seen in Figure 5-1, was placed in series with the controller. To test the performance of the filter, Silicon steps of two different heights were imaged using different cantilevers than the ones used for collecting the creep data.

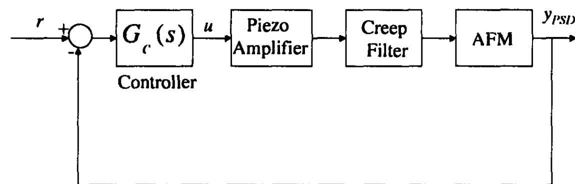

Figure 5-1: Feedback block diagram with creep compensation filter.

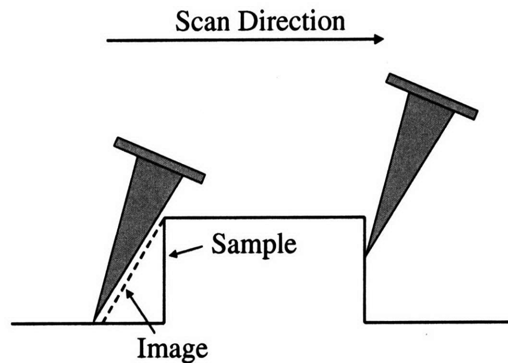

Figure 5-2: Feedback block diagram with creep compensation filter.

5.2 Creep Compensation

5.2.1 530 nm Steps

A Silicon Nitride cantilever with nominal stiffness of $0.37\,N/m$, a triangular cross section, and resonance frequency of $20kHz$ was used for results in Figures 5-3 and 5-5. This shows the images of $530\,nm \pm 1.5\,nm$ Silicon steps scanned at $2.8\,\mu m/s$ with and without creep compensation. The side walls of the steps appear to have different angles due to convolution errors. As shown in Figure 5-2, the probe was tilted with respect to the sample, hence, one side of the step is imaged by the probe's side wall instead of its tip. As a result, one side of the sample appears to the feedback system as a ramp disturbance, while the other could closely approximate a step disturbance. This allows examining the effect of the rate of disturbance on the image and compensation effectiveness. The image is created from the closed loop scanner input voltage responding to changes in sample topography (disturbance). The linear model of the system as given in Equation (2.75) has zeros which makes the response dependant on the disturbance rate in addition to amplitude. This explains why the amount of creep at the top of the steps is different from that at the bottom.

Without compensation, there is creep of $30\,nm$ ($5.7\,\%$ of step height), at the bottom of the step over $0.26\,s$. With compensation this reduces to $4.5\,nm$ ($0.85\,\%$ of step height). At the top, creep is $2.2\,nm(0.4\,\%)$ and $9.5\,nm(1.8\,\%)$ over $0.22\,s$ with and without compensation, respectively. Figures 5-4 and 5-5, show the image at a very slow scan speed of $17.5\,nm/s$

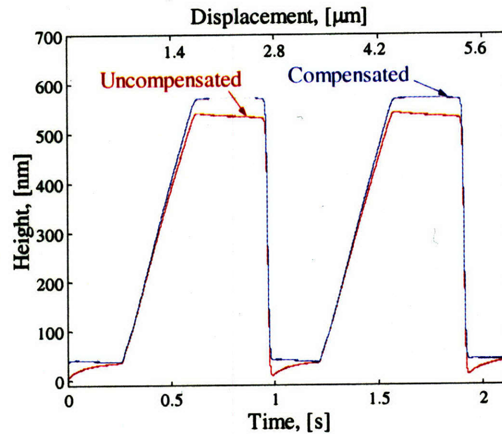

Figure 5-3: AFM image of 530 nm Silicon steps, with and without creep compensation, 2.8 $\mu m/s$.

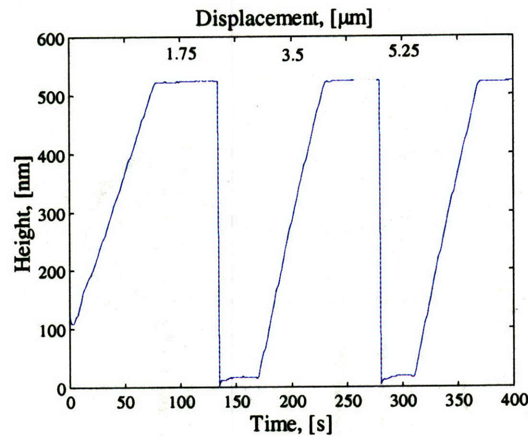

Figure 5-4: AFM image of 530 nm Silicon steps, with creep compensation, 17.5 nm/s.

with and without creep compensation. Without compensation, creep of 14.1 nm (3.1 %) over 35 s and 48.5 nm (10.1 %) over 35 s at top and bottom, respectively. With compensation, this reduces to 2.9 nm (0.57 %) over 50 s and 13.7 nm (2.6 %) over 35 s. The compensation, has dramatically reduced the effect of creep. However, as seen in Figure 4-28, there is as much as 5 nm error between the model and experiment during the first second of the creep response. As a result, Figure 5-4, peaks just after the right-side walls of the sample were not well compensated for.

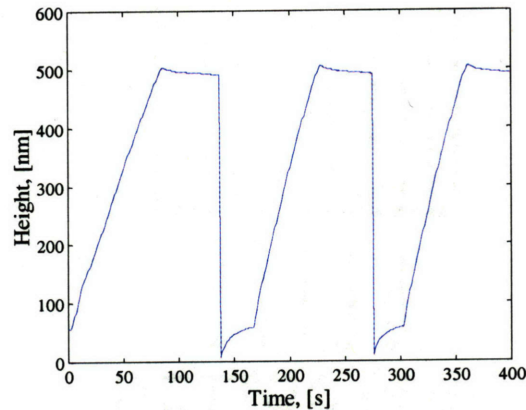

Figure 5-5: AFM image of 530 nm Silicon steps, without creep compensation, 17.5 nm/s.

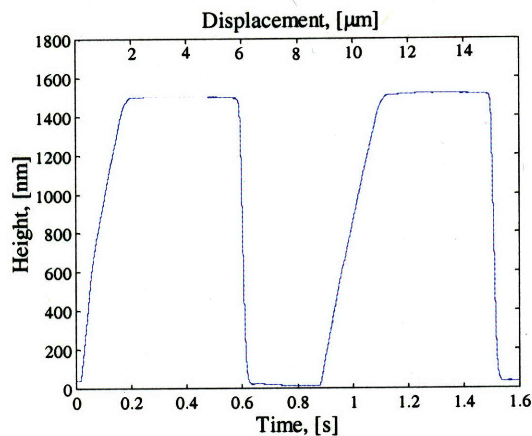

Figure 5-6: AFM image of 1590 nm Silicon steps, with creep compensation, 10 $\mu m/s$.

5.2.2 1590 nm Steps

In Figure 5-6, an image of 1590 $nm \pm 1.5\,nm$ steps is shown for a scan speed of 10 $\mu m/s$. The measured height is 1495 nm due to nonlinearity of scanner displacement (6 % nonlinearity). Creep at the top and bottom of the steps, with compensation, is 6 (0.4 %) and 8.3 nm (0.56 %) over 0.5 s. At a much slower scan speed of 41.67 nm/s, Figures 5-7 and 5-8, the images are shown with and without compensation. Un-compensated images show creep of 135 nm (9 %) and 143 nm (9.6 %) at the top and bottom of the steps. Compensated images show creep of 35 nm (2.4%) and 41.6 nm (2.8%). Note that the compensation did not degrade because of the larger sample height. This again suggests that the assumption of linearity in creep response is reasonable.

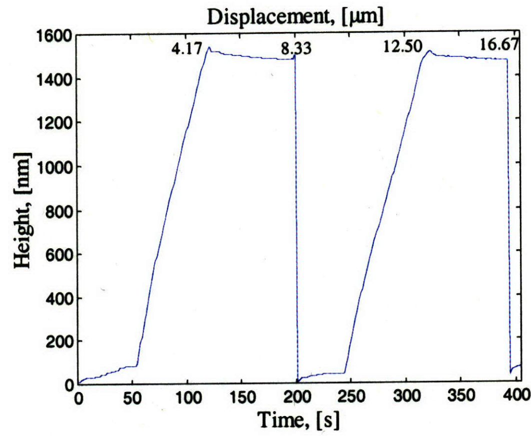

Figure 5-7: AFM image of 1590 nm Silicon steps, with creep compensation, 41.67 nm/s.

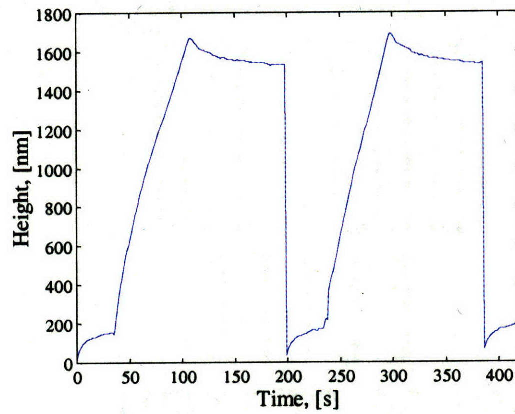

Figure 5-8: AFM image of 1590 nm Silicon steps, without creep compensation, 41.67 nm/s.

5.2.3 Notes on Parameter Identification for the Creep Model

The creep model need to be validated before it can be used for compensation. Validation data can be collected as described in Section 4.9. Alternatively, data could be collected while the system is in contact and in feedback. However, the initial part of creep will depend on the controller gains, and accurate data may not be easily obtained. In either scenario, the duration for data collection should be limited based on instrument drift. It is possible to automate the process of creep identification and compensation. The procedure for Z-axis creep identification can be performed as follows, using a hard sample and a low-stiffness cantilever. While the cantilever is far away from the sample, a frequency sweeping voltage signal is sent to the $x+$ or $x-$ electrodes, and y_{PSD} is collected. The frequency of the first resonance peak ω_{r_1}, may be identified from the data. Alternatively, the collected data may be displayed to the user to interactively select the point of the first resonance peak. Thereafter, the probe is brought into contact with the sample and then retracted until the contact is broke. Using this data, estimate of the sensitivity between y_{PSD} and V_z (DC gain), can be computed as the ratio of y_{PSD} to V_z data around the contact point. In addition, the pull-off point y_{po}, and the noise in y_{PSD} while in-contact y_n, can be found. A ramp input with a saturated amplitude can be used to excite the scanner. The duration of the ramp t_r, should be chosen to be lower by a factor of 3 to 4 than the response time of the scanner, e.g. $t_r > \frac{4}{\omega r_1(Hz)}$. The nominal contact point is chosen to aloow a good SNR, while not loosing contact with the sample during the experiment. This can be accomplished by selecting the set-point y_s as

$$y_s = y_{po} + \frac{SNR\, y_n}{\text{expected \% of creep}} \tag{5.1}$$

where typical values for creep percentage is 10 to 30 %. The SNR can be chosen as desired, typically > 5. The amplitude of the amplitude-saturated ramp is then given by

$$\Delta V_z = \frac{|y_s - y_{po}|}{DCgain} \tag{5.2}$$

The probe is brought back into contact with the sample at the desired set-point and maintained by feedback. After several minutes, the instrument drift should be estimated from the control voltage signal. Based on that the time duration over which creep data is collected can be decided on such that instrument drift is only a small fraction of scanner creep.

Based on the presented compensation results, a 4th to 6th order model would be sufficient. For the selected order, standard input-output identification techniques [96], could be used to fit the data to the model. The resulting fit may require further fine tuning of the parameters. An interactive window showing th experimental and simulated responses can be displayed to the user, as in Figure 4-28. Poles and zeros can be displayed for the users as tuning knobs. The regions of the response where each pole and zero contribute most to the response could be labeled on the response window. The user can then fine tune the model fit to make both the simulated and experimental data in agreement. This procedure needs to be performed infrequently. Typically once or twice a year depending on how often the AFM is used.

For X and Y, a different experiment is needed for collecting creep data. For the X-axis, while the cantilever is in Air and the laser is aligned as in Figure 5-9, an amplitude-saturated ramp signal is applied to both electrodes $x+$ and $x-$, and the PSD signal is collected. To avoid possible nonlinearities in the PSD response, the input amplitude should be kept small. The SNR would still be good, since the PSD would be able to detect scanner bending $\sim 1\mathring{A}$ RMS. Data for the Y-axis creep could be obtained similarly, however, the laser spot would be aligned at the base of a rectangular cantilever as shown in Figure 5-9.

5.2.4 Open Loop vs. Closed Loop

We have shown one method to compensate for scanner creep when operated, as it is commonly, without measuring scanner displacement. An inverse filter can provide an inexpensive method of compensation. However, its performance will strongly depend on the quality of creep data, the order of the filter, and fitting algorithm. Obtaining reliable creep data for long time proved to be a difficult task especially for the common AFM user. In

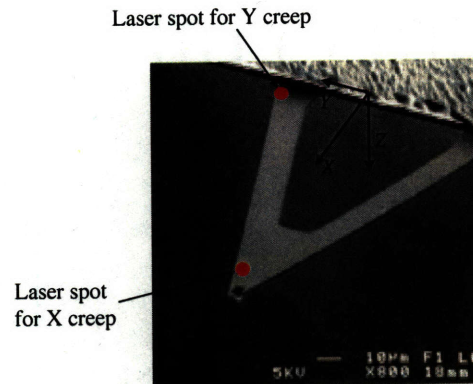

Figure 5-9: Locations for laser spot alignment for X and Y creep identification.

addition, the order of the model would grow if good short and long time compensation is desired. Another compensation alternative is to sense the scanner displacement in the Z-direction and use that signal to create the sample image. This would virtually remove the effect of creep on the image. Many displacement sensing technologies, e.g. capacitive, inductive, optical, can provide short term stability of $100\,ppm/^oC$. For a $5\,\mu m$ scanner like the one used in this study and a temperature change of 1^oC during experiments, a sensor drift of $5\,\AA$ is expected. These results are superior and more reliable than the results of the filter. However, this option is far more expensive. In addition, most sensors do not have large dynamic range at high bandwidth. As a result noise performance is worse than open loop operation especially for small scans or when scanning samples with small features (few nanometers).

5.3 Summary

In this chapter the LTI creep model of Equation (2.75) was inverted and used to compensate for scanner creep in the Z direction. Experimental results showing AFM images of 530 and $1590\,nm$ Silicon steps were presented to demonstrate the effectiveness of the compensation. Moreover, methods for generating creep data for scanner displacement in the X Y and Z directions were presented. Furthermore, identification procedure for model parameters was discussed. Finally, open versus closed loop operation was discussed.

Chapter 6

Automatic Selection of Scan and Controller Parameters

6.1 Introduction

In this chapter, the models and results presented in the earlier chapters will be used to aid in selecting scan and controller parameters. First, factors affecting scan parameter selection will be discussed. Then, performance trade-offs and limitations of the AFM feedback system will be identified and analyzed. Parameter selection will then follow for different control strategies.

6.2 On Factors Affecting Scan Parameter Selection

Several scan parameters are available to be freely specified by the user. These parameters include scan size, scan rate, image resolution (number of data points per scan line), force set-point, and controller gains. Scan size and resolution depend on the sample being imaged, hence, their values should be completely decided on by the user. The objective is to be able to automatically select scan rate (or speed), force set-point, and controller parameters in order to consistently achieve a *good* image. Characteristics of achieving a good image include, that probe and sample remain in- contact during scanning, that the set-point error is maintained small at all times, and the signal used to create the image is free

from mode oscillations. In addition, high-frequency noise level in the image signal should not be amplified by feedback. The latter requirement is less stringent in this application, because feedback stability will dictate a considerable limit on the bandwidth. In order to synthesize simple yet realistic rules for automatically selecting parameters, few simplifying assumptions are required. First, the requirements on scan speed will be addressed followed by a discussion on selection of the contact force set-point.

During scanning, the probe is dragged along the sample surface while in contact. Assuming negligible probe-sample deformations, the vertical speed of the probe v_z, is related to its constant lateral scan speed v_{scan}, by the local slope given by $tan(\alpha)$ at the probe-sample contact point ($\frac{\Delta z}{\Delta x}$ or $\frac{\Delta z}{\Delta y}$ depending on scan direction). This can be seen from Figure 6-1, where v_z is given by

$$v_z = \frac{v_{scan}}{tan(\alpha)} \tag{6.1}$$

A lower bound on the slope is given using the included angle of the probe α_p, as seen in Figure 6-1. The assumption of neglecting contact deformations may be reasonable if the controller manages to keep the set-point error small at all times. Alternatively, if the ratio between contact to cantilever stiffnesses is high, the assumption might be reasonable. Cantilevers used for imaging have resonance frequencies much higher than those of the scanner bending modes; 10 to 90 kHz compared to 300 Hz to 5 kHz for scanner resonances. Hence the feedback bandwidth is typically much lower than the cantilever resonance frequency, therefore neglecting the cantilever (probe) response is very reasonable, as implicitly implied by Equation (6.1). In the case of multiple contact points between the sample and the probe, v_z will depend on the smaller of the slopes at the contact points. Also in reality the probe, especially long sharp ones, could flex and cause the cantilever to twist, which has also been neglected.

The choice of contact force is motivated by four main factors, namely, contact stresses, sample deformation, lateral friction force between the probe and the sample, in addition to maintaining probe-sample contact during scanning. Using the model of section 2.2.1, the force required to theoretically achieve zero deformation between the probe and sample was

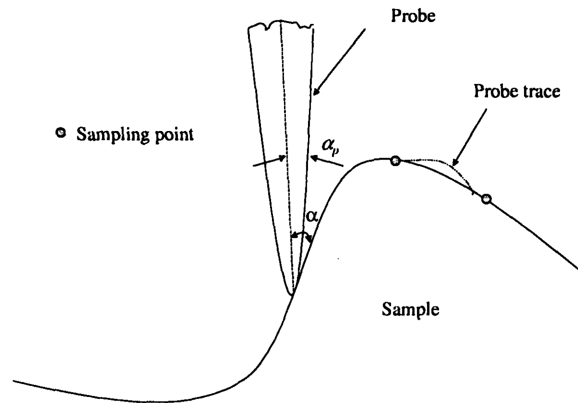

Figure 6-1: Dependance of probe vertical speed on local slope at contact point.

computed. The ratio between the zero-deformation force and the pull-off force is plotted versus λ in Figure 6-2. It is seen that except for very hard contacts ($\lambda < 0.1$), the force ratio is about 0.89. This implies that in order to achieve zero sample deformation, the force set-point would be such that the cantilever is pulling the probe away from the sample. This condition demands that during scanning, the set-point error be maintained very small at all times. Consequently, requiring a high-bandwidth typically beyond the system's mechanical resonances, and hence is impractical. On the other hand, the set-point should be chosen to minimize the friction force between the probe and the sample. In [74], experiments on mica have shown that in the absence of wear, the average friction force is directly proportional to contact area. The contact area is non-zero as long as the probe and sample remain in contact. Hence, there is no set-point which will make the friction force zero. However, the larger the contact force the greater the contact area, Figure 6-3, and the higher the friction force will be. Accordingly, a small contact force is desired. The minimum contact area for a stable contact will also depend on the cantilever stiffness.

Based on the above arguments, it is seen that the contact force should be selected as small as possible. The maximum achievable feedback bandwidth should then be identified for that particular set-point. The scan speed should be chosen to be smaller or equal to the maximum value for which contact is maintained at all times during scanning. The maximum feedback bandwidth will depend on the structure of the controller. Therefore,

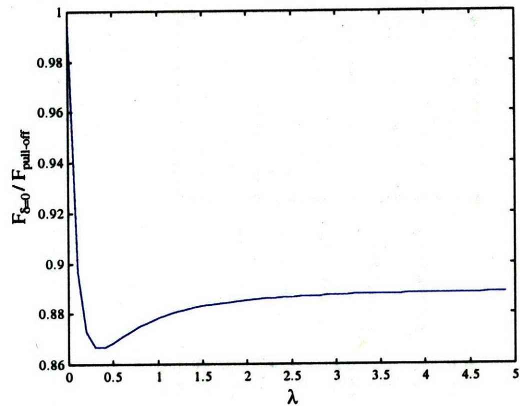

Figure 6-2: Ratio of zero-deformation force to pull-off force vs. λ.

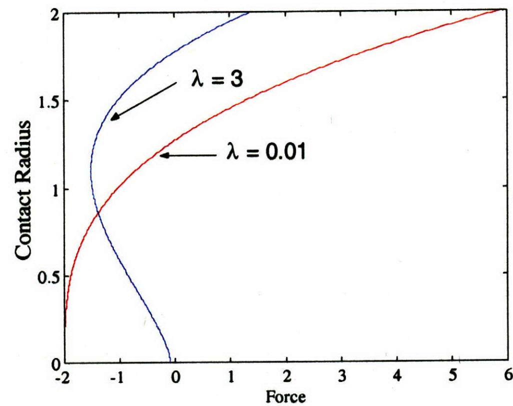

Figure 6-3: Contact radius vs. contact force for different values of λ.

the following sections will discuss different control strategies.

6.3 Trade-offs and Performance Limitations in AFM Feedback System

When the probe is brought into contact with the sample, the controller should achieve closed loop stability at the desired contact force set-point for the given cantilever and sample. Moreover, the controller should maintain the set-point error within a prescribed tolerance for all times (i.e. transient and steady state), such that probe-sample contact is not lost nor excessive force is applied to the sample. In addition, system uncertanties due to cantilever and sample properties, variations in contact stiffness an dissipation, and pole-

zero flipping, should all be compensated for. In addition, good dynamic response should be achieved in despite of these uncertainties. From a practical point of view, it would desired that controller have integral action to avoid needing excessively high-gain to maintain the desired set-point in addition to be able to reject constant disturbances. Furthermore, the controller should be based only on output measurement (PSD output). In addition, the controller should compensate for resonances within the desired closed loop bandwidth.

Before addressing the question of how to automatically select key parameters, it is essential first to identify expected performance trade-offs and limitations. We will begin by analyzing the linear model of the fast dynamics ignoring creep and hysteresis. In this section, the controller is assumed to be LTI. A block diagram of the feedback system is shown in Figure 6-4, where d_o is output disturbance, n is sensor noise, $G_c(s)$ is the controller transfer function, and $G_p(s)$ is the plant transfer function including driving amplifier, scanner, and sensor filter dynamics. A typical frequency response of G_p is shown in Figure 6-5. As discussed previously, the dynamics of the typical cantilevers are much faster than scanner lateral dynamics and therefore are neglected. Accordingly, sample topography maybe be modeled as an output disturbance d_o. The image is typically created from the input voltages (u_x, u_y, u_z). Therefore, the transfer functions between d_o and e (sensitivity function $S(s)$), and between d_o and u (control sensitivity function $S_u(s)$), are the main interest and are given by

$$S(s) = \frac{e}{d_o} = \frac{-1}{1+L(s)} \tag{6.2}$$

$$S_u(s) = \frac{u}{d_o} = \frac{-G_c}{1+L(s)} \tag{6.3}$$

$$L(s) = G_p(s)G_c(s)$$

Nominal feedback performance may therefore be specified in terms of Equations (6.2) and (6.3).

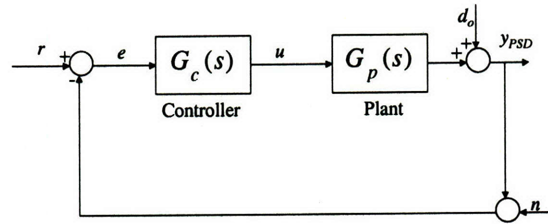

Figure 6-4: Block diagram of the AFM feedback system.

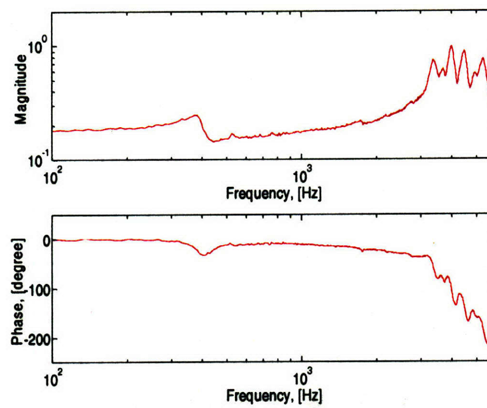

Figure 6-5: Representative frequency response of G_p.

6.3.1 Scanner Bending Modes

The results of Section 4.6 have demonstrated the coupling between the longitudinal and bending dynamics. In addition, the bending modes were found to be observable from the output signal. The frequency of the first bending mode is usually significantly lower than the first longitudinal mode; $380\,Hz$ and $4.6\,KHz$ for the AFM in use. As a result, a substantial reduction in feedback bandwidth is expected as a result of this coupling. Moreover, the poles and zeros of the bending modes will impose additional performance limitations, as will be shown in Section 6.3.3.

Further, when the scanner is commanded to move up/down, there will be a slight bending motion that gets detected by the PSD. The scanner is typically calibrated by imaging a standard of known height usually in the $100\,nm$ range. During imaging, the PSD signal will change due to the sample topography as well as actuator bending. Imagining a sample of a different height will result in a slightly different calibration factor, even if the nonlinearity of the scanner is not a concern. The change in calibration due to scanner bending would typically be less than $1\,\%$.

6.3.2 Uncertainty

In Chapter 4, experiments and simulations have revealed several sources of uncertainties including, changes in the resonance peak, contact stiffness and dissipation, transfer function DC gain, and the pole-zero structure. These changes were found to be a strong function of force set-point and disturbance amplitude. In addition, they may depend nonlinearly on probe-sample contact properties. The large level variations and uncertainties would have a strong impact on robust stability and performance. In order to demonstrate these points, consider a reduced-order model consisting of the first bending mode and its zero pair as the plant. As mentioned previously, the frequencies of the scanner resonances are not affected by the probe sample interactions. Based on this simple model, uncertainty in DC gain, modal damping, and pole-zero flipping can be modeled as an unstructured uncertainty as

follows

$$\begin{aligned} \frac{b_2 s^2 + b_1 s + b_0}{s^2 + a_1 s + a_0} &= \frac{\hat{b}_2 s^2 + \hat{b}_1 s + \hat{b}_0}{s^2 + \hat{a}_1 s + a_0} + \frac{\tilde{b}_2 s^2 + \tilde{b}_1 s + \tilde{b}_0}{s^2 + \tilde{a}_1 s + a_0} \\ G_p(s) &= \hat{G}_p(s) + W(s)\Delta(s) && (6.4) \\ \mid \Delta \mid &< 1 && (6.5) \end{aligned}$$

where $\hat{}$ represents estimate values and $\tilde{}$ represents deviation from the true value. Robust stability requires that

$$\mid W S_u \mid \leq 1 \qquad (6.6)$$

It is worth noting that this stability test is not conservative in the case of pole-zero flipping since the phase may change by a total of 360°. Equation (6.6), implies that at frequencies where uncertainties are large $|W|$ is large, $|S_u|$ should be made small for robust stability. Large variations and uncertainties would generally result in trading-off bandwidth (performance) to guarantee robust stability. This point will be demonstrated using the experimental frequency responses of Figures 4-17 and 4-19. The two responses were obtained for the same disturbance input amplitude but for two different force set-points, namely, 36 and $113\,nN$. An integral controller $G_c(s) = \frac{k_i}{s}$ is used and the resulting loop transfer function is shown in Figure 6-6. The controller gain was chosen to achieve a crossover frequency of $93\,Hz$ and $112\,Hz$ for the $36\,nN$ and $113\,nN$ data, respectively.

Figure 6-7, shows the control sensitivity function S_u for both force set-points. For the smaller force, pole-zero flipping occurs resulting in a very large peak close to the frequency of the bending mode. As a result, poor robustness properties and performance is expected; despite a relatively low bandwidth compared to the open loop bending resonance at $380\,Hz$. In addition, the sensitivity function, depicted in Figure 6-8, similarly shows a large peak. It is worth mentioning that the effect of an output disturbance at the frequency of the peak will be amplified more by S compared to S_u as seen by the magnitude of the peaks in their response. Therefore, the expected oscillations will be large in the output signal,which may be damaging to the probe and the sample. An image taken under these conditions would show oscillation if the probe would be perturbed during scanning. This is demonstrated in

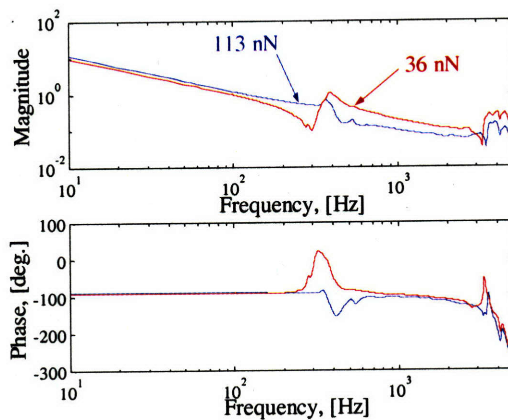

Figure 6-6: Loop transfer function frequency response of experimental data with integral control.

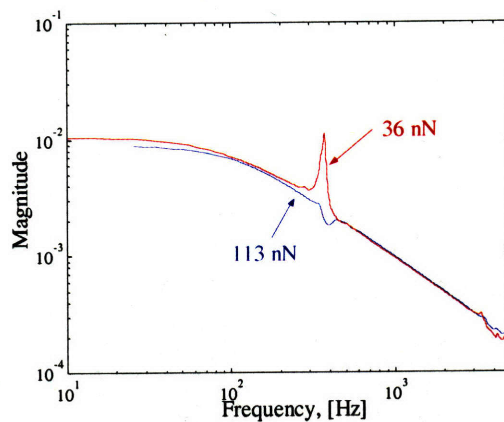

Figure 6-7: Control sensitivity function frequency response of experimental data with integral control.

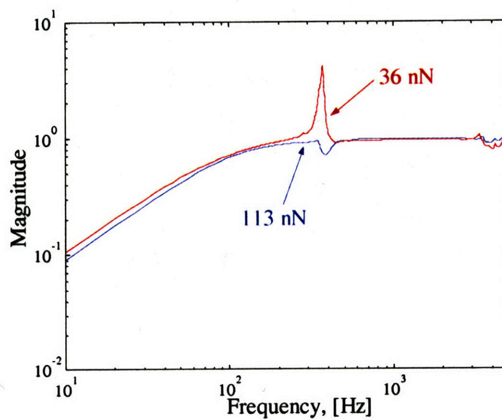

Figure 6-8: Sensitivity function frequency response of experimental data with integral control.

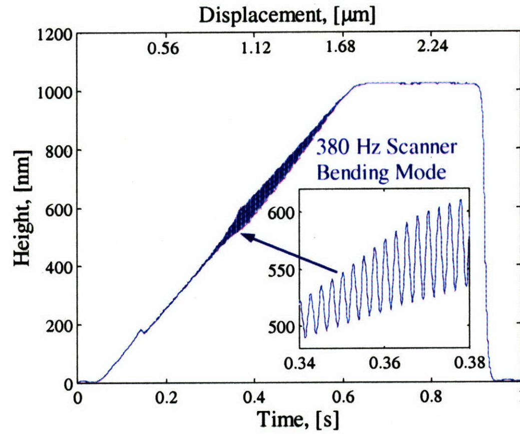

Figure 6-9: Oscillations due to scanner bending mode in experimental AFM image of a 1046 nm Silicon step.

Figure 6-9, where an experimental AFM image of a 1046 nm step is shown. A small force helps reduce probe-sample friction, sample deformation hence, image distortion. However, it may dictate a small bandwidth in order to eliminate oscillations in the image, therefore, trading off bandwidth (performance) for robustness.

6.3.3 Poles and Zeros of a Transfer Function

Fundamental limitations in feedback control systems have been studied since the early work of Bode [98] and Horowitz [99]. A recent review on this topic is available in [97, 101]. It is fairly known that adding zeros to a transfer function can increase overshoot in the step response. The presence of zeros, more formally, may impose a fundamental limitation on the achievable performance. The results of [101] will be used and later expanded on to show that zeros impose a trade-off between response time and overshoot.

Consider a stable proper single-input single-output (SISO), transfer function $G(s)$ with at least one zero at $s = -s_z$, $s_z > 0$. Furthermore, assume that all the poles of $G(s)$ have real parts less than $-s_z$. Then the unit step response of $G(s)$ satisfies the following integral constraint

$$\int_0^\infty e^{s_z t}\, e(t)\, dt \quad = \quad \frac{-G(0)}{s_z} \tag{6.7}$$

where $e(t)$ is the output error defined as the difference between the output and its steady state value due to a unit step response. Equation (6.7), results from the application of the Laplace transform to the error signal $E(s) = G(0) - G(s)$, and noting that $G(s_z) = 0$. For a complex zero-pair at $s_z = -\sigma_z \pm j\omega_z$, $\sigma_z, \omega_z > 0$, Equation (6.7), leads to

$$\int_0^\infty e^{\sigma_z t}\cos(\omega_z t)\, e(t)\, dt = \frac{-\sigma_z G(0)}{\sigma_z^2 + \omega_z^2} \tag{6.8}$$

$$\int_0^\infty e^{\sigma_z t}\sin(\omega_z t)\, e(t)\, dt = \frac{\omega_z G(0)}{\sigma_z^2 + \omega_z^2} \tag{6.9}$$

To demonstrate how these integrals constitute a constraint on performance, consider a plant with a single real zero at $s = -s_z$ and assume that for $t > t_s$ $e(t) \approx 0$ and that $s_z t_s \ll \frac{\pi}{2}$. Furthermore, all the poles of $G(s)$ have real parts that $\ll -s_z$, then Equation (6.7) reduces to

$$\int_0^{t_s} e^{s_z t}\, e(t)\, dt + \int_{t_s}^\infty e^{s_z t}\, e(t)\, dt = \frac{-G(0)}{s_z} \tag{6.10}$$

$$\int_0^{t_s} e(t)\, dt \simeq \frac{-G(0)}{s_z} \tag{6.11}$$

where it has been assumed that the contribution of the second integrand in Equation (6.10), is negligible compared to that of the first integrand under the aforementioned assumptions. If $G(0) > 0$, then the initial error is positive, and decays exponentially to zero. From Equation (6.11), it is seen that the integral of the error amounts to a negative value. Hence, the error signal changes sign and the output signal will overshoot. A similar argument holds for $G(0) < 0$. In addition, Equation (6.11) suggests that $\| e \|_\infty > \frac{-G(0)}{s_z t_s}$, hence a large overshoot would occur as the response time t_s is made small compared to the frequency of the zero s_z. No rigorous reasoning was given for neglecting the contribution from the second integrand in Equation (6.10). However, the argument was presented to demonstrate the trade-off due to system zeros. It also demonstrates that if the system response was allowed to be slow compared to the zeros, the trade-off is relaxed.

Furthermore, consider the step response of a system with a complex zero pair at $0.7 \pm j0.7$ and three real poles all at $s = -\lambda$. Three cases are considered for λ equal to 1, 2 and 3. The

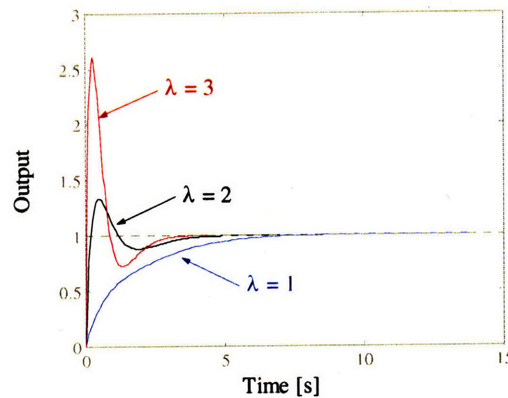

Figure 6-10: Step response of three transfer functions with a complex zero-pair .

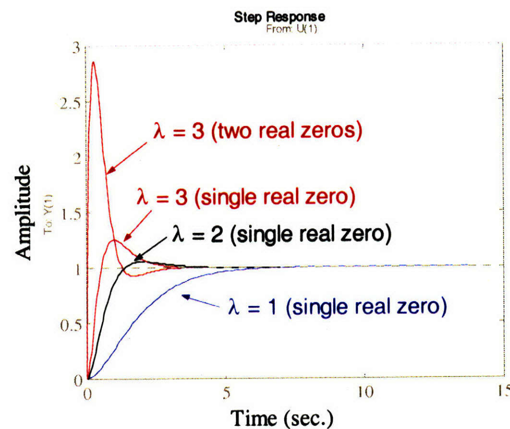

Figure 6-11: Step response of three transfer functions with a single real pole demonstrating trade-off.

response is shown in Figure 6-10, where it is seen that as the response time is made faster compared to the frequency of the zeros, large overshoot is observed in the step response. Another system was also consider which has a single real zero at $s = -1$ and again three real poles all at $s = -\lambda$. The case of $\lambda = 3$ was simulated and compared to the previous system with the two complex zeros. The result is depicted in Figure 6-11. It is seen that trade-off exist, however, the amount of overshoot is smaller for the case with a single pole. The number of zeros is found to have more effect on the amount of overshoot rather than the complex or real nature of the zeros. Thus, a fundamental trade-off between response time and overshoot exists due to transfer function zeros.

The structure of the feedback system imposes additional constraints. The values of $S(s)$ and the complementary sensitivity function $T(s)$, are constrained at the frequencies of the plant poles s_{p_i} and zeros s_{z_i}. At these frequencies, $S(s)$ and $S_u(s)$ are given by

$$S(s_{p_i}) = 0 \quad (6.12)$$

$$S(s_{z_i}) = 1 \quad (6.13)$$

$$S_u(s_{p_i}) = 0 \quad (6.14)$$

$$S_u(s_{z_i}) = G_c(s_{z_i}) \quad (6.15)$$

The response of the output error $E(s)$, and the control signal $U(s)$, to the reference signal $R(s)$ and the output disturbance $D_o(s)$ are governed by $S(s)$ and $S_u(s)$, respectively. By applying the constraint of Equation (6.7), to $S(s)$ and $S_u(s)$, the response of the output error and the control signal to a unit step in reference or a negative unit step in output disturbance are found to satisfy the following Equations

For an open loop pole at $s = -s_p$

$$\int_0^\infty e^{s_p t}\, e(t)\, dt = \frac{-S(0)}{s_p} \quad (6.16)$$

$$\int_0^\infty e^{s_p t}\, [u_o - u(t)]\, dt = \frac{-S_u(0)}{s_p} \quad (6.17)$$

For an open loop zero at $s = -s_z$

$$\int_0^\infty e^{s_z t}\, e(t)\, dt = \frac{-[S(0) - 1]}{s_z} \quad (6.18)$$

$$\int_0^\infty e^{s_z t}\, [u_o - u(t)]\, dt = \frac{-[S_u(0) - G_c(s_z)]}{s_z} \quad (6.19)$$

where s_p and s_z could be real or complex, and u_o is the steady state value of the control signal to the unit step input. Following similar arguments to the ones presented earlier, the open loop poles and zeros impose a trade-off between overshoot and response time at

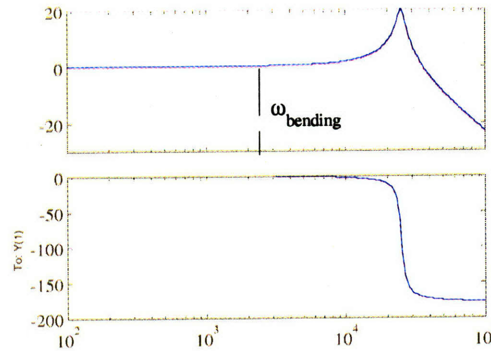

Figure 6-12: Simulated frequency response between input voltage V_z, and the scanner's vertical displacement z_p.

different degrees of severity.

For the AFM feedback system it is seen that the poles of the 1st bending mode will appear as zeros for the sensitivity function $S(s)$, and $S_u(s)$ provided that they are not canceled by zeros in the controller. Hence, for any LTI controller, extending the bandwidth beyond the first mode will result in overshoot in tracking step-like samples in both output and voltage (image signal), responses. Attempts to cancel the bending mode by controller zeros might lead to poor robustness due to the high-level of uncertainty in the system and may lead to closed loop instability. Moreover, even if exact cancellation was possible, the bending mode poles will remain zeros of $S_u(s)$ but not $S(s)$. Hence, the limitation would remain for the input signal (image signal). Another option is to create the image from a measurement of the scanner vertical displacement z_p by fitting the AFM with a displacement sensor. The transfer function between input voltage V_z and z_p is shown in Figure 6-12. Hence, overshoot and oscillations in the control voltage with frequencies close to that of the bending mode, will pass unfiltered, and z_p response will have same characteristics as the input voltage.

The open loop zeros of the AFM, as seen from Equation (6.18), will also impose a similar trade-off on the output error response. If the frequencies of the slowest open loop pole and zero are relatively close, then Equation (6.18) would yield a more stringent constraint

compared to Equation (6.16). Moreover, open loop zeros impose an additional limitation on the achievable performance in terms of the control signal response (image signal). Many model-based control methodologies including fixed linear control, and adaptive control, will attempt to cancel the plant dynamics and introduce favorable dynamics as higher performance is demanded from the closed loop system. If the controller introduces poles to cancel the open loop zeros, these controller poles will appear as poles of the control sensitivity function $S_u(s)$. Consequently, these lightly damped poles will make the response oscillatory having poor transients with response time not faster than that of the zeros. The material presented in this section applies to single-degree of freedom feedback configuration. It is possible to alleviate these trade-offs using a two-degree of freedom design. This approach may permit shaping the response of a measured input (e.g. reference signal or a measured disturbance), however, it would not be possible with unmeasured disturbances. Therefore, the performance of the AFM feedback system will be constrained with the aforementioned trade-offs.

6.4 Performance of PID and Higher Order LTI Controllers

As discussed in Section 6.3.3, substantial increase in the feedback bandwidth beyond the first resonance will result in overshoot and poor time response. As had been shown from experiments and simulations, the frequency response of the AFM is that of a relative degree zero transfer function. This is a reasonable approximation over frequencies below to the second resonance. In order to reduce the effect of high-frequency modes on feedback stability and performance, the relative degree of the loop transfer function should be made one or higher by the controller. Commercial AFM use a PID controller . Due to the aforementioned high-frequency roll-off constraint, in addition to the constraints of Section 6.3.3, a PID controller does not provide any advantage over a simple integral controller. To show this consider the open loop experimental frequency response of Figure 4-18 of the $113\,nN$ set-point. A PID controller with zeros at $400\,Hz$ only 5% from the actual resonance was used. In addition, a single pole was added to make the transfer function of the controller proper

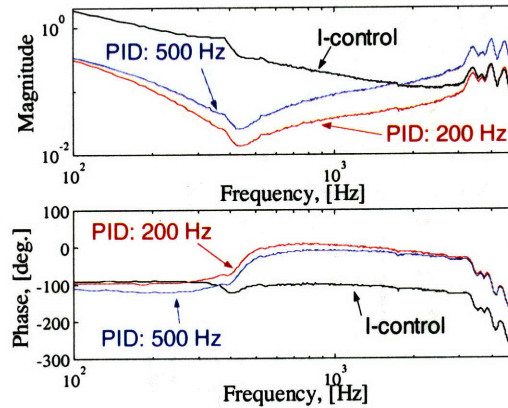

Figure 6-13: Loop transfer function frequency response with integral control and proper PID controller.

for real-time implementation. The PID controller transfer function is given by

$$G_c(s) = \frac{b_{c_2}s^2 + b_{c_1}s + b_{c0}}{s(s + a_{c0})} \tag{6.20}$$

Figure 6-13, compares the frequency response of the loop transfer function for both integral and the above proper PID controller. For the PID controller two cases are shown, one with a pole at a lower frequency than the resonance frequency (at $200\,Hz$), while in the other case the pole frequency is higher (at $500\,Hz$). It is seen that in order to meet the high-frequency roll-off constraint, the crossover frequency for both PID controllers is about $30\,Hz$, while for integral control it is $200\,Hz$. Hence, a PID would trade-off bandwidth in order to meet the high-frequency modes constraint. In addition, a standard improper PID controller would achieve an even smaller bandwidth.

The aforementioned limitations are true for any LTI controller. With higher-order fixed controllers, only marginal increase in bandwidth may be obtained compared to an I-controller, if the overshoot constraint is to be avoided. In addition, with the higher order controller, the feedback loop may become more sensitive to the large system uncertainties.

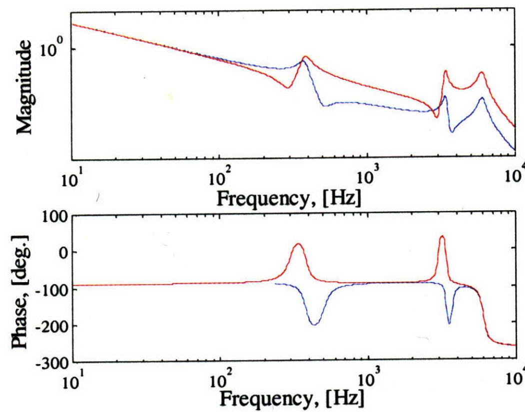

Figure 6-14: Loop transfer function frequency response with integral control.

6.5 Integral Controller

A simple integral controller can be used to stabilize the AFM feedback loop, provided that the crossover frequency is chosen either lower than the first resonance frequency, or between the first and second resonance frequencies where the phase is close to zero degrees, as seen from Figure 6-14. Although having a crossover frequency between the first and the second resonances may yield nominal closed loop stability, the resulting closed loop system will have poor robustness properties because of the large resonance peak in the frequency response and possible pole-zero flipping. This can be seen from Figures 6-15 and 6-17, for the two possible pole-zero structures. In addition, the feedback system would have poor transient performance due to oscillations in the step response, Figures 6-16 and 6-18. Accordingly, to achieve robust stability, and oscillation-free response, one needs to sacrifices bandwidth by selecting the crossover lower than the first resonance. Commonly, an integral action in the controller is not used on its own but complemented with a proportional term to form a PI controller. The reason behind this, is that for a system with a relative degree two, using an integral controller will result in increasing the relative degree to become 3, which leads to high-gain instability as seen in Figure 6-19 (a). However, the AFM model of Equation (6.4), has a relative degree zero. Hence, as seen in Figure 6-19 (b), the AFM feedback system with integral control would remain stable at high-gain, within the region where this model is valid.

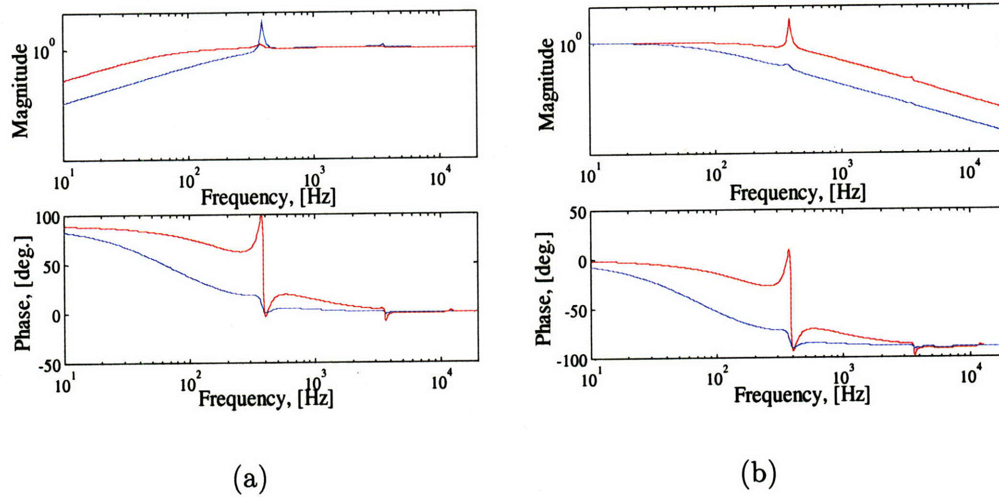

Figure 6-15: Frequency response with integral control: (a) sensitivity function (d_o to y_{PSD}), (b) control sensitivity function (d_o to u), (red) high bandwidth (blue) low bandwidth.

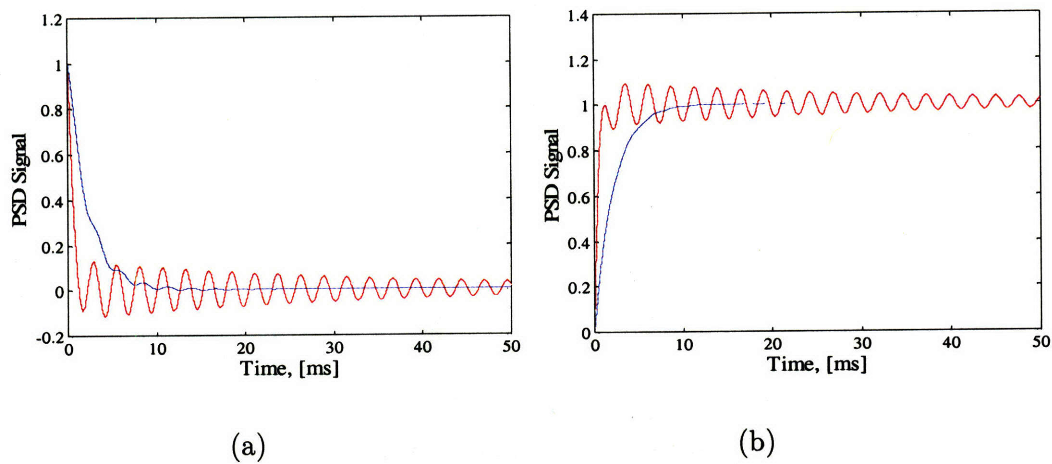

Figure 6-16: Unit step response in d_o with integral control: (a) sensitivity function (d_o to y_{PSD}), (b) control sensitivity function (d_o to u), (red) high bandwidth (blue) low bandwidth.

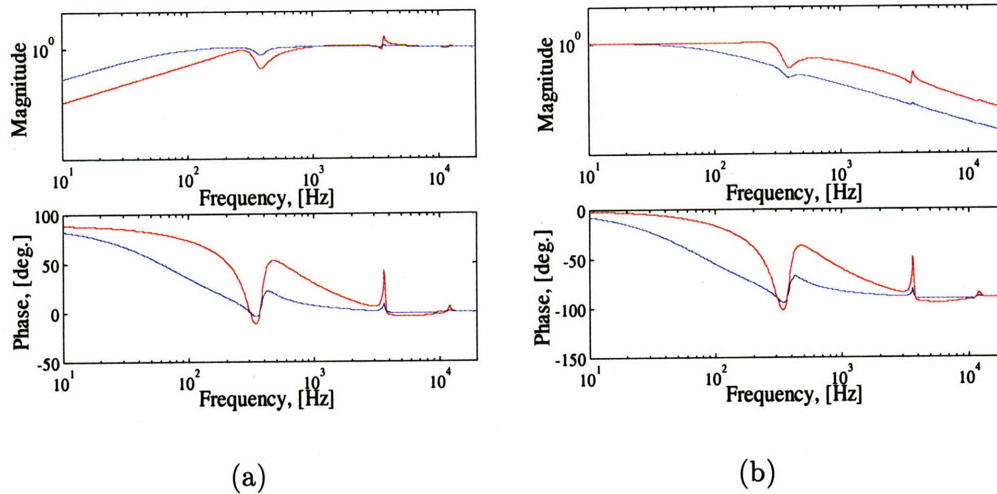

(a) (b)

Figure 6-17: Frequency response with integral control: (a) sensitivity function (d_o to y_{PSD}), (b) control sensitivity function (d_o to u), (red) high bandwidth (blue) low bandwidth.

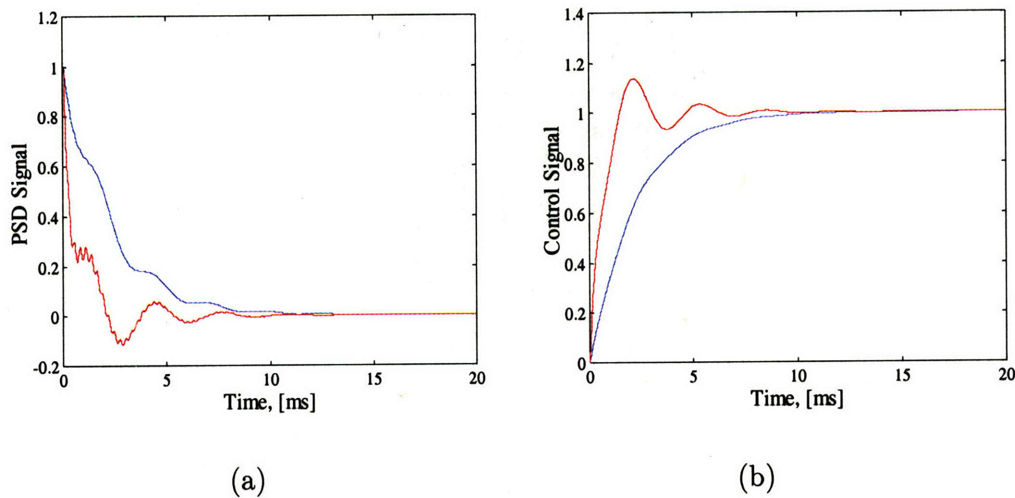

(a) (b)

Figure 6-18: Unit step response in d_o with integral control: (left) sensitivity function (d_o to y_{PSD}), (right) control sensitivity function (d_o to u), (red) high bandwidth (blue) low bandwidth.

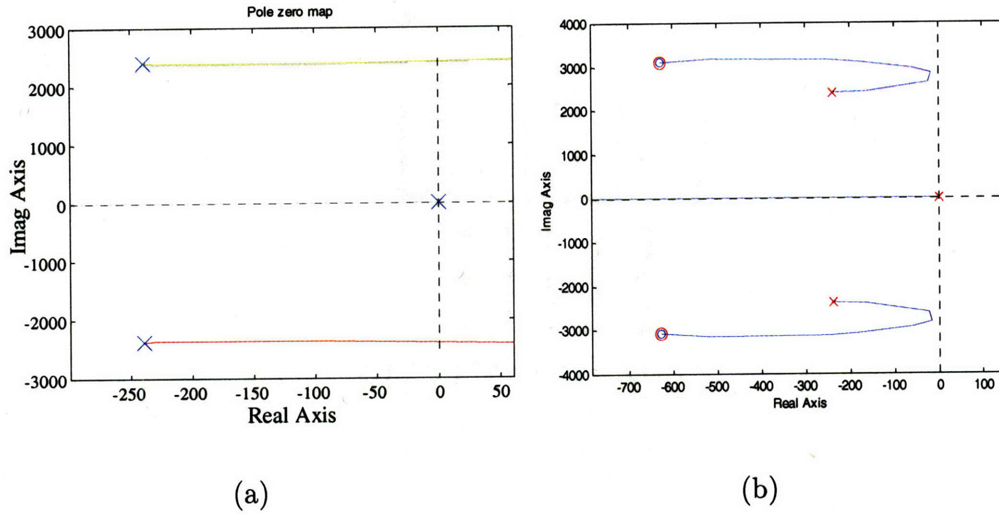

Figure 6-19: Root locus using an integral controller with (a) $G_p(s) = \frac{1}{(\frac{s}{2\pi 380})^2+\frac{0.2s}{2\pi 380}+1}$, (b) $G_p(s) = \frac{(\frac{s}{2\pi 500})^2+\frac{0.4s}{2\pi 500}+1}{(\frac{s}{2\pi 380})^2+\frac{0.2s}{2\pi 380}+1}$.

Based on the previous discussion, the design of the AFM feedback system can performed by imposing specifications on S_u, since it represents the response of the signal the image is created from. In addition, if an AFM is equipped with scanner vertical displacement sensor, the response of z_p will be very similar to V_z for the reason discussed earlier (Section 6.3.3, and Figure 6-12). The performance specification on S_u will be chosen such that the bandwidth as defined by $-3\,dB$ frequency be maximum such that the magnitude of $|S_u(j\omega)| < \delta/(DCgain)$ for $\omega \geq \omega_o$, where δ is design constant. The condition on $|S_u(j\omega)|$ is to ensure that there are no large peaks in the frequency response. Closing the feedback loop with the I-controller, the poles of the first mode will tend to the system zeros at high gain. If there are peaks in the $|S_u(j\omega)|$ it would be at frequencies between the open loop poles to and the zeros. Hence, ω_o should be set as the smaller of the resonance or zeros' frequency. From experiments and simulations $\delta \leq 0.4$ seems to give good results.

As seen from Figure 6-7, limiting the bandwidth to be below the resonance by a factor of 2 or 3 will not necessarily guarantee good performance, rather it will strongly depend on the contact force set-point. Therefore, the feedback bandwidth may be improved for a given set-point by estimating the frequency response function (FRF) to obtain $\hat{G}_p(j\omega)$ around that set-point. The procedure for estimating $\hat{G}_p(j\omega)$ starts as follows, while the

cantilever is away from the sample and in Air, excite the scanner in bending along the axis of the cantilever (X-axis in Figure 4-7) and collect the PSD signal. This can be done by for example using a frequency sweeping input signal, the range of frequencies can be as low as 10 Hz and up to few kilohertz. From the data estimate resonance frequency and resonance peak. These values may be stored and this step of the procedure need not be repeated before each scan. It may be left as part of the AFM calibration procedure, typically performed few times a year depending on how often the instrument is used.

Then the scanner moves the probe closer to the sample until it is in contact and zero contact force is achieved. The probe is then retracted until contact is broken. The PSD signal is collected. An estimate for DC gain (V_z to y_{PSD}) around zero-force point, the cantilever deflection at pull-off, output noise at zero-force point both peak-to-peak and RMS can all be estimated from the collected data.

The probe is to be brought into contact at the desired set-point. While in contact and in open loop, a perturbation voltage signal V_z is sent to the scanner. The signal should be rich enough to excite first resonance and dose not cause loss of contact. In addition, a good signal-to-noise ratio should be obtained. For example, if a frequency sweep is used, then the estimate of resonance peak in Air, in-contact DC gain, and pull-off can be used to select the amplitude of the input voltage such that the probe remains in contact during this test.

The collected input output data can be used with standard spectral methods [96], to compute the auto and cross corelation functions and use them to estimate the FRF. The estimate of the DC gain obtained for the FRF may be corrected using the estimate from the pull-off experiment. In addition, an estimate for the frequency of the zeros ω_{z_1}, can be found. The FRF estimate could be displayed to the user and the user may identify the frequency of the zeros. The FRF can be used to create $S_u(j\omega)$.

The controller gain k_i can be found as follows

1. Define the maximum $-3\,dB$ bandwidth of $S_u(s)$ as the frequency of the bending

mode ωr_1, as motivated by the constraints of Section 6.3.3. The gain to achieve this is $k_{i_r} = \frac{\omega r_1}{DCgain}$.

2. Initialize two vectors k_y and k_n, where the former vector will contain tested values of k_i that satisfies the performance specification, and k_{in} are used to store tested value of k_i that does not. Initialize first entries e.g. $k_{1y} = \frac{\omega r_1}{20\,DC\,gain}$ and $k_{1n} = \frac{20\,\omega r_1}{DC\,gain}$.

3. Use an initial guess for k_i (for example $k_{1n} = \frac{\omega r_1}{3\,DCgain}$), and compute $S_u(j\omega)$ and find ω_{-3dB}.

4. Check if $|S_u(j\omega)| < \frac{\delta}{DCgain}$ for $\omega > \omega_o$, where $\omega_o = min(\omega_{z_1}, \omega_{r_1})$, and $\delta < 1$.

5. If condition is satisfied store the used value of k_i into the vector k_{iy} and choose a higher value of k_i to repeat the test to check if performance objective will be met with the new value of k_i. The method of bisection could be used to find the new value of k_i by taking it as the average between the highest value in k_{iy} and k_{i_r}.

6. If condition in step 4 is not satisfied store the used value of k_i into the vector k_{in}. Choose a lower value in a similar manner as step 5.

7. The procedure should be stopped when the error (either relative or absolute) between the last two values of ω_{-3dB} satisfying the constraint are smaller than a prescribed value.

8. During the procedure it should be checked that the computed ω_{-3dB} that meet the performance specification are not larger than ω_{r_1}.

The value of k_i can then be used to find the maximum scan speed v_{scan} such that contact is maintained at all time. As had been previously discussed, while the probe is in contact with the sample, the fastest output disturbance seen by the feedback system is approximated by a ramp with a slope of $k_{ramp} = \frac{v_{scan}\,DCgain}{tan(\alpha_p)}$. As a result the maximum

output error due to this ramp input may be found as

$$G_p(s) = \frac{b_2 s^2 + b_1 s + b_0}{s^2 + a_1 s + a_0}, \quad G_c(s) = \frac{k_i}{s} \tag{6.21}$$

$$S(s) = \frac{s(s^2 + a_1 s + a_0)}{s(s^2 + a_1 s + a_0) + k_i(b_2 s^2 + b_1 s + b_0)} \tag{6.22}$$

$$e_{ss} = \lim_{s \to 0} s \frac{k_{ramp}}{s^2} S(s) = k_{ramp} \frac{a_0}{k_i b_0} \tag{6.23}$$

$$|y_s - y_{po}| = e_{ss} = \frac{k_{ramp}}{k_i k_{z_p/V_z}} = \frac{v_{scan}\, DCgain}{tan(\alpha_p) k_i k_{z_p/V_z}} \tag{6.24}$$

$$v_{scan_{max}} = \frac{|y_s - y_{po}|\, tan(\alpha_p)\, k_i\, k_{z_p/V_z}}{DCgain} \tag{6.25}$$

where, k_{z_p/V_z} is the scanner linear displacement sensitivity in the Z direction i.e. calibration factor. The value of α_p is given available in specification sheets of commercial AFM cantilevers which could be entered by the user. If not, then a value for the sharpest available cantilever may be used which is about 20°.

The computed value for the maximum scan speed is such that probe-sample contact is not lost, but does not guarantee a low set-point error. It is also possible to estimate the scan speed needed to track the minimum sample feature that could be detected by the probe. Hence, as seen in Figure 6-20, an estimate may be obtained by setting the scan speed such that the probe moves laterally a distance of $4\, R_p$ within the response time of the scanner $\frac{1}{\omega_{r_1}\,(Hz)}$, hence, the maximum $v_{scan_{max}}$ is given by

$$v_{scan_{max}} = 4 R_p \omega_{r_1}\,(Hz) \tag{6.26}$$

Then for the selected set-point, the scan speed may be chosen between both limits. In Sections 6.7 and 6.6, two methods will be presented to further improve image quality. It is possible that if $v_{sacn_{max}} \leq v_{scan_{min}}$ or some other minimum value set by the user that set-point be increased by the ratio of $\frac{v_{scan_{min}}}{v_{scan}}$ and the whole procedure is repeated to find the controller gain and scan speed range. It is also possible to test different set-points and give speed and scan times for each case.

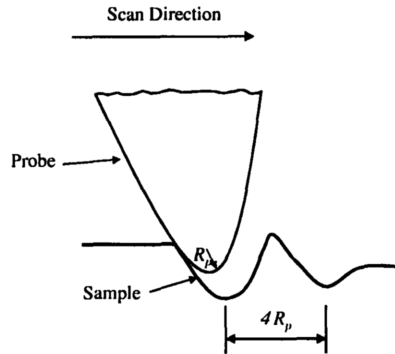

Figure 6-20: Schematic of probe sliding on sample.

In the above procedure, the initial choice for the set-point was the zero contact force point. As discussed in Section 6.2, it is desired to use the smallest force that is practically possible. The absolute minimum value for a set-point will be limited by the output signal noise close to the pull-off point, in order for the contact not to be broken. In addition, if the pull-off point is found to be too close to zero-force point, then a larger set-point may be used as an initial guess. The initial guess should be at least a factor of 2 or 3 of the peak-to-peak output signal noise.

If the perturbation signal is chosen appropriately, its effect on sample deformation or damage should be minimal. Typically, the output noise is $< 1\,\mathring{A}$, hence for a SNR of say 6 and a typical resonance peak of 2 to 3 the maximum displacement of the cantilever would be $< 1\,nm$ typical, which is smaller than tracking error involved with PID controller used in Commercial AFMs. In addition, because of the low stiffness of cantilevers used in contact-mode operation ($\sim 0.1\,N/m$), the resulting force will be small ($\sim 1\,nN$). Other operating modes like the intermittent-mode use stiff cantilevers driven at high frequencies (100 to $500\,kHz$) with typical oscillation amplitudes of 20 to $100\,nm$. The resulting tapping force [14], will at be $\sim 10s\ nN$. Hence, the effect of the perturbation signal on the sample should generally be acceptable.

As seen from Chapter 4, the in-contact frequency response depends on input amplitude and set-point. Therefore, the performance of the feedback system would depend on how good the estimate of G_p is. In the above parameter selection procedure, the parameters were chosen such that the controller would be able to keep the output error small. Hence, the system is expected to behave closer to the estimated dynamics. In addition, possible errors in $\hat{G}_p$ would affect the performance and achievable bandwidth. However, since small amplitudes were to be used in estimating G_p, the resulting estimate will typically underestimate modal damping compared to high amplitude signals. This may be seen from results of Chapter 4, where dissipation is often seen to be amplitude dependant. As a result, the procedure is expected to yield results that are on the conservative side. In addition, uncertainties in estimating frequency response, pull-off force, and DC gain may be compensated for by choosing a small value for δ. The advantages of this procedure of automatically selecting scan and controller parameters, compared to the trial and error method usually employed will be demonstrated by experimental results which will be shown shortly. Without this procedure a mere change in the set-point may result in closed loop oscillation or instability, damage to sample. In addition, with trial and error, the user would spend considerable time in tuning parameters and the resulting image may not be close to the true sample. Furthermore, if the cantilever is changed or a new sample is to be imaged the user would typically need to find new scan parameter using trial and error.

When choosing an input for perturbing the system, several factors have to be considered, including, its spectrum, amplitude, SNR, spectral leakage, and time required for the experiment. Since the range of frequencies of interest is known a priori, in addition to typical noise floor of the instrument, the input signal can be generated off-line, while allowing some of its characteristics (e.g. amplitude), to be scaled or modified based on the SNR of the particular test according to the cantilever and sample, and environment. There are many input signals that can be used, three types have been tested, namely, swept sine, chirp, and bandwidth-limited white noise. Each has its advantages and disadvantages. Stepped sine does not suffer from spectral leakage but requires a large time to complete the experiment and may require a more elaborate software for running the experiment with the AFM hard-

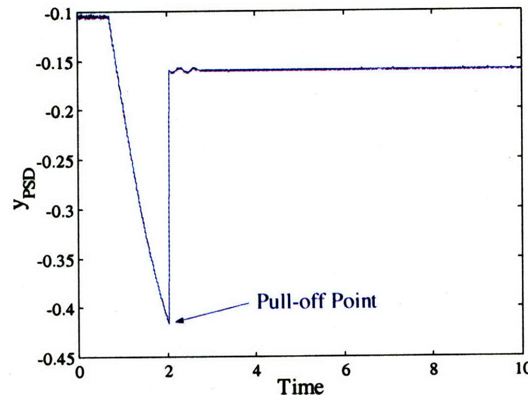

Figure 6-21: Force vs. scanner displacement: identifying DC gain, pull-off point, and in-contact output signal noise.

ware. Chirp signal, on the other hand, provides a smaller measurement time compared to swept sine but may have low SNR at frequencies of the system zeros. In addition, spectral lines other those of interest may appear due to nonlinear effects and they can not be separated. Finally, filtered white noise can be generated with a desired spectrum through a proper filter. Drawbacks include the need for a frequency window to reduce spectral leakage and large number of averaging of results. The three signals were used and experiments showed that with SNR > 6 good results were obtained. With random noise averaging of 20 to 30 yielded good consistent results. Experience from FFT-based signal analyzers can be used. In addition, the fact that the structure of the system to be identified in known a priori in the frequency range of interest should be used in designing the perturbation signal.

The proposed procedure was tested experimentally and the results are shown in Figures 6-21 to 6-23. The data in Figure 6-21 gives estimates for the DC gain of $0.3\,V/V$, $y_{po} \approx -0.42\,V$, noise of $5\,mV$ peak-to-peak. A bandwidth-limited white noise of intensity of 10^{-10} and a bandwidth of $20\,kHz$ was used to perturb the system. Using Welch's averaged periodogram method [96], an estimate of $\hat{G}_p$ was obtained giving $\omega_{z_1} \approx 420\,Hz$. These estimates were used in the proposed controller gain selection procedure to yield $k_i = 4600$ and $\omega_{-3dB} \approx 115\,Hz$ for a value of $\delta = 0.4$. The resulting estimates for the closed loop sensitivity and control sensitivity functions are given in Figure 6-22. Based on Equations

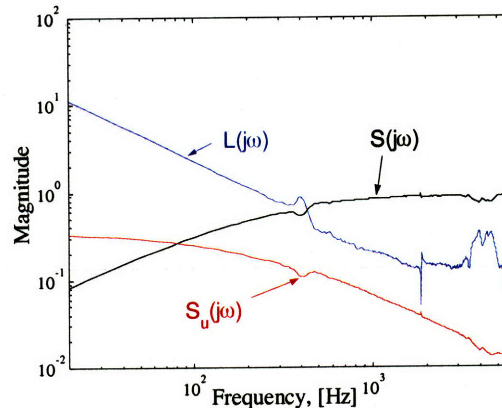

Figure 6-22: Estimate of $|\hat{L}(j\omega)|$, $|\hat{S}(j\omega)|$, and $|\hat{S}_u(j\omega)|$ using Welch's averaged periodogram method.

(6.26) and (6.25), the range for the scan speed is $9.2\mu m/s$ to $307\mu m/s$. The wide range of the possible scan speeds raises the question of what value to use. In Sections 6.6 and 6.7 two options will be given to address this question.

To compare the performance of the I-controller with the proposed tuning procedure with the PID controller used with commercial AFMs, a set of Silicon steps were imaged with a scan area of $10 \times 10\,\mu m^2$. The PID controller gains, scan rate, and force set-point were set at the AFM manufacturer recommended values of 150 for the proportional and integral gains, 50 for the derivative gain, $4\,Hz$ for the scan rate and $1.7\,muN$ for the force set-point. The force set-point for the I-controller was set to zero and the scan rate to $2\,Hz$. The resulting images are shown in Figure 6-23 (a) and (b) for the PID and I controller, respectively. As clearly seen from the figures, the I-controller provides a more accurate image of the steps while using a substantially smaller contact force and hence reducing the probe-sample friction force. As a result, more details on the sample surface quality can be observed while reducing the possibility of sample and probe damage and wear. One main parameter governing how well the image closely resembles the true sample shape is the ratio of feedback response time to the time over which sample topography changes. The latter is governed by the scan speed or scan rate for a given scan size. A ratio smaller than one would be desired. Since the default value for scan rate used with the PID controller is

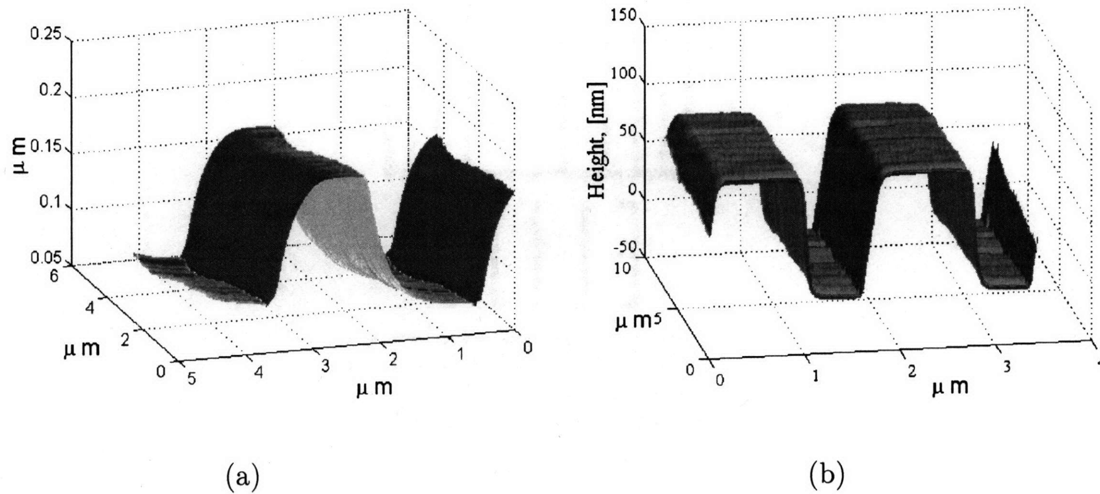

(a) (b)

Figure 6-23: AFM images of Silicon steps: (a) PID controller with default parameter values, (b) I-controller using proposed tuning method.

twice that used for the I-controller, using a smaller scan rate would improve the accuracy of the image collected with the PID controller. However, as discussed in Section 6.4 the I-controller can achieve a higher feedback bandwidth than the PID controller, therefore, a much smaller scan rate compared to that used with the I-controller will be required with the PID controller to resolve the sample shape accurately.

6.6 Feedforward Compensation

In the previous section, a procedure for automatically selecting scan and controller parameters was presented. The procedure yielded a range of possible scan speeds. Choosing speeds close to the minimum of the range would yield smaller set-point error, however would require longer scan time. Choosing the speed closer to the maximum allowable value would yield the opposite result. In this section, it is suggested that an intermediate value be used. In addition, a feedforward term is added to the controller to help reduce the set-point error. The feedforward term is based on the control signal used in the first pass along the scan line (the trace line). This voltage would be applied as the probe is dragged along the retraces line. A block diagram representation is shown in Figure 6-24. It is important to note that because the feedforward term does not depend on a real-time signal during the retrace

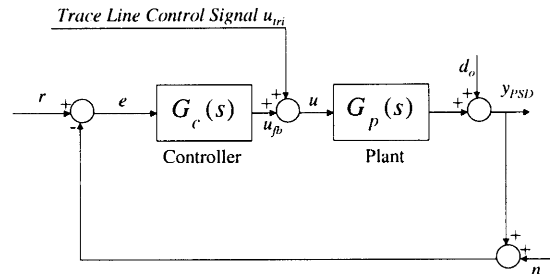

Figure 6-24: AFM feedback block digram with a feedforward term.

period, this term will not affect feedback stability. However, this method would be most effective under two main conditions. The first is that the scan and controller parameters values are selected such that the feedback system response is well behaved. This would be expected by using the procedure of Section 6.5. For example, consider a condition where the feedback response is oscillatory, and is used to image a step. As the probe climbs the step along the trace line, oscillations are expected to occur at the top of the step. During the retrace, the oscillations are expected to occur at the bottom of the step. Therefore, if the trace signal was used as feedforward signal for the retrace line, large errors in the final image may result. Hence, if scan and controller parameters are not selected to give a good dynamics response and image is quite different than the sample, then the feedforward term will not be effective. The second condition is that the distance in the slow scan direction between the trace and retrace lines is small compared to the probe seize, e.g. $\leq 2R_p$ (typically $R_p \sim 20\,nm$). This is typically not a problem especially with new AFM where the maximum number of scan lines is 1000 to 4000, over a scan range of 40 to $100\,\mu m$.

6.7 Variable Scan Speed Scanning

The trade-off between scan speed and scan time motivates devising a procedure for varying the scan speed as needed. The use of this procedure is not necessarily limited to I-control. Conventionally, a triangular wave is applied to the so-called fast scan direction, while a slow ramp signal is applied to the so-called slow scan direction. The resulting probe trace

along the sample surface is depicted in Figure 6-25. The scan speed is therefore, given by the frequency of the triangular wave (scan rate), and the scan size. The new proposed scan voltage signals are shown in Figure 6-26, along with the resulting probe trajectory. While the input to the slow scan direction is held constant, the first half of a triangular wave is applied to move the probe along the trace line. The scan speed used can be selected as an intermediate value of the scan range found from the procedure of Section 6.5 for I-control, or an initial value specified by the user. At the end of the trace line, the probe is maintained at that position for a very short time period $\Delta t_1 \sim$ one or two sampling periods (10 to $20\,\mu s$, typically). During this brief period, a new scan speed is computed based on the output error signal from the trace line. The speed could be either increased or decreased accordingly. The slope of the retrace line (return line) would be based on this new scan speed. At the end of the retrace line, the probe is held for another period of Δt_2, and the scanner is commanded to move in the slow scan direction a distance equal to the scan size divided by the number of scan lines (image resolution), as specified by the user. The choice of Δt_2 should be based on the bending resonance frequency which has been identified as in Section 6.5, e.g. $\Delta t_2 > \frac{4}{w_{r_1}(Hz)}$. The procedure is repeated. The scan speed used for the following trace line could be either as the one of the first trace line or as the one of the last retrace line. It can be seen that with this scan voltages the probe will trace the same line twice in comparison to the conventional scan trajectory, hence, using the proposed feedforward compensation of Section 6.6 could be combined with the variable scan speed for further improvement is image accuracy and reduced transient contact and friction forces.

The increase in scan time due to the new trajectory compared to the conventional one will depend on the scan speeds of each line. However if the scan speed was initially selected appropriately such than no change in the speed was needed, then the relative increase in scan time would be given by

$$t_{conv} = \frac{image\ resolution}{scan\,rate} \tag{6.27}$$

$$t_{new} = (image\ resolution)\,\Delta t_1 + (image\ resolution - 1)\,\Delta t_2 + \frac{image\ resolution}{scan\,rate} \tag{6.28}$$

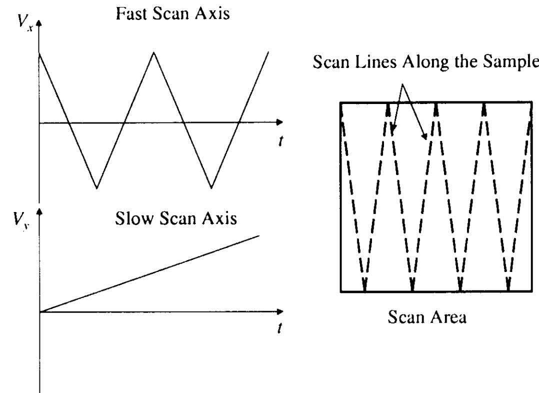

Figure 6-25: Conventional scan voltage signals and resulting probe trace.

$$\frac{t_{conv}}{t_{new}} = 1 + (scan\,rate)\,(\Delta t_1 + \Delta t_2) \tag{6.29}$$

The increase in scan time, under these conditions, would be $< 2\%$ of a typical scan time of $3\,minutes$. Moreover, the variable scan speed may yield reduced scan time in addition to improved image details. However, due to scanner creep, the voltage applied to the slow scan speed may result in increased creep response in the slow scan direction due to the ladder-like shape of the voltage signal compared to the conventional ramp signal. Therefore, unless creep compensation is employed, this procedure may not be appropriate. However, if creep compensation is employed for the lateral directions, then the resulting creep is expected to yield good results. This scan trajectory would be ideal if closed loop is employed for the lateral scan direction using additional scanner displacement sensors. One may imagine varying the scan speed along the same line but the complexity in generating reference scan trajectories that would not result in exciting the scanner lateral dynamics would probably over weigh any expected reduction in scan time.

Different criteria may possibly be used to modify the trace-line scan speed based on the retrace-line data. One possible algorithm is as follows

While in-contact and just before scanning starts, collect the output error data and compute the in-contact RMS ($e_{RMS}(0)$), peak-to-peak output noise $n_{e_{pp}}$, in addition to an estimate of the DC gain. Using the trace line data, find the maximum error e_{max}, the

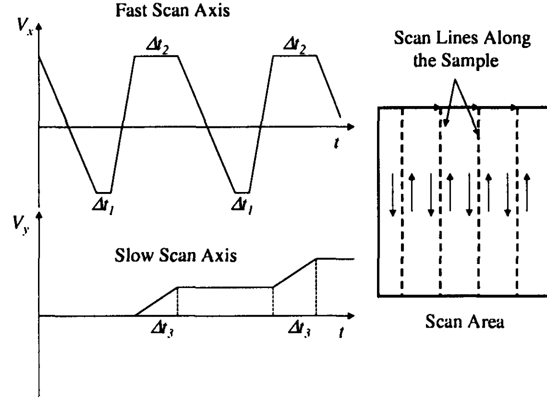

Figure 6-26: New proposed scan voltage signals and resulting probe trace.

corresponding input voltage $V_z(e_{max})$, and the minimum voltage along the line $V_{z_{min}}$. The latter value represents the reference point for sample height along that scan line.

Check if $|e_{max}-e_{RMS}(0)|$ is within the output noise level, e.g. check if $|e_{max}-e_{RMS}(0)| < \frac{n_{e_{pp}}}{2}$.

If the conditions satisfied then the maximum set-point error is small and no change in the scan speed is needed. If the condition is not satisfied then the scan speed can be changed based on the percentage of output error relative to measured sample height at the point of maximum output error. The new scan speed can be found by doing the following

check if $|V_z(e_{max}) - V_{z_{min}}| \times DC\,gain < n_{e_{pp}}$, i.e. is the point of maximum error has

if not then use $v_{scan_{rtc}} = \frac{\beta_1\, DCgain\, |V_z(e_{max})-V_{z_{min}}|}{|e_{max}-e_{RMS}(0)|}\, v_{scan_{trc}}$, where $\beta_1 > 0$ and is the percentage of acceptable dynamic error, e.g. $< 10\%$.

if yes then the new scan speed $v_{scan_{rtc}}$ can be given in terms of the trace speed $v_{scan_{trc}}$ as $v_{scan_{rtc}} = \frac{\beta_2\, n_{e_{pp}}}{2\,|e_{max}-e_{RMS}(0)|}\, v_{scan_{trc}}$, i.e. dynamic error compared to the output noise, $\beta_1 \geq 1$.

6.8 Robust Adaptive Output Control

It has been shown that in-contact AFM dynamics can vary dramatically depending on the choice of scan parameters, and sample and cantilever properties. The large level of uncertainties in the AFM dynamics invites more advanced control methodologies to be used in order to compensate for uncertainties and improve performance. The careful modeling and analysis of the AFM dynamics presented in the previous chapters provides valuable information that should be used by the controller to maximize possible gains in performance. The aforementioned work has identified the correct model structure in addition to various sources of uncertainties. Commonly in control, there are two methods for handling uncertainties. If the uncertainty can be parameterized appropriately, adaptation may be used to compensate for these parametric uncertainties. When the uncertainties are bounded but their structure is unknown or too complicated to model, robust control can be used to handle these types of uncertainties and disturbances. For the AFM, both types of uncertainties are present and a robust adaptive controller will be designed to handle them.

The controller to be designed is to be based only on output measurement, y_{PSD} and have both adaptive and robust parts to compensate for parametric and time-varying bounded uncertainties and disturbances. Moreover, it is desired that the controller have integration action in order to maintain the desired set-point and reject constant disturbances without needing excessively high gain. A mechanism for avoiding integrator anti-wind up is also desired for a practical implementation. In addition, the dynamic order of the controller should be kept as low as possible, and have a minimum number of design parameters. A systematic method for choosing these design parameters is desired and parameters should ultimately be related to scan parameters' selection. Furthermore, some degree of tuning for transient performance would be advantageous.

The field of adaptive control is very rich with various control algorithms. These algorithms vary in their complexity, and the class of systems and uncertainties they can be applied to. However, adaptive control is hardly used in practice. This is mainly due to the complexity and high-order of typical adaptive controllers. In addition, no systematic

procedures are available for to relating controller parameters to feedback performance. The proposed controller which will be presented, is based on several main results in the literature. The references will be appropriately cited in the presentation. However, several simplifications were made to ensure a practically viable controller, while achieving improved performance over a fixed controller.

In the absence of a rigid body mode (double integrator in a transfer function model), mechanical structures in many cases can be modeled as zero relative degree transfer function, over the frequency range of interest. As a result, the derivative of the physical control signal would be required in order to synthesize the adaptive control signal. This difficulty was circumvented by augmenting a ficticious first order low-pass filter with the plant model. The resulting design model will have a relative degree of one. A ficticious control signal u, is then synthesized and passed through the filter to obtain the physical control signal V. Alternatively, an integrator could have been augmented with the plant model. The ficticious control signal would then be required to stabilize the integrator in addition to the original plant model. However, the filter dynamics are known, which would simplify selecting controller parameters. In addition, the filter bandwidth can be selected to reduce the effect of unmodeled dynamics and sensor noise by filtering high-frequency components from the control signal. As discussed previously, the sample topography may be modeled as an output disturbance. In addition, disturbance at the plant input may arise from actuator nonlinearities and hysteresis. Therefore, both types of disturbances are included in the model. The plant model considered for controller design is therefore, given as

$$y = \frac{b_n s^n + b_{n-1}s^{n-1} + \ldots + b_0}{s^n + a_{n-1}s^{n-1} + \ldots + a_0}V, \quad V = \frac{p}{s+p}u \tag{6.30}$$

$$y = \frac{b'_n s^n + b'_{n-1}s^{n-1} \ldots + b'_0}{s^{n+1} + a'_{n-1}s^n + \ldots + a'_0}u + d_o + \sum_j \frac{r'_{q_j}s^{q+1} + r'_{q-1_j}s^q + \ldots + r'_{q0_j}}{s^{n+1} + a'_{n-1}s^n + \ldots + a'_0}d_{i_j} \tag{6.31}$$

where, $q \leq n-1$. Equation (6.31), can be written is state space form as,

$$\begin{aligned}
\dot{x}_1 &= x_2 - a'_{n-1}x_1 + b'_n u \\
\dot{x}_2 &= x_3 - a'_{n-2}x_1 + b'_{n-1}u
\end{aligned}$$

$$\vdots \tag{6.32}$$

$$\dot{x}_{n-q} = x_{n-q+1} - a'_q x_1 + b'_{q+1} u + \sum_j r'_{q_j} d_{i_j}$$

$$\vdots \tag{6.33}$$

$$\dot{x}_n = -a'_o x_1 + b'_o u + \sum_j r'_{o_j} d_{i_j}$$

$$y = x_1 + d_o$$

$$\dot{\mathbf{x}} = \mathbf{A}\mathbf{x} - \mathbf{a}' x_1 + \mathbf{b}' u + \sum_j \mathbf{r_j}\, d_{i_j} \tag{6.34}$$

$$\dot{\mathbf{x}} = \mathbf{A}\mathbf{x} - \mathbf{a}' y + \mathbf{b}' u + \mathbf{a}' d_o + \sum_j \mathbf{r_j}\, d_{i_j} \tag{6.35}$$

$$\mathbf{A} = \begin{bmatrix} 0 & \dots \\ \vdots & I_{n-1} \end{bmatrix} \tag{6.36}$$

where d_o is output disturbance, d_{i_j} is the jth input disturbance, $\mathbf{r_j}$ is vector of known constant parameters, and $\mathbf{a}'$ and $\mathbf{b}'$ are vectors of unknown constant parameters. The main assumptions involved are

A.1 The plant is minimum phase, i.e. $\mathbf{b}'(\mathbf{s})$ is Hurwitz.

A.2 The sign of the high-frequency gain, $sgn(b'_n)$ is known and is positive.

A.3 Plant order n is known and plant relative degree is 1, else a first order filter is augmented with the plant model.

A.4 Bounds on the uncertain parameters and disturbances are known.

Since only output measurements are available, an observer needs to be designed to estimate the unmeasured states. The so-called K-filters [63], will be used for this task. Equation (6.35), can be rewritten as

$$\dot{\mathbf{x}} = \mathbf{A}\mathbf{x} + \mathbf{F}(y,u)^T \mathbf{\Theta} + \mathbf{a}' d_o + \sum_j \mathbf{r_j}'\, d_{i_j} \tag{6.37}$$

$$\mathbf{F}(y,u)^T = [\mathbf{I}_{m+1} u, -\mathbf{I}_n y] \tag{6.38}$$

$$\mathbf{\Theta} = [\mathbf{b}', \mathbf{a}']^T \tag{6.39}$$

Now consider an observer of the form

$$\dot{\hat{\mathbf{x}}} = \mathbf{A}\hat{\mathbf{x}} + \mathbf{F}(y,u)^T\mathbf{\Theta} + \mathbf{k}(y - \mathbf{e_1}^T\hat{\mathbf{x}}) \tag{6.40}$$

where $\mathbf{e_1}$ is the standard basis vector in R^{n+1}, and $\mathbf{k} = [k_1, ..., k_n]^T$ such that $\mathbf{A_o} = \mathbf{A} - \mathbf{k}\mathbf{e_1}^T$ is Hurwitz, which implies that $\exists \, \mathbf{P}\,\mathbf{A_o} + \mathbf{A_o}^T\mathbf{P} = -\mathbf{I},\ \mathbf{P} = \mathbf{P}^T > 0$. However, Equation (6.40) involves the unknown parameter vector $\mathbf{\Theta}$, therefore, can not be directly used. Furthermore, consider the filters ξ and $\mathbf{\Omega}$ given by

$$\dot{\xi} = A_o\xi + \mathbf{k}y \tag{6.41}$$

$$\dot{\mathbf{\Omega}}^T = A_o\mathbf{\Omega}^T + \mathbf{F}(y,u)^T \tag{6.42}$$

The state estimation is given by $\hat{\mathbf{x}} = \xi + \mathbf{\Omega}^T\mathbf{\Theta}$. This may be seen by considering

$$\hat{\mathbf{x}} = \xi + \mathbf{\Omega}^T\mathbf{\Theta} \tag{6.43}$$

$$\dot{\hat{\mathbf{x}}} = \dot{\xi} + \dot{\mathbf{\Omega}}^T\mathbf{\Theta} \tag{6.44}$$

$$\dot{\hat{\mathbf{x}}} = \mathbf{A_o}\xi + \mathbf{k}y + \mathbf{A_o}\mathbf{\Omega}^T\mathbf{\Theta} + \mathbf{F}(y,u)^T\mathbf{\Theta} \tag{6.45}$$

$$= (\mathbf{A} - \mathbf{k}\mathbf{e_1}^T)(\xi + \mathbf{\Omega}^T\mathbf{\Theta}) + \mathbf{k}y + \mathbf{F}(y,u)^T\mathbf{\Theta} \tag{6.46}$$

$$= \mathbf{A}\hat{\mathbf{x}} + \mathbf{F}(y,u)^T\mathbf{\Theta} + \mathbf{k}(y - \mathbf{e_1}^T\hat{\mathbf{x}}) \tag{6.47}$$

The dynamics of estimation error $\varepsilon = \mathbf{x} - \hat{\mathbf{x}}$ are governed by

$$\dot{\varepsilon} = \mathbf{A_o}\varepsilon + (\mathbf{a}' - \mathbf{k})d_o + \sum_j \mathbf{r}'_{\mathbf{j}} d_{i_j} \tag{6.48}$$

Hence, ε are exponentially stable in the absence of disturbances. With assumption of bounded disturbances, the disturbed dynamics of ε are bounded but the bound is unknown.

Consider the columns of $\mathbf{\Omega}^T = [v_n, \dots, v_o, \Xi]$. The first $n+1$ columns are given by

$$\dot{v}_j = \mathbf{A_o} v_j + e_{n-j}\ ,\ j = 0, \dots, n \tag{6.49}$$

Also note that, $\mathbf{A_o}^j e_n = e_{n-j}, j = 0, \dots, n-1$. Therefore, the following filter can be used in addition to a single algebraic equation to evaluate v_j,

$$\dot{\lambda} = \mathbf{A_o}\lambda + \mathbf{e_n}\, u \tag{6.50}$$

$$v_j = \mathbf{A_o}^j \lambda,\ \ j = 0, \dots, n \tag{6.51}$$

Similarly, Ξ can be obtained from as follows

$$\dot{\eta} = \mathbf{A_o}\eta + \mathbf{e_n}\, y \tag{6.52}$$

$$\Xi = -[\mathbf{A_o}^{n-1}\eta, \dots, \mathbf{A_o}\eta, \eta] \tag{6.53}$$

Using the identity, $\mathbf{A_o}^n \mathbf{e_n} = -\mathbf{k}$, leads to $\xi = -\mathbf{A_o}^n \eta$.

Now that the observer filters are available, the controller design may be carried out. First define the output error $z_1 = y - y_s$. The output dynamics are given by

$$\dot{z}_1 = x_2 - a'_{n-1} y + b'_n\, u + \sum_j r'_{n_j}\, d_{i_j} + \dot{d}_o + a'_{n-1}\, d_o \tag{6.54}$$

$$\mathbf{x} = \xi + \Omega^T \mathbf{\Theta} + \varepsilon \tag{6.55}$$

$$x_2 = \xi_2 + \Omega_2^T \mathbf{\Theta} + \varepsilon_{x_2} \tag{6.56}$$

$$\dot{z}_1 = \xi_2 + \Omega_2^T \mathbf{\Theta} + \varepsilon_{x_2} - a'_{n-1} y + b'_n\, u + \sum_j r'_{n_j}\, d_{i_j} + \dot{d}_o + a'_{n-1}\, d_o \tag{6.57}$$

$$\dot{z}_1 = \xi_2 + \mathbf{\Theta}^T \Lambda + \varepsilon_{x_2} + b'_n\, u + D \tag{6.58}$$

where $\Lambda^T = \Omega_2^T + \mathbf{e_{n+2}}^T y$, and $D = \sum_j r'_{n_j}\, d_{i_j} + \dot{d}_o + a'_{n-1}\, d_o$. Define, $\tilde{\Theta} = \Theta - \hat{\Theta}$, $\varrho = \frac{1}{b_n}$,

$\tilde{\varrho} = \varrho - \hat{\varrho}$. Now consider the choice of control law u given by

$$u = (\hat{\varrho}\alpha_1 + \alpha_2) \tag{6.59}$$

and

$$b'_n\hat{\varrho}\alpha_1 = b'_n\hat{\varrho}\alpha_1 + \alpha_1 - \alpha_1 = \alpha_1 - \tilde{\varrho}b'_n\alpha_1 \tag{6.60}$$

Substituting the above control law into Equation (6.58), results in

$$\dot{z}_1 = \xi_2 + \mathbf{\Theta}^T\Lambda + \varepsilon_{x_2} + b'_n(\hat{\varrho}\alpha_1 + \alpha_2) + D \tag{6.61}$$

$$\dot{z}_1 = \xi_2 + \mathbf{\Theta}^T\Lambda + \varepsilon_{x_2} + \alpha_1 - b'_n\tilde{\varrho}\alpha_1 + b'_n\alpha_2 + D \tag{6.62}$$

Choosing α_1 as

$$\alpha_1 = -\xi_2 - \hat{\mathbf{\Theta}}^T\Lambda \tag{6.63}$$

$$\dot{z}_1 = \tilde{\mathbf{\Theta}}^T\Lambda + \varepsilon_{x_2} - b'_n\tilde{\varrho}\alpha_1 + b'_n\alpha_2 + D \tag{6.64}$$

In order to proof closed loop stability with the above control law consider the Lyapunov function candidate V_1 given by

$$V_1 = \frac{1}{2}z_1^2 \tag{6.65}$$

$$\dot{V}_1 = z_1[\tilde{\mathbf{\Theta}}^T\Lambda + \varepsilon_{x_2} - b'_n\tilde{\varrho}\alpha_1 + b'_n\alpha_2 + D] \tag{6.66}$$

Before completing the stability analysis the choice of adaptation law and robust control functions need to be addressed. For an adaptation law, parameter projection is used. There are several options [100] including continuous and discontinuous projection. The adaptation laws have to ensure the following two properties, namely

$$\tilde{\boldsymbol{\Theta}}^T[z_1\Lambda - \Gamma^{-1}\dot{\hat{\boldsymbol{\Theta}}}] \leq 0 \tag{6.67}$$

$$\hat{\boldsymbol{\Theta}}(t) \in \boldsymbol{\Pi} \tag{6.68}$$

where $\Gamma = \Gamma^T$ is a constant gain matrix. Equation (6.67) ensures that the adaptation law will render the Lyapunov function non-increasing. The following update law is used

$$\dot{\hat{\boldsymbol{\Theta}}} = Proj(\hat{\boldsymbol{\Theta}}, \Gamma z_1 \Lambda) \tag{6.69}$$

$$\dot{\hat{\varrho}} = -sgn(b_n')\gamma_\varrho z_1 \alpha_1 \tag{6.70}$$

$$Proj(\hat{\Theta}_i, \Gamma_i) = \begin{cases} 0 & \hat{\Theta}_i \leq \Theta_{i_{min}} \text{and}\, \gamma_{ii} z_1 \Gamma_i < 0 \\ 0 & \hat{\Theta}_i \geq \Theta_{i_{max}} \text{and}\, \gamma_{ii} z_1 \Gamma_i > 0 \\ \gamma_{ii} z_1 \Gamma_i & \text{otherwise} \end{cases} \tag{6.71}$$

where γ_i are constants.

Now α_2 could be chosen to ensure that $V_1 \leq 0$. α_2 is chosen to compensate for disturbances D, uncertain parameter estimation error, and state estimation error $\varepsilon_{x_{2_o}}$. The following form is chosen for α_2

$$\alpha_2 = -k_{z_1}/b_{n_{min}} z_1 + \alpha_{21} + \alpha_{22}, \quad k_{z_1} > 0 \tag{6.72}$$

Since bounds on uncertain parameters and disturbances are known we can choose α_{21} to satisfy the following two conditions

$$z_1(b_n'\alpha_{21} + \tilde{\boldsymbol{\Theta}}^T\Lambda - b_n' \, \tilde{\varrho}\alpha_1 + D) \leq \epsilon_1 \tag{6.73}$$

$$z_1\alpha_{21} < 0 \tag{6.74}$$

where $\epsilon_1 > 0$ is a design parameter. Equation (6.73) is used to bound the disturbances and uncertainties by a known function to enable controlling transient performance at all times. Equation (6.74) is used to ensure that when adaptation is on α_{21} is dissipative in nature so

V_1 will remain negative semidefinite. To handle ε_{x_2}, α_{22} is used and is chosen to satisfy the following condition

$$z_1(b'_n\alpha_{22} + \varepsilon_{x_2}) \leq \epsilon_2\varepsilon_{x_2}^2 \tag{6.75}$$

$$z_1\alpha_{22} < 0 \tag{6.76}$$

where $\epsilon_2 > 0$ is a design parameter, and ε_{x_2} is bounded (Equation (6.48)) , and assumption **A.4**), but unknown.

The stability analysis can know be completed. With the proper choice of α_{21} and α_{22}, Equation (6.66) reduces to

$$\dot{V}_1 \leq -k_{z_1}z_1^2 + \epsilon_1 + \epsilon_2\,\varepsilon_{x_2}^2 \tag{6.77}$$

$$\dot{V}_1 \leq -2k_{z_1}V_1 + \epsilon_1 + \epsilon_2\,\varepsilon_{x_2}^2 \tag{6.78}$$

$$V_1(t) \leq V_1(0)\,e^{-2k_{z_1}t} + \int_0^t e^{-2k_{z_1}(t-\tau)}(\epsilon_1 + \epsilon_2\,\varepsilon_{x_2}^2(t))d\tau \tag{6.79}$$

$$V_1(t) \leq V_1(0)\,e^{-2k_{z_1}t} + \frac{1}{2k_{z_1}}[1 - e^{-2k_{z_1}t}](\epsilon_1 + \epsilon_2 \parallel \varepsilon_{x_2} \parallel_{max}^2) \tag{6.80}$$

Hence, $z_1 = y - y_s$ is bounded. From Equation (6.48) ε is bounded and also $\boldsymbol{\Theta}$ is also bounded as a result of the adaptation law of Equations. (6.69) and (6.70). The boundedness of z_1 leads to boundedness of η, Equation (6.52). To prove the boundedness of λ consider the transfer function representation of Equation (6.50) given by

$$\lambda_i(s) = \frac{s^{i-1} + k_1 s^{i-2} + \ldots + k_{i-1}}{s^{n+1} + k_1 s^n + \ldots + k_{n+1}}\,u\,,\ i = 1, \ldots, n+1 \tag{6.81}$$

$$y = \frac{b'(s)}{a'(s)}\,u \tag{6.82}$$

$$\lambda_i(s) = \frac{(s^{i-1} + k_1 s^{i-2} + \ldots + k_{i-1})\,a'(s)}{(s^{n+1} + k_1 s^n + \ldots + k_{n+1})\,b'(s)}\,y\,,\ i = 1, \ldots, n+1 \tag{6.83}$$

Based on assumption **A.1**, λ_i , $i = 2, \ldots, n+1$ is also bounded. By referring to Equation (6.55) it is seen that the states $\mathbf{x}$ are also bounded. Finally, u is also bounded. Conse-

quently, the closed loop system is stable and all signals are bounded.

Now assume that the disturbances D are zero, and consider the following Lyapunov function candidate V, and its time derivative both given as

$$V = \frac{1}{2}z_1^2 + \frac{|b_n'|}{2\gamma_\varrho}\tilde{\varrho}^2 + \frac{1}{2}\tilde{\Theta}^T\Gamma^{-1}\tilde{\Theta} + \frac{\epsilon_2}{2}\varepsilon^T P\varepsilon \tag{6.84}$$

$$\begin{aligned}\dot{V} &= z_1[\tilde{\mathbf{\Theta}}^T\Lambda + \varepsilon_{x_2} - b_n'\,\tilde{\varrho}\alpha_1 + b_n\alpha_2] \\ &\quad -\frac{|b_n|}{\gamma_\varrho}\tilde{\varrho}\dot{\hat{\varrho}} - \tilde{\Theta}^T\Gamma^{-1}\dot{\hat{\Theta}} - \epsilon_2\varepsilon^T\varepsilon \end{aligned}\tag{6.85}$$

Substituting Equation (6.72) into Equation (6.85) leads to

$$\begin{aligned}\dot{V} \le\; & -k_{z_1}z_1^2 + \tilde{\mathbf{\Theta}}^T[z_1\Lambda - \Gamma^{-1}\dot{\hat{\mathbf{\Theta}}}] + \tilde{\varrho}b_n'[-z_1\alpha_1 - \frac{1}{\gamma_\varrho}\dot{\hat{\varrho}}] + b_n' z_1\alpha_{21} + z_1[\varepsilon_{x_2} + b_n'\alpha_{22}] \\ & -\epsilon_2\varepsilon^T\varepsilon \end{aligned}\tag{6.86}$$

The second and third terms on the right hand side of inequality (6.86) ≤ 0 using Equation (6.67) and (6.70), respectively. The fourth term < 0 from Equation (6.74) while the fifth term is $\le \epsilon_2\varepsilon_{x_2}^2$ from Equation (6.75). Hence, Equation (6.86) reduces to

$$\dot{V} \le -k_{z_1}z_1^2 + \epsilon_2\varepsilon_{x_2}^2 - \epsilon_2\varepsilon_{x_2}^2 - \epsilon_2 \sum_{i=1,3,4,\ldots,n} \varepsilon_i^2 \tag{6.87}$$

$$\dot{V} \le -k_{z_1}z_1^2 \tag{6.88}$$

Therefore, z_1 is bounded. By inspecting Equation (6.64), $\dot{z}_1$ is also bounded. Hence, by Barbalat's lemma, $z_1 \to 0$ as $t \to \infty$, achieving asymptotic regulation.

It is worth nothing that Assumption **A.2** can be relaxed using results of [64].

Possible choices for the robust function α_{21} are available in [65, 66], and are presented below

$$g \ge |\tilde{\mathbf{\Theta}}^T\Lambda - b_n'\,\tilde{\varrho}\alpha_1 + D| \tag{6.89}$$

$$\alpha_{21} = -\frac{g}{b'_{n_{min}}} tanh(\frac{0.2785\, g z_1}{\epsilon_1}) \qquad (6.90)$$

where

$$0 \leq |x| - x\, tanh(\frac{x}{\epsilon}) \leq 0.2785\, \epsilon\,,\ \epsilon > 0\,,\ x \in \mathbf{R} \qquad (6.91)$$

Alternatively, α_{12} may be chosen as

$$g \geq |\tilde{\Theta}^T \Lambda - b'_n\, \tilde{\varrho} \alpha_1 + D|^2 \qquad (6.92)$$

$$\alpha_{21} = -\frac{g\, z_1}{4\, b_{n'_{min}}\, \epsilon_1} \qquad (6.93)$$

Similarly, α_{22} can be chosen to satisfy Equations (6.75) and (6.76), using the following form

$$\alpha_{22} = -\frac{z_1}{4\, b_{n_{min}}\, \epsilon_2} \qquad (6.94)$$

6.9 Robust Adaptive Output Control Applied to AFM

The dynamic order of the adaptive controller will depend on the number of uncertain parameters and the number of states of the model. The latter governs the order of observer dynamics needed to estimate the unmeasured sates since only output measurement is utilized. Therefore, in order to minimize the dynamic order of the controller a simple low-order model is desired. The model chosen consists of the scanner bending pole-zero pair as in Equation (6.4). In addition, a first order filter is augmented with the model. To include integration action in the controller, a constant input disturbance $\bar{d}_i$ is considered. The design model is therefore given by

$$\dot{x}_1 = x_2 - (a_1 + p) x_1 + p\, b_2 u + \bar{d}_i$$

$$\dot{x}_2 = x_3 - (a_o + p\, a_1) x_1 + p\, b_1 u$$

$$\begin{aligned}
\dot{x_3} &= -p\, a_o x_1 + p\, b_o u \\
y &= x_1 + d_o \\
\dot{\mathbf{x}} &= A\mathbf{x} - \mathbf{a}'\, x_1 + \mathbf{b}'\, u + \mathbf{r} \\
\mathbf{a}' &= [a_1 + p\,, a_o + p\, a_1,\, pa_o]^T\,,\ \mathbf{b}' = p\,[b_2\,, b_1\,, b_o]^T\,,\ \mathbf{r} = [\bar{d}_i\,, 0\,, 0]^T
\end{aligned} \tag{6.95}$$

The results of section 6.8, can be applied directly to obtain the controller. The update law for $\bar{d}_i$ is $\dot{\hat{\bar{d}}}_i = \gamma_{\hat{\bar{d}}_i} z_1, \Rightarrow \hat{\bar{d}}_i = \gamma_{\hat{\bar{d}}_i} \int z_1 dt$, which provide the desired integration action of the output error as part of the control signal.

6.9.1 Selection of Controller Parameters

Estimates on bounds on the unknown parameters may be obtained as follows. The scanner is excited in bending and the PSD signal is collected. The first resonance frequency ω_{r_1} may be identified automatically by software. Alternatively, the collected data may be graphically presented to the user. The user then identifies the first resonance by clicking on the first peak in the amplitude data. The value of ω_{r_1} can be stored for future usage. This procedure could be done during calibration of the AFM and need not be repeated before each scan experiment. Therefore, $a_o = \omega_{r_1}^2$, and $a_1 = 2\zeta\omega_{r_1}$. Damping ratio ζ, of the scanner bending is expected to be low as in typical mechanical structures. However, an accurate estimate is not needed, and an overestimate of the rage of damping will not affect performance so much. Hence, ζ can be let to vary from a very small number say 0.1% up to say .2. The probe is then brought into contact with the sample and then retracted until the contact is broken. using this data an estimate of the cantilever deflection at the pull-off point can be obtained. The estimate may be reduced by a factor of safety to account for variations in the sample properties, hence different pull-off forces at different points on the sample surface. In addition, an estimate of the sensitivity of V_z to PSD signal can be obtained from probe retraction data. The sensitivity is the DC gain of the transfer function $G_p(0)$. Due to possible variations in the DC gain based on set-point and sample properties the range for the DC gain may be increased to vary for example within an order of magnitude. Therefore, $b_o = G_p(0)\, a_o$. The frequency of the modal zeros (ω_z) has been shown to vary around the resonance frequency. Hence, $b_2 = \frac{b_o}{\omega_z}$. Finally, $b_1 = 2\zeta_z\omega_z b_2$, where again ζ_z

made to vary as for ζ.

Bounds on sample topography disturbance or equivalently, d_o may be obtained by considering that while in-contact, the cantilever deflection would take the minimum value of pull-off force and would vary during the short response time of the feedback system ($\sim 4\,\omega_b$) with a maximum rate of $|\dot{d}_o| = \frac{V_x}{tan(\alpha_p)}$. Hence, bounds on $d_o \in [y_{po}, y_s + \frac{V_x}{tan(\alpha_p)} 4/\omega_b]$. Additional margins can be included to account for variations in the pull-off point. The constant input disturbance $\bar{d}_i$ was introduced to realize an integral action in the controller. For practical implementation, a mechanism for integrator anti-wind up need to be included. The mechanism could be devised by appropriately choosing the range of the unknown disturbance $\bar{d}_i$. The integral part of the control signal is $u_I = \hat{\varrho}\hat{\bar{d}}_i = \hat{\varrho}\gamma_{\bar{d}_i} \int z_1 dt$, where, $\hat{\varrho} \in [1/b_{2_{max}}, 1/b_{2_{min}}]$. Hence, $u_{min}/b_{2_{max}} \leq \hat{\bar{d}}_i \geq u_{max}/b_{2_{min}}$, where $\gamma_{\bar{d}_i}$ acts as an integral gain. Therefore, the output of the integrator is saturated at the minimum and maximum values of the control signal, u_{min} and u_{max}, respectively.

Th observer gain vector $\mathbf{k}$, is chosen to place the eigenvalues of the observer filters at the desired locations. In general the observer eigenvalues should be faster than the first bending resonance. However, excessive observer bandwidth would result in amplifying measurement noise, and may increase the effect of unmodeled dynamics on the feedback system. The first order filter cut off frequency p should also be chosen similarly. It is interesting to note that the filter p can help reduce exciting unmodeled dynamics of the AFM and reduce the effect of high-frequency measurement noise. Therefore, the filter is practically valuable, in addition it is simple and intuitive to tune. The gain k_{z_1} dictates the decay rate of transient response with a time constant of $\frac{1}{2k_{z_1}}$. So it should be chosen about the order of the first resonance response time.

The values of ϵ_1 and ϵ_2, may be chosen small to reduce the final set-point error, at least theoretically. Choosing small values would increase the feedback bandwidth, hence, may violate the validity of the assumed design model. As a result, unmodeled dynamics may cause feedback instability. Further work is needed to understand how values of ϵ_1 and ϵ_2, may be chosen in the presence of unmodeled dynamics. In the simulation study which will

be presented shortly, $\epsilon_1 = 3$ and $\epsilon_2 = k_{z_1}$, were used.

The scan speed may be used to control the frequency content of sample topography disturbance as seen by the AFM feedback system. The adaptive controller contains an inverse of the plant dynamics which is tuned in real time to compensate for parametric uncertainties. Thus, if the disturbance contains frequencies close to the plant complex zeros, the response of the control signal is expected to be oscillatory, as it strives to maintain the output error small. Consequently, in contrast to I-control, the scan speed should be selected first, and then the contact force set-point may be chosen accordingly. The minimum sample features that the probe can detect laterally depends on the probe radius of curvature. There maybe different definitions for the size of the minimum detectable feature. However, from a dynamics point of view, it is desired that the probe track the finest sample features it can detect without introducing oscillations in the control signal. Hence, as seen in Figure 6-20, the scan speed may be estimated by setting the scan speed such that the probe moves laterally a distance of $4\,R_p$ within the response time of the scanner $\frac{1}{\omega_{r_1}\,(Hz)}$, hence, the maximum $v_{scan_{max}}$ is given by

$$v_{scan_{max}} \quad = \quad 4R_p\omega_1\,(Hz) \tag{6.96}$$

As has been discussed previously, within the response time $\frac{1}{\omega_{r_1}\,(Hz)}$, an estimate of the maximum distance the cantilever can deflect from the set-point Δy_{PSD}, under the sharpest feature is given by

$$|\Delta y_{PSD}| \quad = \quad |y_s - ypo| = \frac{v_{scan}\,DCgain}{\omega_{r_1}\,tan(\alpha_p)\,k_{z_p/V_z}} \tag{6.97}$$

where DC gain is the estimate of sensitivity between V_z and y_{PSD}, and k_{z_p/V_z} is the small amplitude linear calibration factor between V_z and the scanner vertical displacement z_p. Hence, the minimum force set-point can be estimated. The actual set-point may be chosen slightly larger to allow for variations in the pull-off force over the sample surface and approximations made in the above equations.

6.9.2 Simulation Results

In order to test the performance of the RAOC controller, simulations were performed. The model used for simulations was far more realistic than the low-order design model. The model is 10th order with a relative degree of 6, in contrast to the 2nd order zero relative degree design model. The simulation model retained the first two bending modes at 380 and $3.4\,kHz$, and the associated zeros at $430\,Hz$ and $3.8\,kHz$. In addition, a single mode for the cantilever was also included. The phase lag introduced by the dynamics of the drive amplifier was accounted for using two 2nd order filters with resonance frequency of $8\,kHz$ and damping ratio of 0.707. This matches the measured frequency response of the amplifier within the frequency range of interest. Finally, a bandwidth-limited white noise source was used as a input to the cantilever. This simulates the effect of thermal and measurement noise on the cantilever output. The resulting cantilever noise oscillations were $2\AA$ peak-to-peak at a bandwidth of $10\,kHz$. These values were chosen to reflect typical specifications of commercial AFMs. The sample shape used in the simulation is that of the calibration steps. The sample contains both high-aspect ratio features in addition to fine features, which would allow testing the controller performance for different types of samples. Other parameter values used in the simulations are given in Appendix A.

The scanning simulations were performed using both the RAOC and an I-controller. The gain of the I-controller was maximized until oscillations were observed in the image, which leads to no conservatism is selecting the integral gain. This allows a fair comparison between both controllers. Figure 6-27, shows the retrace image at scan speed of $30\,\mu m/s$ for both controllers. The results show that both images portray the general shape correctly, however, some of the details are lost with the I-controller. It is seen that the sharpness of the edges is not tracked well. Hence, for quantitative measurements they may result is large errors. In Figure 6-27, the slope of the right side of the step-like sample is measured with a 10.4 % error using the I-controller. The set-point error is shown in Figure 6-28, where it is seen that a substantial reduction in output error $(4.7\,\AA)$, is achieved with the RAOC compared to I-controller $(329\,\AA)$, a reduction by a factor of 70 in the maximum dynamic error. In addition, Figure 6-29, shows the set-point error for both the trace and retrace

lines. It can be seen that in the retrace (second pass) the tracking error is substantially improved compared to the trace image as a result of adaptation; $2.3\,\AA$ versus $24\,\AA$. Hence, with the adaptive controller it is advantageous to create the image from the retrace lines.

Figure 6-30, show the simulated image at $70\,\mu m/s$. The increased scan speed causes the topography disturbance to contain higher frequency components. This is especially true around areas where a rapid change in topography occurs. Figures 6-31 and 6-32, show a zoomed view at the top left and bottom right corners of the step, respectively. It can be seen that for the RAOC, artifacts are generated due to oscillations in the control signal as the controller tries to maintain a small set-point error. Maximum amplitude of oscillations of 4 and $16\,\AA$, at the top left and bottom right corners of the step. The numbers show that the faster disturbance has caused larger oscillation amplitudes. The slope at the left is 22.7% in error for the I-controller compared to 2.6 % for the RAOC. Hence, for quantitative data the RAOC would provide a substantial improvement in data accuracy compared to I or PID control. The set-point error is shown in Figure 6-33. The maximum error of $11.7\,\AA$ for the RAOC in contrast to $574.7\,\AA$ for the I-controller. Hence, substantial reduction in maximum contact force, as a result, a smaller contact force set-point may be selected compared to I or PID control for the same scan speed. Figure 6-34, shows the so-called convolution errors that result in the image due to the finite size of the probe. There are several procedures for deconvolving the image in order to recover an estimate of the true sample shape. Convolution is especially important for sample features with characteristic dimension similar to that of the probe or having a high-aspect ratio. The quantitative errors produced above by the I-controller would translate to more error and uncertainties in the deconvolved sample shape estimate. The above results also demonstrate that the noise level in the image is low. This is a result of choosing of a reasonable bandwidth of $1\,kHz$ for the observer and the first order filter dynamics.

It is worth noting that the effect of creep compensation filter on stability and performance of RAOC is expected to be minor. The error in approximating creep by a low-order zero relative degree transfer function can be viewed as an input disturbance d_i. This dis-

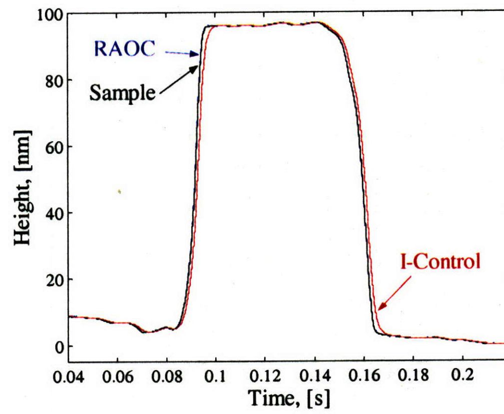

Figure 6-27: Imgae of a step scanned at $30\,\mu m/s$.

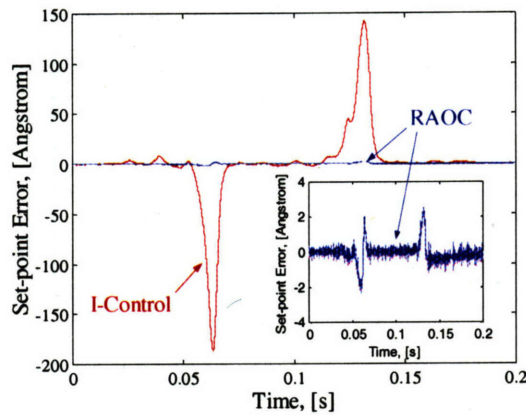

Figure 6-28: Set-point Error in $\mathring{A}$ for image of a step scanned at $30\,\mu m/s$.

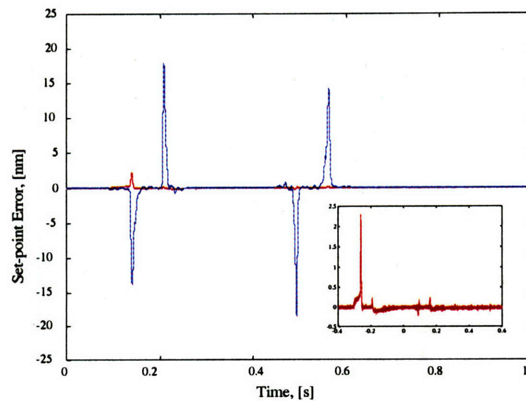

Figure 6-29: Set-point Error in $\mathring{A}$ for image of a step scanned at $30\,\mu m/s$.

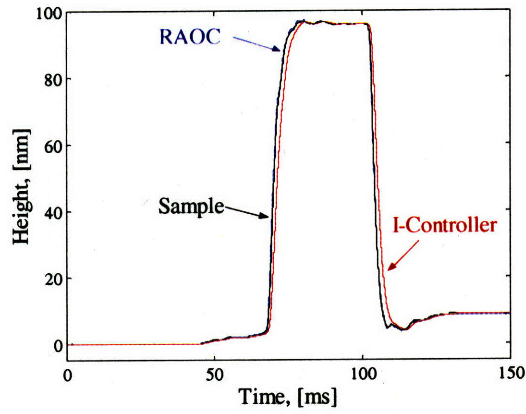

Figure 6-30: Image of a step scanned at 70 $\mu m/s$.

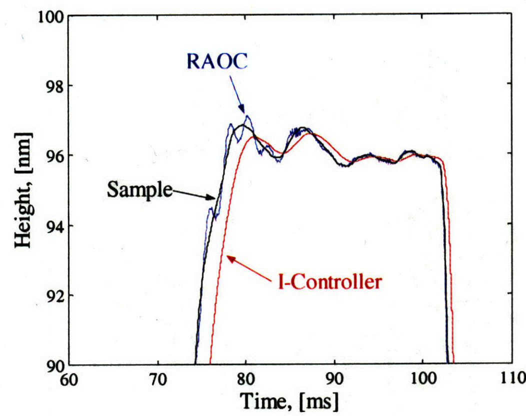

Figure 6-31: Zoom on top left of step image scanned at 70 $\mu m/s$.

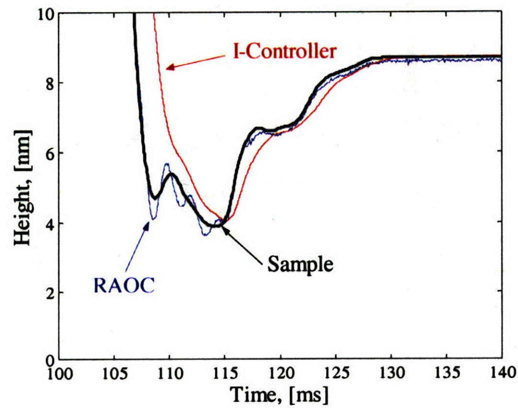

Figure 6-32: Zoom on bottom right of step image scanned at 70 $\mu m/s$.

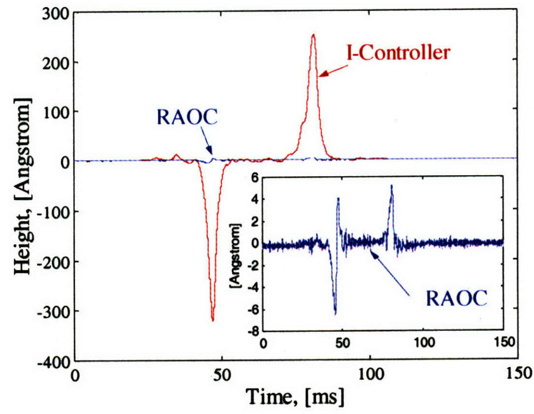

Figure 6-33: Set-point Error in $\AA$ for step image scanned at $70\,\mu m/s$.

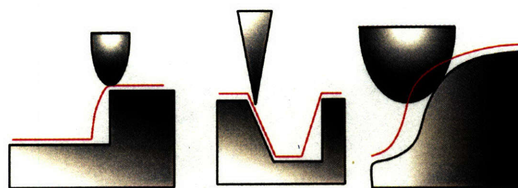

Figure 6-34: AFM image convolution due to finite size of the probe.

turbance will be within the feedback bandwidth. Hence, the RAOC can easily compensate for this modeling error.

6.10 Summary

In this chapter, procedures for selecting scan and controller parameters were presented. First, factors affecting scan parameter selection were discussed. Then, performance trade-offs and limitations of the AFM feedback system were identified and analyzed. These limitations resulted in a severe bound on the maximum achievable feedback bandwidth, as well as a fundamental trade-off between step response overshoot and response time. A careful analysis has revealed that a PID controller has no real advantage over an integral controller. Therefore, a procedure for automatically selecting key scan parameters and controller gain was developed and experimentally tested for I-control. This approach, in contrast to the commonly used trial and error method, can substantially improve image quality and fidelity. Furthermore, procedures for variable scan speed and feedforward compensation were presented. In addition, a robust adaptive output controller (RAOC), was designed to guarantee global boundedness and asymptotic regulation in the presence and absence of disturbances, respectively. Simulations have shown that a substantial reduction in contact force can be achieved with the RAOC, in comparison with a well-tuned I-controller, yet with no increase in the maximum scan speed.

Chapter 7

Conclusions and Recommendations

The phenomenal resolution and versatility of the atomic force microscope (AFM), has made it a widely-used instrument in nanotechnology. The fidelity of AFM data relies, among other factors, on the AFM's dynamic response and the performance of its feedback system. As a result, data artifacts may result from poor AFM dynamics. The work in this thesis has focused on achieving consistent and improved dynamic response of the AFM, through identifying, analyzing, and controlling sources that may contribute to an undesirable poor performance. Consequently, substantially improving data accuracy, and consistency in addition to expanding the range of applications of the AFM.

As a first step, a detailed model of the AFM dynamics has been developed. It includes a new model for the piezoelectric scanner coupled longitudinal and lateral dynamics, creep, and hysteresis. Models for probe-sample interactions and cantilever dynamics were also included. The wide use of the tube scanner in many applications including other scanning probe microscopes (SPM), makes the developed scanner model remarkably valuable for the design and performance analysis of such applications.

An extensive parametric study has been performed to experimentally analyze in-contact dynamics. The experiments were performed for different samples, cantilevers, contact force set-points, and disturbance amplitudes. Nonlinear variations in the frequency response were observed, in addition to changes in the pole-zero structure. The choice of scan parameters

was found to have a major impact on image quality and feedback performance. Moreover, the developed model was used to analyze the AFM dynamics, and was found competent in reproducing experimental observations both for in-contact frequency response and scanning simulations. In addition, the analysis has shown that the coupled scanner response have a substantial impact on AFM performance in several ways. It was found that the scanner bending mode is observable form the output signal. Consequently, the feedback bandwidth is limited by the bending rather than the longitudinal mode as commonly stated in the literature. A substantial reduction in the potentially achievable feedback bandwidth occurs; a reduction from $4.6\,kHz$ to $380\,Hz$ in the AFM used in this work. Furthermore, it was found that the frequency of the first system resonance (bending mode), is not affected by probe-sample interactions. This is a result of the large force capacity of the actuator $\sim 1\,N$, in comparison to the minute probe-sample interaction forces $\sim$ 10s nN. This important finding was used in the procedures developed for improving the AFM performance. Furthermore, the coupling as observed from the output signal, is expected to affect the scanner vertical calibration by $< 1\%$ at full range, typically. Further analysis has revealed that the ratio of the effective contact to cantilever stiffnesses governs the pole-zero structure of the system. For large ratios, a pole-then-zero structure appears. On the other hand, ratios close to 1 may result in pole-zero flipping causing a zero-then-pole structure. The impact of this uncertainty on feedback stability and robustness is dramatic.

Hysteresis was addressed by first discussing mechanisms contributing to its presence in piezoelectric materials. A brief discussion on models available in the literature was then presented. Based on physical reasonings the scanner model was modified to allow including a hysteresis model in a physically-consistent manner. The two hysteresis variables in the model are the electric displacement and an equivalent hysteresis voltage. As a result, implementation difficulties arise since measuring the charge or current have several practical drawbacks. Experimental hysteresis data was used to demonstrate some of the hysteresis models. A suggestions in the literature to use the derivative of the input in a hysteresis model was shown to be not only physically-unmotivated but in addition does not capture the nonlinear variation in the hysteresis loop average slope and loop width. This issue re-

mains unresolved to be addressed in future work.

Experimental tests were performed to validate the creep model and study creep behavior of common AFM scanners. It was found that creep did not depend on input rate and assumption on linearity of the amount of creep is reasonable. A procedure for identifying creep response for vertical and lateral directions was presented, and an interactive routine was proposed for fitting the data to the creep model. Model-based creep compensation was proposed to reduce creep effects on AFM data and on scanner vertical and lateral calibration , hence achieving more consistent results for different scan speeds. Moreover, compensation for scanner creep in the vertical direction was experimentally tested and it was found that creep was reduced by a factor of 3 to 4 from the uncompensated system.

Moreover, the model was used to identify fundamental performance limitations in the AFM feedback system. The main limitations were found to be due to the high-level of uncertainty including pole-zero flipping, in addition to the pole-zero structure of the system. These limitations resulted in a severe bound on the maximum achievable feedback bandwidth, as well as a fundamental trade-off between step response overshoot and response time. Careful analysis on the requirement for robustness to high-frequency unmodeled dynamics in addition to the fundamental time response trade-off, has revealed that a PID controller has no real advantage over an integral controller. Therefore, a procedure for automatically selecting key scan parameters and controller gain was developed and experimentally tested for I-control. This approach, in contrast to the commonly used trial and error method, can substantially improve image quality and fidelity.

Additionally, further improvement on performance was suggested by utilizing a feedforward term based on trace-line data to be used with retrace line. The method would work best for high-resolution images. In addition, a variable scan speed algorithm was proposed. The use of the algorithm is not limited to I-control. The scan speed of the retrace line was varied based on the maximum output error of the trace line. The procedure is simple and would improve consistency and accuracy of data to a user prescribed tolerance on output

error. However, the algorithm would work best if either creep compensation or closed loop are employed for scanner lateral direction.

In addition, a robust adaptive output controller (RAOC), was designed to guarantee global boundedness and asymptotic regulation in the presence and absence of disturbances, respectively. Simulations have shown that a substantial reduction in contact force can be achieved with the RAOC, in comparison with a well-tuned I-controller. This would translate to reduced probe-sample friction in addition to improved data accuracy. This would be a substantial gain for imaging soft fragile samples and samples that suffer for convolution errors. However, using the RAOC no increase in the maximum scan speed was achieved. This is a result of the controller inversion of plant complex zeros. Furthermore, a new method was developed to allow calibrating the scanner's vertical displacement from few nanometers up to its full range, in addition to characterizing scanner hysteresis.

This work has identified and addressed crucial problems and proposed practical solutions to factors limiting the dynamic performance of the AFM. The developed comprehensive and realistic AFM model, in addition to the analysis and compensation methods presented, represent new contributions complementing the existing literature. In addition, the work has opened new directions for possible future work.

Suggestions for future work include experimental verification of the performance of the adaptive controller. Additionally, issues of parameter selection in the presence of unmodeled dynamics should be addressed. Moreover, additional testing of all proposed algorithms under different operating conditions, with different samples and cantilevers should be beneficial for further developments and improvements to the algorithms. Furthermore, the proposed calibration method for the scanner's vertical displacement should be experimentally tested and compared to the conventional calibration method for small scanner displacements. Moreover, the aforementioned problem of hysteresis control could be addressed. Finally, innovative redesigns of the AFM may provide solutions to increasing the AFM bandwidth.

Bibliography

[1] B. Bhushan, *Nanotribology and Nanomechanics of MEMS Devices*, Proceedings of the Ninth Annual International Workshop on Micro Electro Mechanical Systems, pp. 91-98, 1996.

[2] T.E. Fisher, P.E. Marszalek, A.F. Oberhauser, M. Carrion-Vazquez, and J.M. Fernandez, *The Micro-mechanics of Single Molecules Studied with Atomic Force Microscopy*, Journal of Physiology, Vol. 520 (1), pp. 5-14, 1999.

[3] O.M. El Rifai, and K. Youcef-Toumi, *On Factors Affecting The Performance of Atomic Force Microscopes in Contact-mode*, 1999 IEEE/ASME International Conference on Advanced Intelligent Mechatronics, Atlanta, GA, USA, 19-23 September, pp. 21-26, 1999.

[4] Taylor M. E., *Dynamics of Piezoelectric Tube Scanners for Scanning Probe Microscopy*, Review of Scientific Instruments Vol. 64 (1), pp. 154-158, January 1993.

[5] Tetsuo Ohara, and K. Youcef-Toumi, *Dynamics and Control of Piezotube Actuators for Subnanometer Precision Applications*, Proceedings of the American Control Conference, Seattle, Washington, pp. 3808-3812, June 1995.

[6] S. Yang, and W. Huang, *Transient Responses of a Piezoelectric Tube Scanner*, Review of Scientific Instruments, Vol. 68, 1997, pp. 4483-4487.

[7] H.-J. Butt, P. Siedle, K. Seifert, K. Fendler, T. Seeger, E. Bamberg, A. L. Weisenhorn, K. Goldie, and A. Engel, *Scan Speed Limit in Atomic Force Microscopy*, Journal of Microscopy, Vol. 169, Pt. 1, pp. 75-84, January 1993.

[8] N. Tamer, and M. Dahleh, *Feedback Control of Piezoelectric Tube Scanner*, Proceeding of the 33rd IEEE Conferece on Decision and Control, pp. 1826-1831, 1994.

[9] A. Daniele, T. Nakata, L. Giarre, M.V. Salapaka, and M. Dahleh, *Robust Identification and Control of Scanning Probe Microscope Scanner*, Proceeding of the IFAC Symposium on Robust Control Design, Budapest, Hungary, pp. 33-38, June 25-27, 1997.

[10] H.J. Adriaens, W.L. de Koning, and R. Banning, *Modeling Piezoelectric Actuators*, IEEE/ASME Transaction on Mechatronics, Vol. 5 (4), pp. 331-341, December 2000.

[11] R.D. Mindlin, and L.E Goodman, *Beam Vibrations with Time-dependant Boundary Conditions*, Journal of Applied Mechanics, Vol. 17, pp. 377-380, 1950.

[12] G. Binning, C. F. Quate, and C. Gerber, *Atomic Force Microscope*, Physical Review Letters, Vol. 56 (9), pp. 930-933, 1986.

[13] Y. Martin, C. C. Williams, and H. K. Wickramasinghe, *Atomic Force Microscope-Force Mapping and Profiling on a Sub 100-Angstrom*, Journal of Applied Physics, Vol. 61 (10), pp. 4723-4729, 1987.

[14] Q. Zhong, D. Inniss, K. Kjoller, and V. B. Elings, *Fractured Polymer/Silica Fiber Surface Studied by Tapping Mode Atomic Force Microscopy*, Surface Science Letters, Vol. 290, pp. L688-692, 1993.

[15] D. Maugis, *Adhesion of Spheres: The JKR-DMT Transition Using a Dugdale Model*, Journal of Colloid and Interface Science, Vol. 150 (1), pp. 243-269, 1992.

[16] M. Goken, and H. Vehoff, *Quantitative Metallography of Structural Materials with the Atomic Force Microscope*, Scripta Materialia, Vol. 35, pp. 983-989, 1996.

[17] J. Tamayo, and R. García, *Deformation, Contact Time, and Phase Contrast in Tapping Mode Scanning Force Microscopy*, Langmuir Vol. 12, pp.4430-4435, 1996.

[18] Stavely Sensors Inc., *EBL Product Line Catalog*, 91 Prestige Park Circle, East Hartford, CT 06108-1918.

[19] Preisach F., *Uber die Magnetische Nachwirkung*, Zeitschrift fur Physik Vol. 94, pp. 277-302, 1935.

[20] Mayergoyz I. D., *Mathematical Models of Hysteresis*, Springer-Verlag, New York, 1991.

[21] M.A. Krasnosel'skii, and A.V. Pokrovskii, *Systems with Hysteresis*, Springer-Verlag, Berlin, 1989.

[22] B.J. Lazan, *Damping of Materials and Members in Structural Mechanics*, Pergamon Press, London, 1968.

[23] R. Bouc, *Forced Vibration of Mechanical System with Hysteresis*, Proceedings of 4th Conference on Nonlinear Oscillations, Parague, Czechoslovakia, pp. 315, 1967.

[24] Y-K Wen, *Methods for Random Vibration of Hysteretic Systems*, Journal of the Engineering Mechanics Division EM2, pp. 249-263, April 1976.

[25] P.R. Dahl, *Solid Friction Damping of Mechanical Vibrations*, American Institute of Aeronautics and Astronautics Journal Vol. 14 (12), pp. 1675-1682, December 1976.

[26] L.O. Chua, and K.A. Stromsmoe, *Mathematical Model for Dynamic Hysteresis Loops*, International Journal of Engineering Science Vol. 9, pp. 435-450, 1971.

[27] L.O. Chua, and S.C. Bass, *A Generalized Hysteresis Model*, IEEE Transactions on Circuit Theory, Vol. CT-19 (1), pp. 36-48, January 1972.

[28] B.D. Coleman, and M.L. Hodgdon, *A Constitutive Relation for Rate-independent Hysteresis in Ferromagnetically Soft Materials*, International Journal of Engineering Science Vol. 24 (6), pp. 897-919, 1986.

[29] D. Hughes, and J.T. Wen, *Preisach Modeling of Piezoceramic and Shape Memory Alloy Hysteresis*, Smart Materials and Structures Vol. 6, pp. 287-300, 1997.

[30] M. Goldfarb, and N. Celanovic, *Modeling Piezoelectric Stack Actuators for Control of Micromanipulation*, IEEE Control Systems Magazine Vol. 17 (3), pp. 69-79, June 1997.

[31] R. Smith, and Z. Ounaies, *A Domain Wall Model for Hysteresis in Piezoelectric Materials*, Institute for Computer Applications in Science and Engineering, NASA Langley Research Center, NASA/CR-1999-209832 and ICASE Report No. 99-52, 1999.

[32] I-W. Chen, and Y. Wang, *A Domain Wall Model for Relaxor Ferroelectrics*, Ferroelectrics, Vol. 206, pp. 245-263, 1998.

[33] V.N. Fedosov, and A.S. Sidorkin, *Quasielastic Displacements of Domain Boundaries in Ferroelectrics*, Soviet Physics Solid State Vol. 18 (6), pp. 964-968, 1976.

[34] *IEEE Standard on Piezoelectricity*, ANSI/IEEE Std 176-1987, 1987.

[35] M. Jaschke, and H-J. Butt, *Height Calibration of Optical Lever Atomic Force Microscopes by Simple Laser Interferometry*, Review of Scientific Instruments Vol. 66 (2), pp. 1258-1259, February 1995.

[36] M. Tortonese, H. Yamada, R.C. Barrett, and C.F.Quate*Atomic Force Microscopy using a Piezoresistive Cantilever*, Trabsducers 91, International Conference on Solid-State Sensors and Actuators, pp. 448-451, 1991.

[37] J.A. Harley, *Advances in Piezoresistive Probes for Atomic Force Microscopy*, Ph.D. Thesis, Stanford University, 2000.

[38] M. Tortonese, *Force Sensors for Scanning Probe Microscopy*, Ph.D. Thesis, Stanford University, 1993.

[39] *Q-Scope 250*, Quesant Instrument Corporation, 29397 Agoura Road - Suite 104 Agoura Hills, CA 91301, USA, www.quesant.com

[40] *BenchMate* 2212 , Kinetics Systems Incorporated, 20 Arboretum Road, P.O. Box 414, Rosilindale, MA 02131, USA, www.kineticsystems.com

[41] *ISOCHAMBER* , Burleigh Instruments, www.burleigh.com

[42] *DS1103 PPC Controller Board* , dSPACE Inc., 28700 Cabot Drive - Suite 1100, Novi, MI 48377, USA, www.dspaceinc.com

[43] S. Mittal, and C-H. Menq, *Hysteresis Compensation in Electromagnetic Actuators Through Preisach Model Inversion*, IEEE/ASME Transaction on Mechatronics Vol. 5 (4), pp. 394-409, December 2000.

[44] *Cantilever Model: ULTRASHARP CSC17-E*, http://siliconmdt.com, 2001.

[45] *Cantilever Model: Pointprobe, Type: CONT*, http://www.nanosensors.com/, 2001.

[46] Anders Kühle, Alexis H. Sørensen, and Jakob Bohr, *Role of Attractive Forces in Tapping Tip Force Microscopy*, J. Appl. Phys., Vol. 81 (10), pp.6562-6569, 1997.

[47] Jian Chen, Richard Workman, Dror Sarid, and Ralf Höper, *Numerical Simulations of Scanning Force Microscope with a Large-Amplitude Vibrating Cantilever*, Nanotech. Vol. 5, pp. 199-204, 1994.

[48] S. Hirsekorn, U Rabe, and W. Arnold, *Theoretical Description of the Transfer of Vibrations from a Sample to the Cantilever of an Atomic Force Microscope*, Nanotech., Vol. 8, pp. 57-66, 1997.

[49] N. A. Burnham, O. P. Behrend, F. Oulevey, G. Gremaud, P-J Gallo, D. Gourdon, E. Dupas, A. J. Kulik, H. M. Pollock, and G. A. Briggs, *How Does a Tip Tap*, Nanotechnology, Vol. 8, pp. 67-75, 1997.

[50] N. A. Burnham, R.J. Colton, and H.M. Pollock *Interpretation of Force Curves in Force Microscopy*, Nanotechnology, Vol. 4, pp. 64-80, 1993.

[51] B. D. Aumond, *High Precision Profilometry*, Mechanical Engineering M.S. Thesis, Massachusetts Institute of Technology, 1997.

[52] J. Kerssemakers, and J. Th. M. De Hosson, *A Quantitative Analysis of Surface Deformation by Stick/Slip Atomic Force Microscopy*, J. Appl. Phys., Vol. 82, pp. 3763-3770, 1997.

[53] S. Fujisawa, Y. Sugawara, S. Ito, S. Mishima, T. Okada, and S. Morita, *The Two-Dimensional Stick-Slip Phenomenon with Atomic Resolution*, Nanotech., Vol. 4, pp. 138-142, 1993.

[54] E. Meyer, R. Luthi, L. Howald, M. Bammerlin, M. Guggisberg, and H.-J. Guntherodt, *Site-Specific Friction Force Spectroscopy*, J. Vac. Sci. Tech. B, Vol. 14, pp. 1285-1288, 1996.

[55] R. W. Carpick, N. Agrait, D. F. Ogletree, and M. Salmeron, *Measurement of Interfacial Shear (Friction) with an Ultra-High Vacuum Atomic Force Microscope*, J. Vac. Sci. Tech. B, Vol. 14, pp. 1289-1295, 1996.

[56] A. M. Homola, J. N. Israelachvili, M. L. Gee, and P. M. McGuiggan, *Measurements of and Relation Between the Adhesion and Friction of 2 Surfaces Separated by Molecularly Thin Liquid-Films,* Journal of Tribology, Vol. 111 (4), pp. 675-682, 1989.

[57] F. P. Bowden, and D. Tabor, *The Friction and Lubrication of Solids*, Clrendon, Oxford, 1950.

[58] N. Agrait, G. Rubio, and S. Vieira, *Plastic Deformation in Nanometer Scale Contacts*, Langmuir 12, pp. 4505-4509, 1996.

[59] M. Goken, H. Vehoff, and P. Neumann, *Atomic Force Microscopy Investigation of Loaded Crack Tips in NiAl*, J. Vac. Sci. Techn. B, Vol. 14, pp. 1157-1161, 1996.

[60] H. Vehoff, P. Ochmann, M. Goken, and M. Gehling, *Deformation Processes at Crack Tips in NiAl Single- and Bi-Crystals*, Mat. Sci. Eng. A, Vol. 239-240, pp. 378-385, 1997.

[61] A. C. Ugural, *Advanced Strength and Applied Elasticity*, 3rd Ed., Englewood Cliffs, N.J., Prentice Hall, 1995.

[62] K. L. Johnson, *Continuum Mechanics Modeling of Adhesion and Friction*, Langmuir, Vol. 12, pp. 4510-4513, 1996.

[63] M. Krstic, I. Kanellakopoulos, and P. V. Kokotovic, *Nonlinear and Adaptive Control Design*, John Wiley and Sons, New York, 1995.

[64] R. D. Nussbaum, *Some Remarks on a Conjecture in Parameter Adaptive Control*, System Control Letter, Vol. 3, pp. 243-246, 1983.

[65] M. M. Polycarpou, and P. A. Ioannou *A Robust Adaptive Nonlinear Control Design*, Proceedings of the American Control Conference, San Francisco, CA, pp. 1365-1369, June 1993.

[66] B. Yao, and M. Tomizuka, *Adaptive Robsut Control of Nonlinear Systems: Effective Use of Information*, Proceedings of the 11th IFAC Symposium on System Identification, pp. 913-918, 1997.

[67] O. M. El Rifai, and K. Youcef-Toumi, *Dynamics of Contact-mode Atomic Force Microscopes*, American Control Conference, Chicago, Illinois, USA, June 28-30, pp. 2118 -2122, 2000.

[68] O. M. El Rifai, and K. Youcef-Toumi, *Coupling in Piezoelectric Tube Scanners Used in Scanning Probe Microscopes*, American Control Conference, Arlington, Virginia, USA, June 25-27, pp. 3251-3255, 2001.

[69] O. M. El Rifai, and K. Youcef-Toumi, *Creep in Piezoelectric Scanners of Atomic Force Microscopes*, American Control Conference, Anchorage, Alaska, USA, May 8-10, 2002.

[70] T. Bouhacina, D. Michel, J. P. Aime, and S. Gauthier, *Oscillation of the Cantilever in Atomic Force Microscopy: Probing the Sample Response at the Microsecond Scale*, Journal of Applied Physics, Vol. 82, 1997, pp. 3652-3660.

[71] G. Y. Chen, R. J. Warmack, A. Huang, and T. Thundat, *Harmonic Response of Near-Contact Scanning Force Microscopy*, Journal of Applied Physics, Vol. 78, 1995, pp. 1465-1469.

[72] B. D. Aumond, *High Precision Profilometry*, Mechanical Engineering M.S. Thesis, Massachusetts Institute of Technology, 1997.

[73] J. Kerssemakers, and J. Th. M. De Hosson, *A Quantitative Analysis of Surface Deformation by Stick/Slip Atomic Force Microscopy*, Journal of Applied Physics, Vol. 82, pp. 3763-3770, 1997.

[74] A. M. Homola, J. N. Israelachvili, M. L. Gee, and P. M. McGuiggan, *Measurements of and Relation Between the Adhesion and Friction of 2 Surfaces Separated by Molecularly Thin Liquid-Films,* Journal of Tribology, Vol. 111 (4), pp.675-682, 1989.

[75] M. Goken, H. Vehoff, and P. Neumann, *Atomic Force Microscopy Investigation of Loaded Crack Tips in NiAl*, Journal of Vacuum Science and Technology B, Vol. 14, pp. 1157-1161, 1996.

[76] K. L. Johnson, *Continuum Mechanics Modeling of Adhesion and Friction*, Langmuir, Vol. 12, pp. 4510-4513, 1996.

[77] R. C. Barrett, *Development and Applications of Atomic Force Microscopy*, Edward L. Ginzton Lab. Stanford Univ., G. L. No. 4847, Jul. 1991.

[78] F. M. Battiston, M. Bammerlin, C. Loppacher, R. Luthi, E. Meyer, and H.-J. Guntherodt, and F. Eggimann, *Fuzzy Controlled Feedback Applied to a Combined Scanning Tunneling and Force Microscope*, Applied Physics Letter, Vol. 72, pp. 25-27, 1998.

[79] T. M. H. Wong, and M. E. Welland, *A Digital Control System For Scanning Tunneling Microscopy and Atomic Force Microscopy*, Measurement Science and Technology, Vol. 4, pp. 270-280, 1993.

[80] S. Yang, and W. Huang, *Transient Responses of a Piezoelectric Tube Scanner*, Review of Scientific Instruments, Vol. 68, 1997, pp. 4483-4487.

[81] Patrick M. Sain, Michael K. Sain, and B. F. Spencer, *Models for Hysteresis and Applications to Structural Control*, Proceedings of the American Control Conference, Albuquerque, New Mexico, June 1997, pp. 16-20.

[82] Tadahiro Hasegawa, Sumiko Majima, *A Control System to Compensate the Hysteresis by Priesach Model on SMA Actuator*, 1998 International Symposium on Micromechatronics and Human Science, ?? , pp. 171-176.

[83] Katsushi Furutani, Mitsunori Urushibata, and Naotake Mohri, *Improvement of Control Method for Piezoelectric Actuator by combining Induced Charge Feedback with Inverse*

Transfer Function Compensation ,Proceedings of the 1998 IEEE International Conference on Robotics and Automation, Leuven, Belgium, May 1998, pp. 1504-1509.

[84] K. Kuhnen, and H. Janocha, *Adaptive Inverse Control of Piezoelectric Actuators with Hysteresis Operators*, European Control Conference, Germany, 1999. pp. ??

[85] B. M. Chen, T. H. Lee, C. C. Hang, Y. Guo, *An* H_∞ *Almost Disturbance Decoupling Robust Controller Design for a Piezoelectric Bimorph Actuator with Hysteresis*, amc96?

[86] Gang Tao, and Peter Kokotovic, *Adaptive Control of Plants with Unknown Hysteresis*, IEEE Transaction on Automatic Control, Vol. 40, no. 2, February 1995, pp. 200-212.

[87] M. F. Arnsdorf, and S. H. Xu, *Atomic(Scanning) Force Microscopy in Cardiovascular Research*, Journal of Cardiovascular Electrophysiology, Vol. 7, no. 7, July 1996, pp. 639-652.

[88] Kathryn Wilder, Hyongsok T. Soh, Abdullah Atalar, and Calvin F. Quate, *Nanometer-scale Patterning and Individual Current-controlled Lithography Using Multiple Scanning Probes*, Review of Scientific Instruments, Vol. 70, no. 6, June 1999, pp. 2822-2827.

[89] R. W. Carpick, N. Agrait, D. F. Ogletree, and M. Salmeron, *Variation of the Interfacial Shear Strength and Adhesion of a Nanometer-Sized Contact*, Langmuir, Vol. 12, 1996, pp. 3334-3340.

[90] H. Jung, and D-G. Gweon, *Creep Characteristics of Piezoelectric Actuators*, Review of Scientific Instruments, Vol. 71, No. 4, pp. 1896-1900, April 2000.

[91] H. Jung, and D-G. Gweon, *New Open-loop Actuation Method of Piezoelectric Actuators for Removing Hysteresis and Creep*, Review of Scientific Instruments, Vol. 71, No. 9, pp. 3436-3440, Septemebr 2000.

[92] K.R. Koops, P.M.L.O. Scholte, and W.L. de Koning, *Observation of Zero Creep in Piezoelectric Actauators*, Applied Physics A, Vol. 68, pp. 691-697, 1999.

[93] Hartmut Janocha, and Klaus Kuhnen, *Real-time Compensation of Hysteresis and Creep in Piezoelectric Actuators*, Sensors and Actuators A, Vol. 79, 2000, pp. 83-89.

[94] Cao Wei, Honghai Zhang, Lu Tao, Wenju Li, and Hanmin Shi, *Compensation Method Based on Formularizing Hysteresis of Piezoelectric Tube Scanner*, Review of Scientific Instruments, Vol. 67, No. 10, 1996, pp. 3594-3598.

[95] M. Jouaneh, and H. Tian, *Accuracy Enhancement of a Piezoelectric Actuator with Hysteresis*, Japan/USA Symposium on Flexible Automation, Vol. 1, pp. 631-637, 1992.

[96] L. Ljung, *System Identification: Theory for the User*, 2nd Ed., Prentice Hall PTR, NJ, USA, 1999.

[97] M. Seron, J. Braslavsky, and G. Goodwin *Fundamental Limitations in Filtering and Control*, Springer, 1997.

[98] H. Bode, *Network Analysis and Feedback Amplifier Design*, D. van Nostrand, 1945.

[99] I. Horowitz *Synthesis of Feedback Systems*, Academic Press, New York, 1963.

[100] H. Khalil, *Adaptive Output Feedback Control of Nonlinear Systems Represented by Input-Output Models*, IEEE Transactions on Automatic Control, Vol. 41 (2), pp.177-188, February 1996.

[101] G.C. Goodwin, A.R. Woodyatt, R.H. Middleton, and J. Shim, *Fundamental Limitations due to $j\omega$-axis Zeros in SISO Systems*, Automatica, Vol. 35, pp.857-8633, 1999.

Appendix A

Parameter Values Used in Simulations

Extension Tube Parameter Values

$$L_m = 44.45\,mm \qquad R_{om} = 7.435\,mm$$

$$R_{im} =_6 .285\,mm \qquad \rho_m = 2520\,kg/m^3$$

$$E_m = 66.9\,GPa \qquad M_{sh} = 120\,g$$

$$b_{m1} = 3 \times 10^4\,kg/m\,s \qquad b_{m2} = 3 \times 10^4\,kg/m\,s$$

$$b_{m3} = 1 \times 10^4\,kg/m\,s$$

Piezoelectric Tube Parameter Values

$$\epsilon_x = 49.5\,\mu m \qquad \epsilon_y = -5.1\,\mu m$$

$$R_o = 6.35\,mm \qquad R_i = 5.84\,mm$$

$$L_p = 44.45\,mm \qquad M_o = 140\,g$$

$$s_{11} = 1.5873 \times 10^{-11}\,m^2/N \qquad d_{31} = -1.73 \times 10^{-10}\,m/V$$

$$\rho_p = 7500\,kg/m \qquad b_{p1} = 5 \times 10^3\,kg/m\,s$$

$$b_{p2} = 5 \times 10^3\,kg/m\,s \qquad b_{p3} = 5 \times 10^3\,kg/m\,s$$

Cantilever beam Parameter Values

$$L_c = 350\,\mu m \qquad \rho_c = 2430\,kg/m^3$$
$$w_c = 35\,\mu m \qquad t_c = 1\,\mu m$$
$$E_c = 169\,GPa \qquad \nu_c = 0.3$$
$$l_t = 3\,\mu m$$

Adaptive Controller Parameter Values

$$sign(b_2) = 1 \qquad p = 2\pi \times 10^3$$
$$k_1 = 6\pi \times 10^3 \qquad k_2 = 12(\pi \times 10^3)^2$$
$$k_3 = (2\pi \times 10^3)^3 \qquad k_{z1} = \pi \times 10^3$$
$$\gamma_{11} = 5 \times 10^{18} \qquad \gamma_{22} = 5 \times 10^{18}$$
$$\gamma_{33} = 5 \times 10^{18} \qquad \gamma_{44} = 5 \times 10^{18}$$
$$\gamma_{55} = 5 \times 10^{18} \qquad \gamma_{66} = 5 \times 10^{18}$$
$$\gamma_{77} = 5 \times 10^5 \qquad \gamma_{88} = 5 \times 10^2$$
$$a_{1min} = 6.287 \times 10^3 \qquad a_{1max} = 1.131 \times 10^4$$
$$a_{omin} = 3.5767 \times 10^6 \qquad a_{omax} = 3.7899 \times 10^7$$
$$b_{omin} = 1.1162 \times 10^{10} \qquad b_{omax} = 5.9532 \times 10^{10}$$
$$b_{2min} = 7.8540 \times 10^2 \qquad b_{2max} = 3.7699 \times 10^4$$
$$b_{1min} = 1.9739 \times 10^4 \qquad b_{1max} = 2.8424 \times 10^8$$
$$g_{min} = -10^3 \qquad g_{max} = 10^3$$
$$\varrho_{min} = 1/b_{2max} \qquad \varrho_{max} = 1/b_{2min}$$